University of Stavanger

Faculty of Science and Technology

MASTER'S THESIS

Study program/Specialization: Marine and Offshore Technology	Spring semester, 2021 Open / ~~Restricted access~~
Writer: Nils Olav Hauge	*Nils Olav Hauge* .... (Writer's signature)

Faculty supervisor:
Associate Prof. Lin Li

Thesis title:
Numerical study on splash zone crossing with subsea template and ROV

Credits (ECTS):
30 ECTS

| Key words:

Offshore lifting operation
Subsea template
ROV
Time domain simulation
Diffraction analysis
Allowable sea state assessment | Pages: 125

+ enclosure: 28

Stavanger, 14.06/21
Date/year |

NUMERICAL STUDY ON SPLASH ZONE CROSSING WITH SUBSEA TEMPLATE AND ROV

Author   : Nils Olav Hauge

Supervisor   : Associate Prof. Lin Li

Abstract

External loads on a free-floating vessel affect the vessel responses in waves. DNV's recommended practice for modeling and analysis of marine operations [1] categorizes lifting of an object above 1-2% of the vessel displacement as a heavy lift operation. Such operations have a non-negligible impact on the vessel responses. This type of operation is primarily lifting using the vessel crane. This study focuses on two different cases of lifting operations. The first case is a purpose-made vessel for transportation and deployment/recovery of a Remotely Operated Vehicle (ROV) at the stern of the vessel. The second case is installation of a subsea template (ITS) with an offshore construction vessel. Such operations are often done at a certain heeling or trimming angle induced by the weight of the lifted object. Realistic operational weather limitations for these types of operation are important both for safety reasons and economic reasons. It is therefore interesting to investigate the consequence of changing the vessels heeling and trimming angle when performing the lifting operations.

Installation of a subsea template typically involves overboarding, lowering through the splash zone, lowering down to seabed, and landing on the seabed. Deployment of an ROV is similar, but the overboarding phase is slightly different. The ROV will be brought overboard by the launch and recovery system, lowered through the splash zone and lowered further down to working depth. The common phase for these cases is lowering through the splash zone. This study focuses on crossing of the splash zone, which is considered one of the critical phases of a deployment operation due to the potentially large hydrodynamic forces.

Comparative response analyses of the vessels with and without an initial trimming or heeling angle are conducted. The hydrodynamic properties for both vessels have been acquired through frequency domain analysis in upright/even keel condition and with a certain angle of trimming or heeling. Time domain simulations of the cases, with the acquired hydrodynamic properties, are used to study the dynamic responses of the system.

In addition to addressing the differences between simulating the deployment operations with response amplitude operators for upright/even keel position and a certain angle of trimming or heeling, the thesis discusses the differences between running the template deployment simulations as a coupled and uncoupled model.

The results indicate that waves arriving parallel to the axis that the vessel is rotated around generates larger responses for both vessels after being trimmed/heeled. Since the ROV deployment case has a criterion related to horizontal motion the larger responses cause lower allowable sea states for the trimmed case. The allowable sea states for the ITS deployment increases for the case with an initial heeling angle. The uncoupled case highlights the importance of the vessels ability to adjust to the motions of the lifted object, as the allowable sea state decreases.

Acknowledgements

This thesis serves as a final closure of my Master of Science in Marine and Offshore Technology at the University of Stavanger. The work has been performed in cooperation with my employer, DeepOcean, between January and June 2021. This work has been rewarding and a great learning experience.

First of all, I would like to thank my supervisor Associate Professor Lin Li, for her enthusiasm and support throughout the entire project. Continuous guidance and follow-up inspired me to keep a steady progress from start to finish. She offered valuable advice and mentoring whenever it was needed. Furthermore, I would like to thank several of my colleagues at DeepOcean for valuable discussions and guidance. I appreciate that Anders Haga and Anders Vikebø shared their experiences at the University. I benefitted greatly from discussions about numerical modeling with Dag Abel Sveen and Roger Jensen. Gustav Vik, Roger Hunsbedt and Anita Åkre took their time to proofread my work, and for that I am very grateful.

The main analyses and simulations carried out in this thesis have been performed in Orcawave and Orcaflex and further post-processed in Excel. I would like to extend my gratitude to Orcina for providing me the software license and for answering questions regarding analysis and simulation setup.

Nils Olav Hauge

Haugesund, June 2021

Abbreviations

AHC	Active Heave Compensation
BBC	Bottom Boundary Condition
COG	Center of Gravity
CFD	Cumulative Distribution Function
DFSBC	Dynamic Free Surface Boundary Condition
DHL	Dynamic Hook Load
DNV	Det Norske Veritas
GEVD	Generalized Extreme Value Distribution
GL	Germanischer Lloyd
ITS	Integrated Template Structure
JONSWAP	Joint North Sea Wave Project
KFSBC	Kinematic Free Surface Boundary Condition
LARS	Launch and Recovery System
PDF	Probability Density Function
PLET	Pipeline End Termination
RAO	Response Amplitude Operator
ROV	Remotely Operated Vehicle
SPS	Subsea Production System
SWL[1]	Still Water Level
SWL[1]	Safe Working Load
TMS	Tether Management System
WBC	Wall Boundary Condition

---

[1] Commonly used for both Still Water Level and Safe Working Load.

Contents

List of Figures

List of Tables

Chapter 1

Introduction

1.1   Background and Motivation

As oil and gas fields move further offshore and to deeper waters than earlier, new methods for recovery of petroleum develop. A method to compensate for the increasing water depth is to move the production system down to the seabed [2]. This is often referred to as a subsea production system (SPS). Such a system may consist of [2]:

- Xmas trees and wellhead systems.
- Tie-in and flowline systems.
- Control systems.
- Umbilical and riser systems.
- Manifold and jumper systems.

The subsea control system is the control system that operates the subsea production system during production operations [3]. It operates the chokes and valves on the manifold/templates, xmas trees and pipelines. Data is being received and transmitted between surface and subsea to enable the operator to monitor the status of the production [2].

Subsea manifolds are used in development of subsea fields to simplify the subsea part of the system. This reduces the number of pipelines and risers which either connects the subsea system to the surface system or serves as infield connections between the various subsea equipment [2]. To contain the pressure from the well at the seabed a wellhead is mounted at the end of the production casings (simplified explanation). This wellhead also serves as an interface for well completion activities, testing of all subsea operation phases and drilling of the well [2]. On top of the well head is the xmas tree. It contains several pipes, fittings, sensors and valves to control the production flow, control injection to the well or to monitor the system. The xmas trees can be controlled by the subsea control system or manually by a diver or an ROV [2]. The control fluid or electrical signals from the surface, if the xmas tree is controlled from surface,

are transported through an Umbilical. The umbilical is a bundled arrangement of tubing, piping, and/or electrical conductors.

Jumpers are typically used to connect subsea components, such as freestanding wells to manifolds, between manifolds or from manifold to a pipeline end termination [2]. This is a short pipe connector which transports fluid between the two components. Other components with larger distance between them are connected using flowlines. The flowlines can either be flexible pipes or rigid pipes. The subsea production system is connected to the surface system using risers [2].

A typical subsea production system with its components, and the relationship among them, is presented in Figure 1-1.
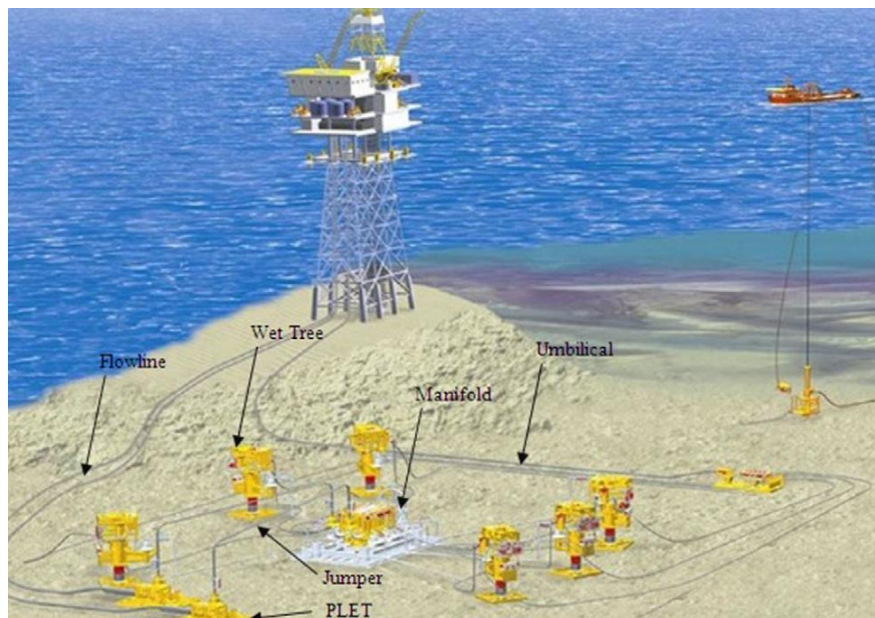
Figure 1-1: Typical subsea production system [2].

The wells in a subsea production system can either be arranged separately, like the wet trees in Figure 1-1, or gathered together with a manifold in an integrated template structure (ITS). An ITS during deployment, just prior to crossing the splash zone, is shown in Figure 1-2. This template has the capability to be the foundation for a manifold and four wellheads with each their xmas tree. A typical ITS consists of a several components. The steel framework serves as a support for the other components. The purpose of the ITS is to provide a stable foundation on seabed for the wellheads and ancillaries connected to it. Tailpipes are located in the center of where the wellheads are installed to protect against soil layer collapse for drilling activities [2]. Covers or hatches are mounted on top of the structure to protect against impact from falling objects and to guide fishing gear safely over the structure. One suction anchor is normally fitted in each corner of the template to restrain the template both horizontally and vertically after it has been installed [2].

They are designed to penetrate the soil on the seabed by utilizing both the weight of the template itself and pumps which create a vacuum inside the suction anchor [4].

Figure 1-2: ITS deployment at Snorre field [Source: DeepOcean]

Installation of the subsea production system involves hazards and high risks because of the harsh nature and uncertainty around the marine environment [5]. This study focuses on the installation of the subsea template. Handling the uncertainties and risk related to the installation phase offshore equipment such as templates requires engineering analytical work [6]. Numerical models are often implemented in the analysis of various phases of the offshore operation to determine operational limitations which maintain a desired level of confidence that an accident is avoided. Allowable sea state limits for the offshore operations are determined through detailed numerical analysis of the different phases before comparing the critical responses and the respective allowable limits [6]. Normally a combination of significant wave heights and spectral peak periods where the probability of success for the operation is estimated to be above a certain limit are defined [6].

Deployment of a subsea template, or any similar offshore lifting operation, can be divided into multiple phases. DNV describes the following phases as the main phases of a deployment operation [1] & [7]:

- Pre-lift.
- Lift-off.
- Over-boarding.
- Splash zone crossing
- Lowering
- Vessel positioning
- Landing

The pre-lift phase is when the vessel has reached is designated location and the operation is ready to start. The object is then lifted off either the vessel's own deck or a separate vessel used for transportation of the object. The over-boarding phase is related to lifting the object off the vessel's own deck. At this phase the object is translated horizontally from its position on deck to the lowering position. The object is then lowered through the splash zone where it is directly exposed to wave kinematics. After being lowered through the splash zone the crane pays out until the object is just above the seabed. Prior to the object being landed on seabed the vessel repositions to make sure the object is landed on its deployment point.

Each of the seven above-mentioned phases are subject to engineering prior to offshore execution to make sure an acceptable probability for a successful operation is achieved. This thesis focuses on analyzing the splash zone crossing. This phase is considered one of the most critical [8]. It is essential that the hydrodynamic loads acting on the object during lowering is estimated as accurately as possible to achieve a realistic numerical model. Achieving a realistic numerical model, and accurately predicting the induced motions and slamming loads acting on the object during splash zone crossing is challenging because of the transient effects that occurs as the object reaches the free surface [8]. An accurate numerical model is essential to minimize the chance that the crane wire will become overloaded or slack [9]. DNVGL-RP-N201 presents the following potential consequences of lowering an object through the splash zone, which must be addressed during planning of the offshore operation [7]:

- Damage to the object itself due to slamming loads.
- Snap forces acting on the lifting wire after the wire has become slack.
- Shift of object due to change in position of centre of buoyancy.

Subsea operations are primarily performed by Remotely Operated Vehicles (ROVs). They can either assist during deployment operations such as deployment of the template mentioned above, or perform maintenance inspection or repair to an existing subsea asset [2]. ROVs are often deployed from a surface vessel, making the operation weather dependent. The ROVs can be deployed over the side of the vessel, down a moonpool or even at the stern of the vessel. A typical Launch and Recovery System (LARS) is presented in Figure 1-3. A system for launch and recovery over the side of a vessel normally consists of a ROV connected to a tether management system (TMS) which is connected to a lifting wire (umbilical). The lifting wire is running through a sheave on the LARS frame and spooled onto a winch. The winch usually has some sort of heave compensating system to counteract some of the heave motion at the tip of the LARS frame. The LARS frame transports the ROV from the vessel deck to the deployment/recovery position. The LARS in this study is located at the stern of the vessel.

Lifting through the splash zone is considered the most critical phase during launching and recovery of ROVs [10]. At this stage the lifting wire can become slack and experience large snap loads. The capacity of the wire sets limitations for when the launch and recovery can happen. From an economic perspective it is beneficial to have the range of allowable sea conditions as wide as possible and reduce the amount of waiting on weather. DNV's recommended practice for modeling and analysis of marine operations [1] allows for alternative methods, such as time domain simulations, to determine operational limitations.
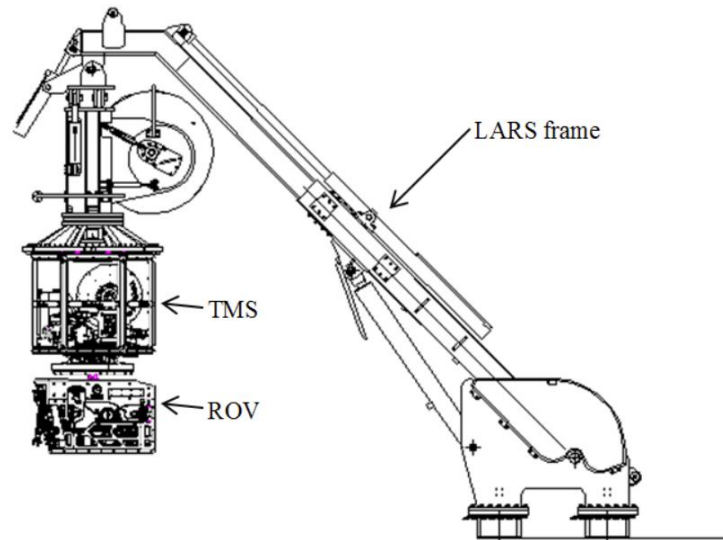
Figure 1-3: Typical ROV Launch and Recovery System [11].

1.2   **State of the Art**

Lifting operations are described in many regulations and standards. The main source of information for Norwegian based offshore companies is the DNVGL standards [11]. DNVGL is a company consisting of the former Det Norske Veritas (DNV) and Germanischer Lloyd (GL). They have produced a standard which "[…] is intended to ensure marine operations are designed and performed in accordance with recognized safety levels and to describe "current industry good practice". [5]. This standard replaces the legacy DNV-OS-H-series and refers to other standards and recommended practices such as "Modeling and Analysis of Marine Operations [1]. This recommended practice gives guidance for lifting operations through the splash zone and lowering of objects down to the seabed. The objective of the "lifting through wave zone" part of the document is to improve modelling and analysis methods to obtain more accurate prediction of design loads. The document also provides a simplified method for estimation of the hydrodynamic forces.

Time domain simulation software can be used to predict loads and motions. There are several different software capable of running time domain simulations for marine applications. Orcaflex, SIMO and Ansys are examples of software which can be used for marine operations. The hydrodynamic properties of the vessels in those time domain simulation software can be obtained from frequency domain analysis software. Some examples which uses potential flow theory are Orcawave, Wadam, and Ansys AQWA. This study uses Orcawave and Orcaflex.

Splash zone crossing has been addressed in several other studies. Min Wu conducted a dynamic analysis of a subsea module during splash zone transit [12] and discovered that the tension in the lifting wire under dynamic analysis could increase to more than twice the static tension. The results also show that, in general, the template will experience a significant drift in the same direction as the induced wave direction.

The effect of shielding during splash zone crossing has been investigated by Li et al. for lowering of an offshore wind turbine monopile from a floating installation vessel [13]. The conclusion from the study was that responses can be greatly overestimated if the shielding effect is not accounted for in the numerical analysis of offshore operations. As a result of this the weather window can be conservatively estimated, which may lead to unnecessary economic consequences. The day rate of the installation vessel and its crew and the standby cost for a production system not in production are typical examples of large expenses when waiting on weather. A study on lowering of a large spool piece through the splash zone conducted by Li et al. [8], on the other hand, concludes that excluding the shielding effect may also overly estimate the operability. Overly estimating the operability could potentially lead to an accident. This conclusion is drawn because the shielding effect creates a variation in wave kinematics along the large spool piece.

Like the ITS deployment in this study, Amer presents a study on an ITS deployment covering both over-boarding and lowering through the splash zone [14]. The lowering through the splash zone with and without including the shielding effect is compared and the conclusion is that including the shielding effect will result in higher allowable sea states. This study addresses a similar type of object to be lowered and a similar vessel which lowers the object, but different parameters are investigated. Amer's thesis does not account for the altered response amplitude operators when the vessel has a heeling angle during deployment. Few studies on the difference between modeling the numerical model as uncoupled and coupled are available.

Operational limits for lifting operations has been addressed in multiple papers. A general method for assessment of the operational limitations demonstrated in a case study for installation of an offshore wind turbine monopile is presented in a journal paper by Guachamin-Acero et al [15]. Li et al. [16] performed a case study on lifting operation to study the uncertainties in allowable sea states associated with the sea state description used in the numerical analysis. Guachamin-Acero and Li [17] have presented a general methodology to assess the uncertainty in significant wave height limits due to variability in wave spectral energy distribution. The case that the study used to assess the uncertainties is installation of an offshore wind turbine transition piece. All the three papers on allowable sea sate and operational limitations are relevant for this thesis, as the majority of the discussion is based on the allowable sea states.

Lifting ROVs through the splash zone has been addressed before in other published work. Bjerkholt [10] presents a study of lifting an ROV through the splash zone with the construction vessel Edda Flora. The simplified method in DNV's recommended practice is compared to time domain simulations conducted in Orcaflex and SIMO. The results show that time domain simulations are a good alternative to the simplified method for the ROV lift operation. The lift in that study falls within the light lift operation category in DNV's recommended practice [1], and the external load's influence on the vessel motion is therefore neglected.

Other studies involving motion analysis have been conducted before. Wu and Moan [18] have investigated the dynamic behavior of an anchor handling vessel during anchor deployment. Their motivation for carrying out the study was previous incidents where the anchor handling vessel capsized. Their study resembles this study since the anchor chain enters the sea from the stern of the vessel when being deployed/retrieved. A coupled SIMO-RIFLEX numerical model was established to capture the interaction between the body(vessel) and the slender structures(chain). One of

their proposals for future work was to investigate the initial heel and trim angle's effect on the hydrodynamic properties of the vessel. This thesis focuses on the initial trimming angles effect on the ROV deployment.

A lot of published work is available for modeling and analysis of marine operations, covering different aspects of the operation. Sound knowledge is important to be able to simulate real-life events as accurately as needed. Knowledge is also the key to determine system boundaries and to make reasonable assumptions and simplifications. This thesis aims to increase knowledge around the influence of the vessel inclination during splash zone crossing.

1.3   **Aim and Scope**

The general scope of this thesis is to evaluate the allowable sea states for a number of different cases by analyzing different numerical models in the time domain simulation software Orcaflex. The numerical model in Orcaflex will be based on hydrodynamic properties acquired through a frequency domain analysis in Orcawave. An overview of the different steps and the link between them is provided in Figure 1-4. The thesis focuses on two different vessels doing each their lifting operation. First the hydrodynamic properties of the vessel must be generated using diffraction analysis. The hydrodynamic properties shall then be included in the numerical model in the time domain simulation along with the hydrodynamic properties for the lifted object which are found by simplified calculations from a recognized standard. The dynamic responses from the time domain simulation shall be used as a basis for the statistical modeling before comparing with the predefined limiting criteria. The aim for the thesis is to draw a conclusion based on comparison of the allowable sea states for the cases mentioned below. The scope for the ROV deployment is to investigate how an initial trimming angle affects the allowable sea states and the scope for the ITS deployment is to investigate how an initial heeling angle affects the allowable sea states.

❖ **Diffraction analysis**

➢ ROV deployment vessel

▪ Generate displacement RAO for even keel and trimmed conditions.

➢ ITS deployment vessel

▪ Generate displacement RAO for upright and heeling conditions.

▪ Generate load RAO for upright and heeling conditions.

▪ Generate sea state RAO for consideration of shielding effects.

❖ **Time domain simulation**

➢ ROV Deployment

▪ Determine allowable sea state for deployment through splash zone at even keel.

▪ Determine allowable sea state for deployment through splash zone with 3,66 degrees trimming angle.

➢ ITS Deployment (Load RAO)

▪ Determine allowable sea state for deployment through splash zone at upright position.

▪ Determine allowable sea state for deployment through splash zone with 3 degrees heeling angle.

▪ Analyse dynamic responses for deployment through splash zone at upright position with increased roll response.

➢ ITS Deployment (Displacement RAO)

▪ Determine allowable sea state for deployment through splash zone at upright position.
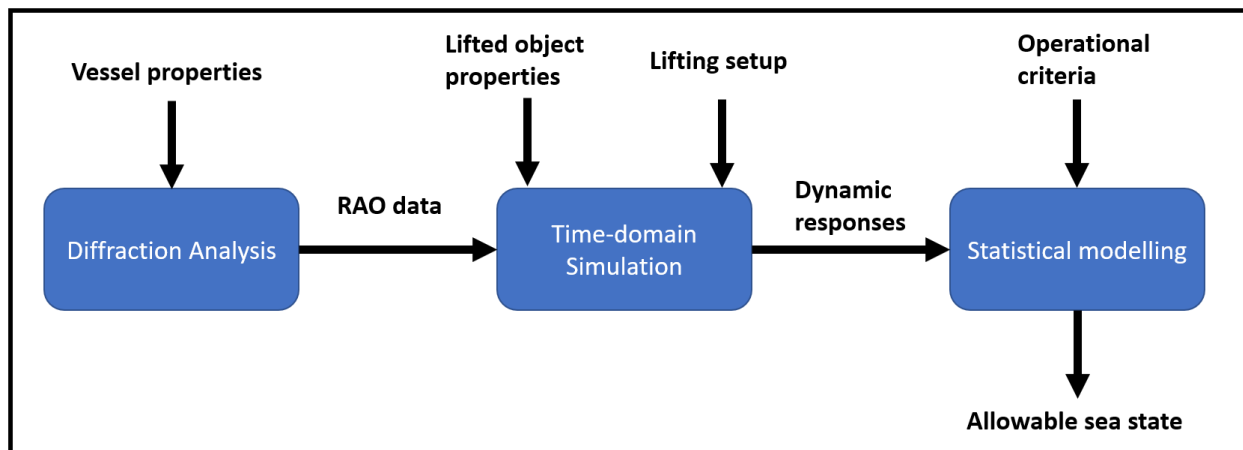
Figure 1-4: General scope of thesis.

1.4   **Outline**

The report is divided into 9 chapters with each their subchapters. The aim is to create a seamless transition from the introduction to the conclusion.

Chapter 1 presents an introduction of the study, where the background and motivation for conducting this study is briefly presented. An introduction to the two objects being lowered through the splash zone and the challenges related to this operation is covered in this chapter. A literature review of previous work and relevant standards is also conducted and presented in this chapter.

Chapter 2 provides an overview of the theory behind the analysis method and the time domain simulation method. It explains ocean waves, their influence on structures, motions for bodies free-floating in fluid and an introduction to statistical modeling.

In Chapter 3 the numerical models in Orcawave are discussed. The assumptions and simplifications in the models, as well as the setup and the parameters used are stated in this chapter.

Chapter 4 discusses the results obtained from the diffraction analysis in Orcawave. The shielding effect present on the leeward side of the ITS deployment vessel is also presented in this chapter.

Chapter 5 presents the numerical models used to run time domain simulations. Extra attention is paid to the modeling of the hydrodynamic properties of the lifted objects.

Chapter 6 and Chapter 7 presents and discusses the results from the time domain simulations of the respectively the ROV deployment and the ITS deployment. These two chapters compare the difference between the results from the cases within each their deployment

Chapter 8 discusses the similarities and differences between the results from the two deployment analyses.

The conclusion of this study and recommendations for future work is given in Chapter 9.

Chapter 2

Theory

This study uses frequency domain analysis and time domain simulations to obtain results. The frequency domain analysis software Orcawave is based on potential flow theory. Potential flow theory is described in this chapter, both in relation to the description of ocean waves and in relation to the motion of free-floating bodies in fluid. The chapter starts with the theory behind ocean waves before explaining their influence on structures. The basis for estimating the wave force on the slender elements in the time domain simulation is given in this chapter. A brief explanation of how time domain simulating software solves the equation of motion and the statistical modeling of the results from the time domain simulations is presented in the end of the chapter.

2.1   Waves

Waves can be created in various ways [19]:

- Generated by a floating structure, either by forward movement or an oscillating movement
- Generated by the tides
- Generated by wind interactions with the sea surface
- Generated by landslides or earthquakes

There is no simple mathematical way to describe ocean surface waves and their interaction with structures. A realistic image of the sea surface contains non-repeating, time-changing wave lengths and crests/troughs. Superpositioning of linear waves can be used to describe irregular waves. Linear wave theory lays the foundation for calculation of surface wave profiles used in ocean and coastal engineering and naval architecture. Despite ocean waves being categorized as irregular waves, long period swells can be described accurately with linear wave theory [19].

2.1.1 **Potential Flow Theory**

Potential (non-rotational) flow theory assumes the water to be an ideal, incompressible, fluid with no shear forces between particles. This is a valid assumption for water not being in proximity to the seabed or any structure [19]. No rotation, or no curl, means that the cross product between the gradient, ∇, and the velocity, $\vec{U}$, is zero.

$$\vec{U} = (u, v, w) \tag{1}$$

$$\nabla \times \vec{U} = \begin{vmatrix} \vec{i} & \vec{j} & \vec{k} \\ \frac{\delta}{\delta x} & \frac{\delta}{\delta y} & \frac{\delta}{\delta z} \\ u & v & w \end{vmatrix} \tag{2}$$

The partial derivatives of the potential function, φ, gives the flow velocity in their respective directions. The velocity can be written as Equation (3).

$$\vec{U} = \left(\frac{\delta \varphi}{\delta x}, \frac{\delta \varphi}{\delta y}, \frac{\delta \varphi}{\delta z}\right) \tag{3}$$

The fluids identification as incompressible can be used to derive the Laplace differential equation of second order for the potential function (Equation (6)).

$$\nabla \cdot \vec{U} = 0 \tag{4}$$

$$\frac{\delta}{\delta x}\left(\frac{\delta \varphi}{\delta x}\right) + \frac{\delta}{\delta y}\left(\frac{\delta \varphi}{\delta y}\right) + \frac{\delta}{\delta z}\left(\frac{\delta \varphi}{\delta z}\right) = \frac{\delta^2 \varphi}{\delta x^2} + \frac{\delta^2 \varphi}{\delta y^2} + \frac{\delta^2 \varphi}{\delta z^2} = 0 \tag{5}$$

$$\nabla^2 \varphi = 0 \tag{6}$$

To solve the Laplace equation boundary conditions must be set. Four types of boundary conditions are particularly useful for potential flow theory [19]:

- Bottom boundary condition
- Wall boundary condition
- Kinematic free surface boundary condition (KFSBC)
- Dynamic free surface boundary condition (DFSBC)
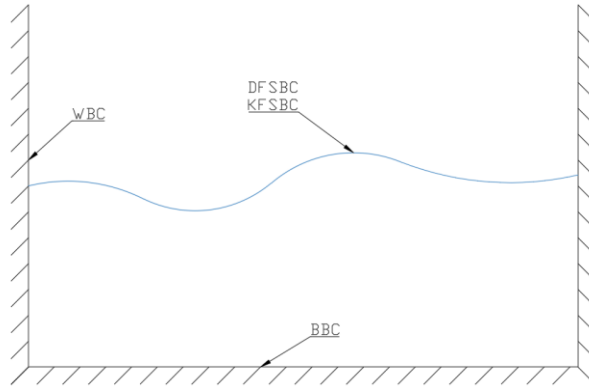
Figure 2-1: Boundary conditions

The Bottom boundary condition and Wall boundary condition resemble each other. They restrict the flow from passing through the seabed and walls, respectively. Walls can typically be the hull of a vessel or a structure located in the water, either standing still or moving. The surface boundary conditions define that no water can flow through the surface. The ever-adjusting surface profile, ξ, makes sure that the surface boundary condition is always satisfied.

According to the KFSBC water particles at the free surface always remains at the free surface. The vertical velocity at the free surface can be expressed using a two-dimensional description of the surface [19].

$$z = \xi(x, t) \tag{7}$$

$$w = \frac{\delta\varphi}{\delta z} = \frac{dz}{dt} = \left(\frac{\delta z}{\delta t} + u\frac{\delta z}{\delta x}\right) = \left(\frac{\delta\xi}{\delta t} + u\frac{\delta\xi}{\delta x}\right) \tag{8}$$

The DFSBC states that "the pressure at the free surface is constant and equal to the atmospheric pressure" [19]. The Bernoulli equation describes the pressure variations in a fluid.

$$\frac{P}{\rho} + gz + \frac{\delta\varphi}{\delta t} + \frac{1}{2}(u^2 + w^2) = C(t) \tag{9}$$

By utilizing that the constant $C(t)$ can be any convenient constant, the Bernoulli equation can be rewritten for the surface pressure [19].

$$\left(gz + \frac{\delta\varphi}{\delta t} + \frac{1}{2}(u^2 + w^2)\right)\Bigg|_{z=\xi} = 0 \tag{10}$$

The boundary conditions in the potential flow theory can be used to express surface elevation for waves. Removing the terms in the equations with orders of magnitude higher than 1 gives linearized surface conditions and hence linear/regular waves. Solving the Laplace equation without removing the higher order terms obtains higher order wave theories. Higher order wave theories are in general more representative of real ocean waves, with higher peaks than

in linear wave theory [19]. Sinusoidal waves obtained from the linear wave theory are easier to calculate by hand, but only valid under the assumption of small wave amplitude compared to wave length [19].

2.1.2 **Regular Waves**

Function (11) defines the surface profile for harmonic (regular) waves. The surface profile is derived from the potential function, using the DFSBC and the KFSBC. By removing the higher order term $u(\delta\xi/\delta x)$ from Equation (8), and assuming that the velocity at the surface is approximately the same as the velocity at the still water level, the linearized KFSBC is formed. Applying the same two linearizing measures to the DFSBC gives the linearized boundary condition version, as seen in Equation (13).

$$\xi(x,t) = \xi_0 \sin(\omega t - kx) \tag{11}$$

$$\left.\frac{\delta\varphi}{\delta z}\right|_{z=0} = \frac{\delta\xi}{\delta t} \tag{12}$$

$$\xi = -\frac{1}{g}\frac{\delta\varphi}{\delta t}\bigg|_{z=0} \tag{13}$$

Combining the two surface conditions gives the basis for the derivation from the Laplace equation to the velocity potential.

$$\frac{\delta^2\varphi}{\delta t^2} + g\frac{\delta\varphi}{\delta z} = 0 \tag{14}$$

$$\varphi(x,z,t) = \frac{\xi_0 g}{\omega}\frac{\cosh k(z+d)}{\cosh(kd)}\cos(\omega t - kx) \tag{15}$$

ω = Angular frequency

d = Water depth

k = Wave number

ξ_0 = Wave amplitude

The relation between the velocity profile at SWL, where $z = 0$, and the linearized DFSBC yields the equation for the sinusoidal wave (Equation (17)).

$$\xi = -\frac{1}{g}\frac{\delta}{\delta t}\left(\frac{\xi_0 g}{\omega}\frac{\cosh(kd)}{\cosh(kd)}\cos(\omega t - kx)\right) \tag{16}$$

$$\xi(x,t) = \xi_0 \sin(\omega t - kx) \tag{17}$$

2.1.3 **Irregular Waves**

As mentioned, irregular waves give a more realistic description of the actual ocean waves. There is a continuous variation in length and wave height [20]. Important parameters in the description of irregular waves are the average zero up-crossing period and the significant wave height. Zero up-crossings are when the time history graph of a wave train crosses the SWL on its way upwards [21]. The significant wave height is the average of the 1/3 highest waves in a record [20].

Recording a series of waves with a large number of samples and statistically analyzing the surface elevation indicates that the surface elevation fits the Gaussian distribution quite well [20]. The standard deviation of the surface elevation is directly related to the significant wave height and follows the form given in Equation (18).

$$\sigma = \sqrt{\frac{1}{N-1}\sum_{n=1}^{N}\zeta_n^2} \tag{18}$$

$$\sigma = \frac{H_s}{4} \tag{19}$$

The wave amplitude or global maxima statistics will follow a Rayleigh distribution if the surface elevation process is narrow banded [21]. The surface elevation can be considered narrow banded if the range of frequencies in the wave field is not too large.

$$F_{C_G}(c) = 1 - e^{-\frac{1}{2}\left(\frac{c}{\sigma_\Xi}\right)^2} \tag{20}$$

Equation (20) is the cumulative distribution function for the global maxima. For at a time interval that contains N global maxima the distribution of the largest global maxima will also follow the Rayleigh distribution. This is true under the assumptions that the global maxima are identically Rayleigh distributed and that they are statistically independent [21].

$$F_{C_N}(c) = F_{C_{G1}}(c) * F_{C_{G2}}(c) * F_{C_{G3}}(c) \dots * F_{C_{GN}}(c) = \left[F_{C_N}(c)\right]^N \tag{21}$$

$$F_{C_G}(c) = \left[1 - e^{-\frac{1}{2}\left(\frac{c}{\sigma_\Xi}\right)^2}\right]^N \tag{22}$$

The distribution of the largest crest height can for example be used to determine the expected largest value for a given number of waves, N. It can also be used to calculate the probability of exceedance.

The wave periods play an important part in the description of waves. Fourier series analysis can be used to study a recorded superposition of a series of sinusoidal waves [20]. This can be used to create a spectrum showing the density

of each wave frequency. The Fourier series for the sea surface elevation can be written as Equation (23), and rewritten to Equation (24) [21]. The following relations are used:

$$\xi(t) = \sum_{n=1}^{\infty} \left[a_n cos \frac{2n\pi}{T} t + b_n sin \frac{2n\pi}{T} t \right] \tag{23}$$

$$\xi(t) = \sum_{n=1}^{\infty} \xi_n cos(\omega_n t - \theta_n) \tag{24}$$

$\xi_n = \sqrt{a_n^2 + b_n^2}$

$\theta_n = \arctan \left(\frac{a_n}{b_n} \right)$

$\omega_n = \frac{2n\pi}{T}$

By letting the phase angle, θ_n, be a uniformly distributed random variable the wave elevation can be considered a stochastic process [21]. As previously mentioned, the surface elevation fits the Gaussian distribution quite well. This means that the variance is the standard deviation squared. Calculating the variance of one regular wave component proves the existence of Equation (19). The wave spectrum is defined as Equation (27), utilizing that a stationary Gaussian process is characterized by the auto-correlation function $R_{\Xi\Xi}(\tau)$, and the relation between the auto-correlation function and the spectral density, $S_{\Xi\Xi}(\omega)$ [21].

$$\Xi_n(t) = \xi_n cos(\omega_n t - \Theta) \tag{25}$$

$$Var[\Xi_n] = \sigma_{\Xi_n}^2 = \frac{1}{2} \xi_n^2 \tag{26}$$

$$S_{\Xi\Xi}(\omega_n) * \Delta\omega = \sum_{\omega_n}^{\omega_n + \Delta\omega} \frac{1}{2} \xi_n^2(\omega) \tag{27}$$

$\Delta\omega$ is the difference between two successive frequencies. By letting the frequency step approach zero, the definition of the wave spectrum can be written as Equation (28) [20].

$$S_{\Xi\Xi}(\omega_n) * d\omega = \frac{1}{2} \xi_n^2 \tag{28}$$
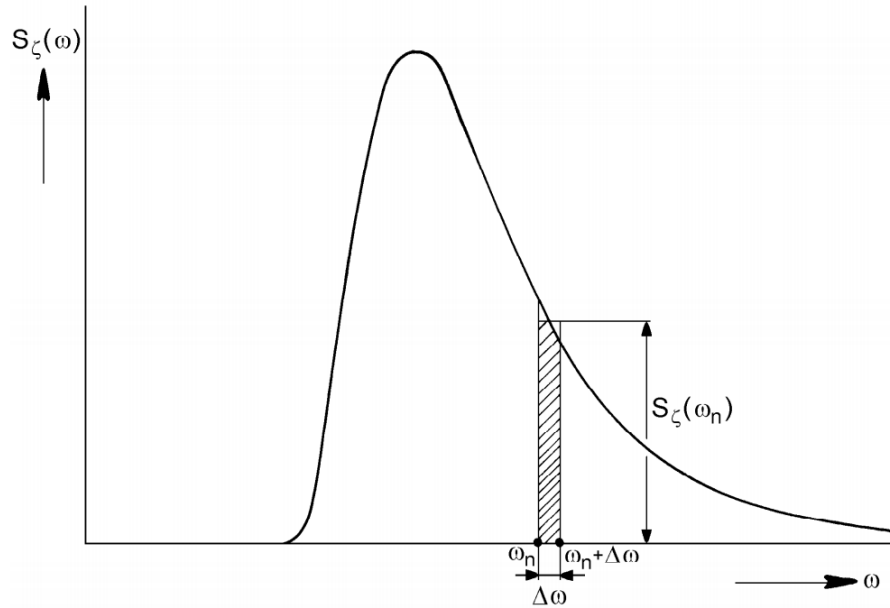
Figure 2-2: Typical wave spectrum [20]

The wave frequency spectrum is based on statistics just like wave height statistics. Several projects have been conducted in an attempt to describe the spectrum in a standard form [21]. This has resulted in several mathematical formulations for normalized uni-directional waves. The mathematical formulations are based on two parameters; significant wave height, H_s, and the peak period, T_p [21]. Two wave spectrums are presented here: the Pierson-Moskowitz spectrum and the JONSWAP spectrum.

Pierson-Moskowitz

The Pierson-Moskowitz spectrum assumes that the considered sea state is fully developed. The original Pierson-Moskowitz spectrum was a one-parameter spectrum based on the average wind speed measured at a 19,5 m height above sea level [21]. Later the spectral shape has been re-parameterized to include both the significant wave height and the peak period. The spectrum given in hertz is defined as Equation (29).

$$S_{\Xi\Xi}(f) = 0.3125H_s^2 * T_p^{-4} * f^{-5} * e^{\left(-1.25T_p^{-4}*f^{-4}\right)}$$
(29)

JONSWAP

The Joint North Sea Wave Project, a wave measurement program carried out along a line extended over 100 miles into the North Sea from Sylt Island, took place in 1968 and 1969 [21]. This resulted in a mathematical formulation for a growing wind sea (fetch-limited/coastal). The spectrum given in angular frequency is defined as Equation (30)

$$S_{\Xi\Xi}(\omega) = \frac{320 * H_s^2}{T_p^4} * \omega^{-5} * e^{\left(\frac{-1950}{T_p^4} * \omega^{-4}\right)} * \gamma^A \tag{30}$$

$$A = e^{-\left(\frac{\frac{\omega}{\omega_p}-1}{\sigma\sqrt{2}}\right)^2}$$

γ = Peak shape parameter

ω_p = Angular frequency at spectral peak, $\frac{2\pi}{T_p}$

$$\sigma = \begin{cases} 0.07, & if\ \omega < \omega_p \\ 0.09, & if\ \omega > \omega_p \end{cases}$$

According to the simplified analysis method in DNV's recommended practice for modeling and analysis of marine operations [1], the range of mean zero up-crossing periods can be defined as Equation (31). An increment of 1 second is in most cases sufficient according to the simplified method.

$$8,9 \cdot \sqrt{\frac{H_s}{g}} \leq T_z \leq 13 \quad [s] \tag{31}$$

The peak shape parameter can be calculated according to section 2.2.6.9 in DNV-RP-H103 [1]. The parameter is related to the spectral peak period and the significant wave height and can be written as Equation (32). The spectral peak period is related to the zero-up-crossing period as described in Equation (33). This is only valid for $1 \leq \gamma \leq 7$.

$$\gamma = \begin{cases} 5 & ;\dfrac{T_p}{\sqrt{H_s}} \leq 3,6 \\ e^{5,75-\frac{1,15T_p}{\sqrt{H_s}}} & ;3,6 \leq \dfrac{T_p}{\sqrt{H_s}} \leq 5 \\ 1 & ;5 \leq \dfrac{T_p}{\sqrt{H_s}} \end{cases} \tag{32}$$

$$\frac{T_z}{T_p} = 0,06673 + 0,05037\gamma - 0,006230\gamma^2 + 0,0003341\gamma^3 \tag{33}$$

A directional short-crested wave spectrum can be described as the product of a unidirectional wave spectrum and a spreading function. This function is often simplified such that the directional function only depends on the angle between the elementary wave trains and the direction of the short-crested waves [1].

$$S(\omega, \theta) = S(\omega)D(\omega, \theta) = S(\omega)D(\theta) \tag{34}$$

The directional function for wind seas is commonly described as Equation (35), where θ_p is the primary direction, θ is the direction of the short-crested waves and n is a spreading coefficient. The expression shows that when the

spreading coefficient increases the spreading decreases. Typical spreading coefficient values for wind waves are between 2 and 4. For swell, a spreading coefficient above 6 is more appropriate [1].

$$D(\theta) = \frac{\Gamma\left(1 + \frac{n}{2}\right)}{\sqrt{\pi}\Gamma\left(\frac{1}{2} + \frac{n}{2}\right)} \cos^n\left(\theta - \theta_p\right) \tag{35}$$

$$\left|\theta - \theta_p\right| \leq \frac{\pi}{2} \tag{36}$$

Both wave spectrums can be converted between frequency and angular frequency using relation (37).

$$f = \frac{\omega}{2\pi} \tag{37}$$

Reversing the information given in this subchapter results is a method for creating a deterministic time record of water surface elevation. The time series is needed to solve non-linear problems (the software Orcaflex has, in this study, been used for these non-linear problems) [22]. The wave record generated based on the measured wave record is statistically identical and contains the same amount of energy [20]. The wave history does, however, differ due to different phase angles. The surface elevation can be written as Equation (38)

$$\xi(t) = \sum_{n=1}^{N} \xi_n \cos(k_n x - \omega_n t + \epsilon_n) \tag{38}$$

The amplitude, ξ_n, is determined from the wave spectrum using Equation (28). The wave number, k_n, can be found using the dispersion relation from linear wave theory [19]. The phase angle is a uniformly distributed, random variable, which is the reason for the mentioned difference in wave history [20].
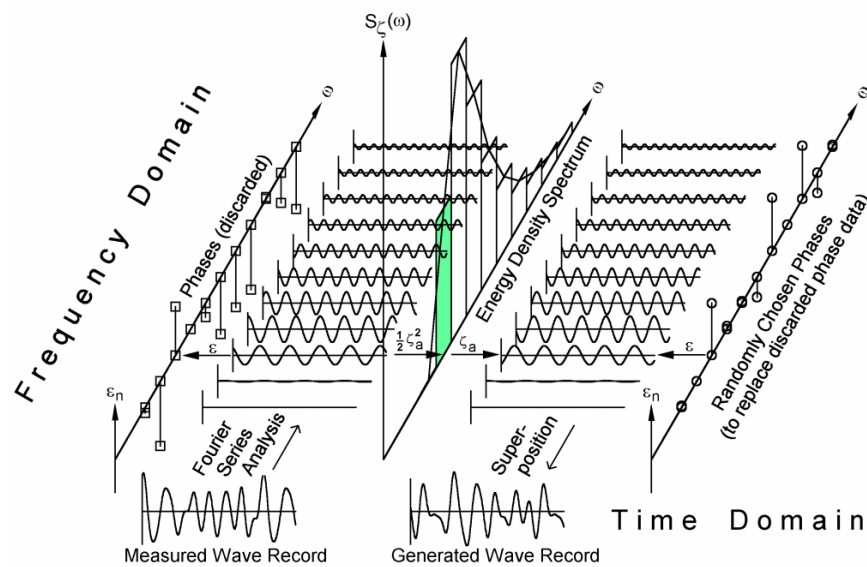
Figure 2-3: Wave record analysis and regeneration [20].

2.2 Rigid Body Motions in Waves

This chapter describes the motion of rigid bodies exposed to sea surface elevations. Irregular motion is described as a series of different regular motions [20]. Potential flow theory gives the basis for determination of motions in different sea states.

2.2.1 Rigid Body Dynamics

The motion of a structure floating in fluid has irregular characteristics. Just like the irregular waves, the irregular motions of a floating structure can be described as a superposition of linear motions [20]. Motion components can be obtained for a range of frequencies. The linear property means that for each motion component (at one frequency) the ratio between the wave amplitude and the motion amplitude remains constant. The phase angle will also remain constant. The amplitudes of the motions in the frequency domain relative to the wave amplitudes gathered together is called RAO data. RAO, or Response Amplitude Operator, is an operator which multiplied by the wave amplitude gives the motion amplitude [20]. Each frequency has its own operator and phase angle.

$$\frac{z_a}{\xi_a}(\omega) \tag{39}$$

z_a = Heave motion amplitude

ξ_a = Wave amplitude

The RAO can be used to determine the response spectrum by utilizing the transfer function between the wave spectrum and the motion [20].

$$S_z(\omega) = \left|\frac{z_a}{\xi_a}(\omega)\right|^2 \cdot S_\xi(\omega) \tag{40}$$

This gives the heave response in irregular waves. The RAO, $\frac{z_a}{\xi_a}(\omega)$, represents the relation between the wave amplitude and the heave amplitude for each frequency. The wave spectrum, $S_\xi(\omega)$, contains several regular wave components with each their amplitude, phase shift and frequency. Figure 2-4 shows the principle of how the time history for irregular waves is turned into a time history for the irregular response.
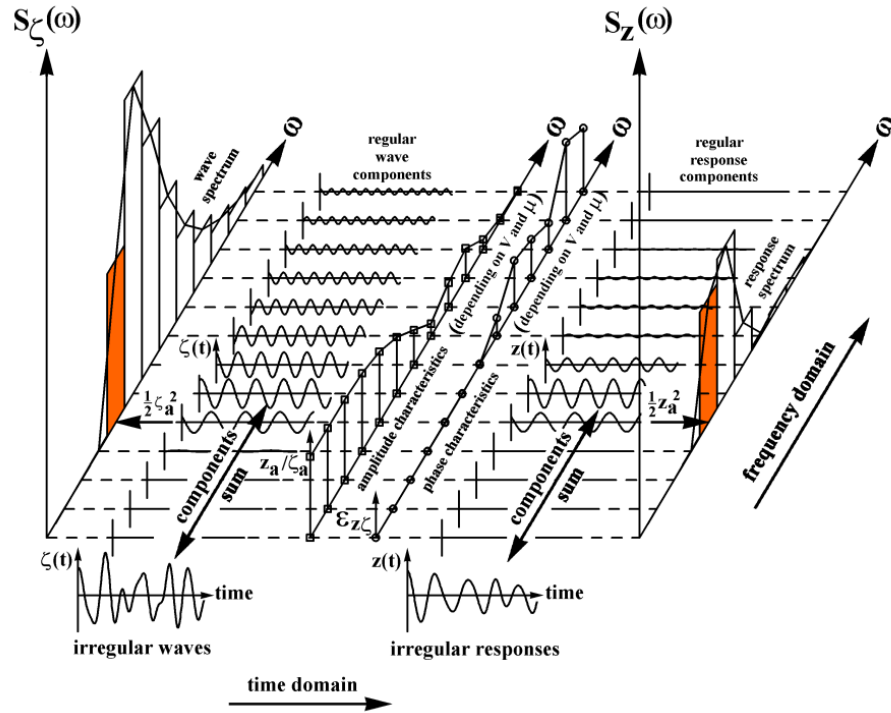
Figure 2-4: Principle of transfer of waves into responses. [20]

The motion of rigid bodies floating in fluids can be described using the equation of motion. The equation of motion can be written both for translations and rotations [23]. Equation (41) applies to a damped mass-spring translating system not exposed to external loads (single-degree-of-freedom). Equation (42) applies to a rotational system.

$$(m + a)\ddot{x} + c\dot{x} + kx = 0 \tag{41}$$

$$(m + a)\ddot{\phi} + c\dot{\phi} + k\phi = 0 \tag{42}$$

m = Object mass

a = Added mass

x = Displacement

ϕ = Angular displacement

c = Damping coefficient

k = Restoring spring coefficient
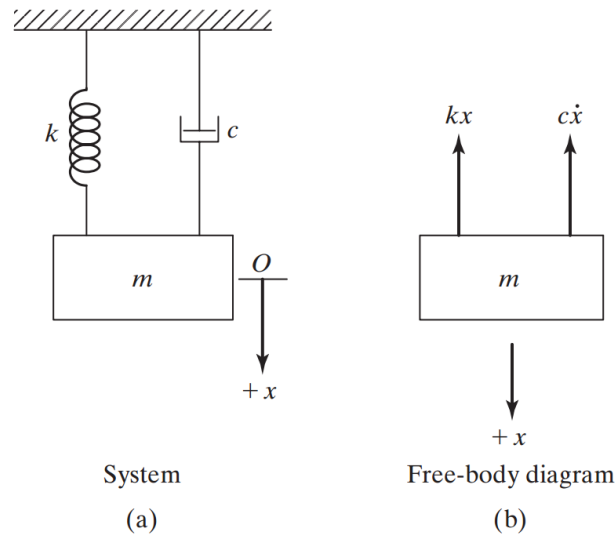
Figure 2-5: Single-degree-of-freedom system with damping (translational). [23]

A superposition of the wave loads acting on a fixed body and the oscillating motion of a body in still water results in the motion response. This assumes two conditions; The hydromechanical forces and moments induced by the oscillations of the body are undisturbed by the waves, and the wave loads are only produced by incoming waves [20]. The wave exciting forces and moments acting on the restrained body are discussed in Section 2.2.2.
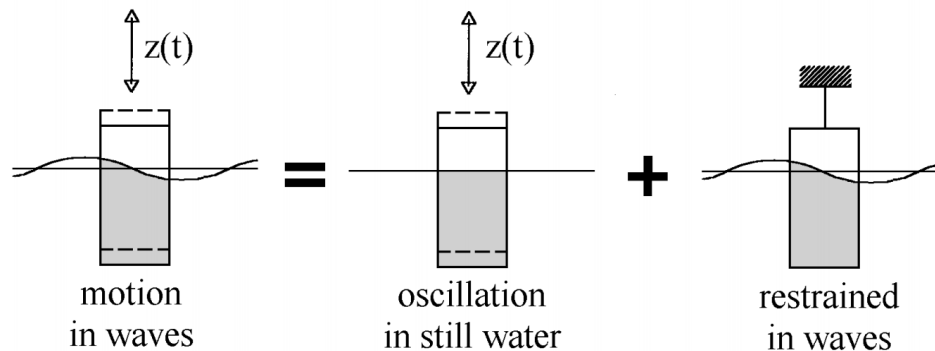
Figure 2-6: Superposition of hydromechanical and wave loads. [20]

Considering a vertical translating motion in still water. The mass and the hydromechanical loads exerted on the body determines the motions. Both the mass and the added mass needs to be accelerated, which explains term "$(m + a)\ddot{z}$" in the equation of motion (Equation (41)). "kx" is the spring restoring term, which is a proportional relation between the spring stiffness and the displacement. For a free-floating body, the spring coefficient in heave direction is Equation (43). The acceleration part and the spring restoring part of the equation of motion are neither dissipating

energy. The heaving motion will die out in the end, due to energy dissipation [20]. The frequency-dependent damping transfers energy to radiated waves moving away from the body and is therefore the component that dissipates energy. The damping coefficient (per unit length), in still water, is derived from the relation between the energy provided by the hydrodynamic damping and the energy dissipated to the radiated waves [20]. ξ_a is the amplitude of the radiated waves.

$$k_{zz} = \rho g A_{WL} \tag{43}$$

$$\frac{c}{L} = \frac{\rho g^2}{\omega^3}\left(\frac{\xi_a}{z_a}\right)^2 \tag{44}$$

Systems which require two or more coordinates to describe their motion is called multiple-degree-of-freedom systems [23]. The regular equation of motion is then replaced with a coupled equation of motion derived from Newton's second law of motion. The mass, damping and stiffness terms are expressed with matrices rather than simple terms.

$$[m]\ddot{\vec{x}} + [c]\dot{\vec{x}} + [k]\vec{x} = \vec{f} \tag{45}$$

$$\begin{bmatrix} m_{11} & m_{12} & * & m_{1n} \\ m_{21} & m_{22} & * & m_{2n} \\ * & * & * & * \\ m_{n1} & m_{n2} & * & m_{nn} \end{bmatrix}\ddot{\vec{x}} + \begin{bmatrix} c_{11} & c_{12} & * & c_{1n} \\ c_{21} & c_{22} & * & c_{2n} \\ * & * & * & * \\ c_{n1} & c_{n2} & * & c_{nn} \end{bmatrix}\dot{\vec{x}} + \begin{bmatrix} k_{11} & k_{12} & * & k_{1n} \\ k_{21} & k_{22} & * & k_{2n} \\ * & * & * & * \\ k_{n1} & k_{n2} & * & k_{nn} \end{bmatrix}\vec{x} = \vec{f} \tag{46}$$

An example of a two-degree-of-freedom system, with coupled motion, is a vessel conducting a lifting operation, at mid-ship, while rolling. This is, for simplicity, only considering the roll motion of the vessel and heaving of the load. The coupled equation of motion will then consist of 2x2-matrices and yield two natural frequencies. Similarly, a vessel deploying an ROV with a launch and recovery system will require a coupled equation of motion.

2.2.2   **Hydrodynamic Loads on Floating Structures**

The velocity potential (Equation (15)) can be split into three parts; the radiation potential, Φ_r, the undisturbed wave potential, Φ_w, and the diffraction potential, Φ_d [20].

$$\Phi = \Phi_r + \Phi_w + \Phi_d \tag{47}$$

These velocity potentials shall fulfill the same boundary conditions as in section 2.1.1, emphasizing the wall boundary condition. The velocity of the water particles at the surface of a body must be the same as the body velocity in the same point [20].

The sum of the hydromechanical loads acting on a body in water is written as Equation (48). The radiation force, F_r is equal to the force due to damping and added mass. The wave and diffraction load, F_w and F_d, can be treated

together using the diffraction theory [20]. The hydrostatic buoyancy in still water, F_s, is the stiffness times the displacement.

$$\vec{F} = \vec{F_r} + \vec{F_w} + \vec{F_d} + \vec{F_s} \tag{48}$$

Integrating the pressure over the submerged surface gives the forces and the moments. $\vec{n}$ is the outward normal vector on the surface S. $\vec{r}$ is the position vector of the surface in the steadily translating coordinate system. Using the derivation of pressure from the linearized Bernoulli equation (Equation (10)) the forces and moments can be rewritten.

$$\vec{F} = - \iint_S (p \cdot \vec{n}) \cdot dS \tag{49}$$

$$\vec{M} = - \iint_S p \cdot (\vec{r} \times \vec{n}) \cdot dS \tag{50}$$

$$\vec{F} = \rho \iint_S \left(\frac{\delta \Phi_r}{\delta t} + \frac{\delta \Phi_w}{\delta t} + \frac{\delta \Phi_d}{\delta t} + gz \right) \vec{n} \cdot dS \tag{51}$$

The radiation potential is used to determine the hydrodynamic loads. This is the forces and moments that the fluid exerts on an oscillating body in still water. The radiation potential, Φ_r, can be expressed in terms of a space dependent potential, ϕ_j, and an oscillatory velocity, v_j [20]. This applies to the potential in direction j. The normal velocity on the surface of the body, for 6 degrees of freedom, can be written as Equation (52).

$$\frac{\delta \Phi_r}{\delta n} = \sum_{j=1}^{6} \left(\frac{\delta \phi_j}{\delta n} \cdot v_j \right) \tag{52}$$

Using this relation, the radiation force can be rewritten to Equation (53).

$$\vec{F_r} = \rho \iint_S \left(\frac{\delta}{\delta t} \sum_{j=1}^{6} \phi_j v_j \right) \vec{n} \cdot dS \tag{53}$$

The forces and moments can either be caused by a motion in the same direction or they can be caused by a motion in another direction. The later one is called coupling between forces/moments and motions [20]. To account for this effect, the velocity potential in k-direction is introduced. The radiation force and radiation moment can be broken down into components. Each component is denoted as Equation (56), utilizing the fact that neither ϕ_j nor ϕ_k are time dependent [20].

$$\vec{F_r} = (X_{r1}, X_{r2}, X_{r3}) \tag{54}$$

$$\overrightarrow{M_r} = (X_{r4}, X_{r5}, X_{r6})$$ (55)

$$X_{rk_j} = \frac{\delta v_j}{dt} \rho \iint_S \phi_j \frac{\delta \phi_k}{\delta n} \cdot dS$$ (56)

The oscillatory motion can be noted using complex values, where the motion itself is given by Equation (57) [20]. As mentioned earlier, the radiation force is equal to the force due to damping and added mass. The damping is in-phase with the velocity and the added mass is in-phase with the acceleration. Combining Equation (56) and Equation (58) and solving the time derivative yields Equation (59).

$$s_j = s_{aj} e^{-i\omega t}$$ (57)

$$X_{rk_j} = -a\ddot{s}_j - b\dot{s}_j$$ (58)

$$\left(-s_{aj}\omega^2 \rho \iint_S \phi_j \frac{\delta \phi_k}{\delta n} \cdot dS \right) e^{-i\omega t} = \left(s_{aj}\omega^2 \cdot a + i s_{aj}\omega \cdot b \right) e^{-i\omega t}$$ (59)

The added mass and damping coefficients for motion in direction j are found by evaluating the sinusoidal velocity and acceleration oscillation for each their phase. The acceleration and velocity are 90 degrees out-of-phase from one another.

$$a_{kj} = -\Re \left(\rho \iint_S \phi_j \frac{\delta \phi_k}{\delta n} \cdot dS \right)$$ (60)

$$b_{kj} = -\Im \left(\rho\omega \iint_S \phi_j \frac{\delta \phi_k}{\delta n} \cdot dS \right)$$ (61)

The diffraction and undisturbed wave part of Equation (48) can be treated together. Combining Equation (51) with isolated space-dependent potentials and normalized oscillatory velocities along with the kinematic boundary condition being zero yields Equation (62).

$$X_{wk} = i\rho e^{-i\omega t} \iint_S (\phi_w + \phi_d) \frac{\delta \phi_k}{\delta n} \cdot dS$$ (62)

ϕ_k is the radiation potential in k-direction [20]. The wave potential is discussed in section 2.1.2, but the diffraction potential is unknown. Utilizing Green's second theorem for a fulfilled Laplace equation (6) (both potential functions must fulfill the equation), gives a relation between the radiation potential and the diffraction potential [20]. Using the kinematic boundary condition for a body with zero forward speed eliminates the diffraction potential.

$$\iint\limits_{S} \phi_d \frac{\delta \phi_k}{\delta n} \cdot dS = \iint\limits_{S} \phi_k \frac{\delta \phi_d}{\delta n} \cdot dS = - \iint\limits_{S} \phi_k \frac{\delta \phi_w}{\delta n} \cdot dS \tag{63}$$

Elimination of the diffraction potential from Equation (62) results in the "Haskind relations". Some potential flow theory software have the option to use this relation instead of force/moment equation including diffraction potential. This can only be used for bodies with a time-averaged speed of zero in all directions.

2.3 Time Domain Approach

The frequency domain approach studies linear systems with behavior related to displacement, velocity and acceleration. For many cases, this cannot be considered a valid approach. Second order wave load, nonlinear viscous damping, forces and moments due to currents and wind all violate the linear assumption [20]. This means that the superposition principle no longer works. To accommodate for the invalid linear assumption, the equations of motion can be solved directly as a function of time [20]. This approach is called the time domain approach.

The equation of motions for the time domain approach can be derived by studying a body experiencing an impulsive displacement, with constant velocity, during a short time interval [20]. When this body moves, the water particles around it will also move. In light of potential theory, the velocity potential can be written as a relation between a normalized velocity potential and the body velocity [20]. The same relation can be written for the body's displacement. Combining these two relations and letting the time step approach zero yields the resulting velocity potential.

$$\Phi(t) = \dot{x}(t) \cdot \Psi + \int_{-\infty}^{t} \chi(t - \tau) \cdot \dot{x}(\tau) \cdot d\tau \tag{64}$$

This expression includes a normalized velocity potential, Ψ, proportional to the velocity of the body and a normalized velocity potential, χ, proportional to the displacement. The displacement of the body also influences the fluid motions subsequent to the body motion [20]. This allows the equation to carry a form for memory of previous motions. Using Equation (64) and the linearized Bernoulli equation, the equation of motion for time domain approach, the added mass coefficient and the damping coefficient can be derived. $X(t)$ is the external load applied to the system and C is the spring coefficient [20].

$$A = \rho \iint\limits_{S} \Psi \cdot n \cdot dS \tag{65}$$

$$B(t) = \rho \iint\limits_{S} \frac{\delta \chi(t - \tau)}{\delta t} \cdot n \cdot dS \tag{66}$$

$$(M + A) \cdot \ddot{x}(t) + \int\limits_0^\infty B(\tau) \cdot \dot{x}(t - \tau) \cdot d\tau + C \cdot x(t) = X(t) \tag{67}$$

This equation of motion (67) is often referred to as the "Cummins Equation" in honor of W.E Cummins' work on the subject [20].

The spring coefficient, C, can be determined from geometry and center of gravity. Frequency-dependent added mass and damping are obtained from potential theory [24]. The frequency-dependent coefficients can be used to describe the coefficients needed in the "Cummins Equation". This function is called the retardation function. Since the retardation function is calculated using frequency-related damping, the radiation force will be formulated as a convolution integral [24].

$$B(\tau) = \frac{2}{\pi} \cdot \int\limits_0^\infty b(\omega) \cdot cos(\omega\tau) \cdot d\omega \tag{68}$$

$$A = a(\omega) + \frac{1}{\pi} \cdot \int\limits_0^\infty B(\tau) \cdot sin(\omega\tau) \cdot d\tau \tag{69}$$

2.4 Wave Forces on Slender Elements

This theory is based on small cylinders relative to the wave length. The requirement is normally that the wave length is 5 times the diameter of the cylinder [20]. It is assumed that the water motions are same all over the diameter of the cylinder. This assumption is the reason for the diameter to wave length ratio requirement. The Morrison equation (70) is used to estimate the drag and inertia loads per unit length on a slender structure exposed to waves and/or current. By integrating over the length of the structure the total hydrodynamic load can be found.

$$f(t) = \rho V(1 + C_A)\dot{v} + \frac{1}{2}\rho C_D A v|v| \tag{70}$$

The first term of the equation, which is the sum of the mass of the displaced volume and the added mass times the fluid acceleration, covers the inertia forces. The second term, which is half the product of the mass density of the fluid and the projected object area times the fluid velocity squared, becomes the drag term when including the drag coefficient. The inertia force is in line with the acceleration of the water particles and the drag force is in line with the water particle velocity. The drag term includes the product of the velocity and the absolute value of the velocity, rather than velocity squared. This is to ensure correct sign/direction. The inertia force and the drag force are not acting at the same time. When the force is plotted as a function of time it can be seen that the two forces are 90 degrees out of phase with each other. This is because of the phase shift between the acceleration and the velocity for an oscillating motion [20].

For a slender cylinder, with an axis which is not perpendicular or parallel with the velocity component, there will be three force components acting on the cylinder: The normal force, f_N, the axial force, f_T and the lift force, f_L.
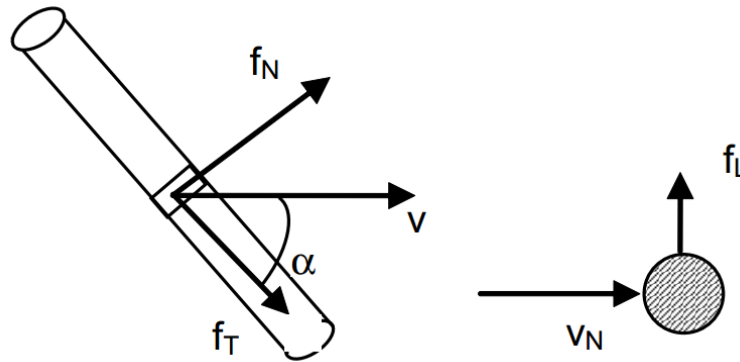
Figure 2-7: Hydrodynamic forces acting on inclined cylinder [1].

Figure 2-7 illustrates the three force components. The normal force and the axial force can be found by decomposing the Morrison equation. The axial force is mainly due to skin friction and the Morrison equation is therefore reduced to the drag term [25]. The lift force can be found from Equation (72).

$$f_T = \frac{1}{2}\rho C_{Dt} D v^2 \tag{71}$$

$$f_L = \frac{1}{2}\rho C_L D v^2 \tag{72}$$

ρ = Fluid density

C_L = Lift coefficient

D = Diameter

v = Fluid velocity

The Morrison equation above is applicable for a still slender structure in flow and/or waves. The forces on moving structures in still waters can be described with Equation (73).

$$f(t) = -\rho C_A A \ddot{r} - \frac{1}{2}\rho C_D D \dot{r} \tag{73}$$

C_A = Added mass coefficient

D = Diameter

v = Fluid velocity

The sectional force acting on a moving structure in waves and current can be found by summing the forces from a moving structure in still water and a still structure in waves and current. This gives Equation (74).

$$f(t) = -\rho C_A A \ddot{r} + \rho V (1 + C_A)\dot{v} + \frac{1}{2}\rho C_D A v|v| - \frac{1}{2}\rho C_D D \dot{r} \qquad (74)$$

According to DNV's recommended practice for environmental loads and environmental conditions [25] the variation of the added mass coefficient and the drag coefficient as a function of the Reynolds number, the Keulegan-Carpenter number and the roughness should be accounted for. For 2- and 3-dimensional bodies with a simple geometry the added mass coefficient and drag coefficient can be found in the appendices in DNV's recommended practice for modelling and analysis of marine operations [1].

2.4.1 Added Mass Coefficient

When accelerating an object in fluid a force arises due to the acceleration of nearby fluid particles. This force can be written as Equation (75), where $\ddot{r}$ is the acceleration of the object and m_a is a coefficient called hydrodynamic mass or added mass (it has the same unit as mass [kg]) [20].
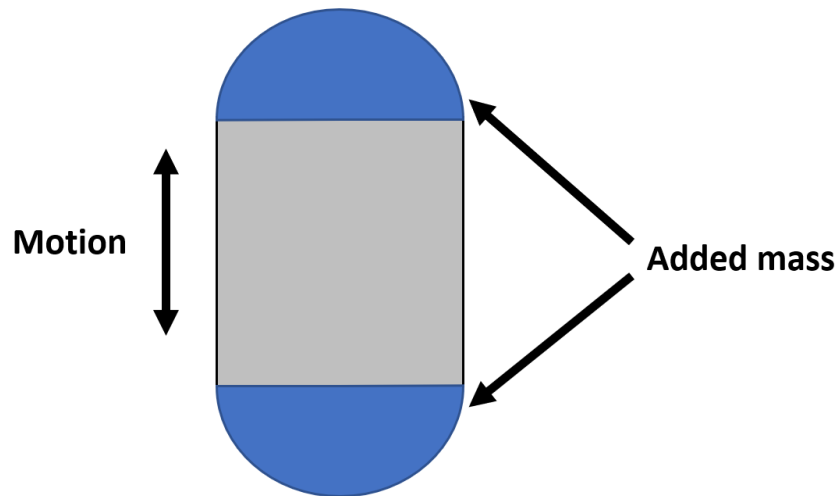
Figure 2-8: Grey rectangular box oscillating in fluid.

$$f = m_a \ddot{r} \qquad (75)$$

The added mass coefficient can be calculated from the ratio between the added mass per unit length and the cross-section area of the object.

$$C_A = \frac{m_a}{\rho A} \tag{76}$$

For small Keulegan Carpenter numbers, $K_C < 3$, the added mass coefficient can be assumed to be independent of the K_C-number. For larger K_C-values the added mass coefficient, for cylindrical elements, can be found by using the K_C-number and the steady flow drag coefficient, C_{DS}.

$$C_A = max \begin{Bmatrix} 1.0 - 0.044(k_C - 3) \\ 0.6 - (C_{DS} - 0.65) \end{Bmatrix} \tag{77}$$

2.4.2   Drag Coefficient

The drag coefficient depends on the Reynolds number for circular cylinders. For a certain range of Reynolds numbers, the drag coefficient drops significantly. This range is referred to as the critical flow regime. Figure 2-9 shows how the drag coefficient, C, changes when the Reynolds number changes for various degrees of surface roughness. This is all within the critical flow regime.
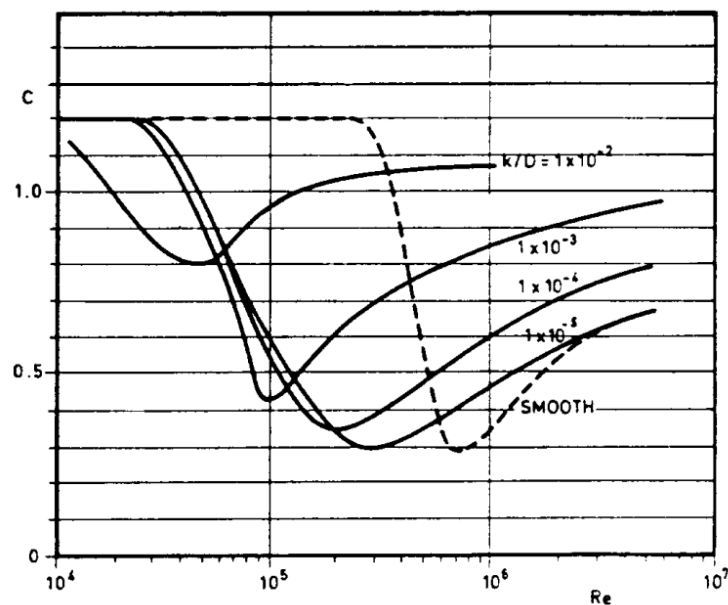
Figure 2-9: Drag coefficient for fixed circular cylinder for steady flow in critical flow regime, for various roughnesses [25].

The drag coefficient variation for cylinders in the supercritical flow regime can be approximated by Equation (78). This is the product of the steady flow drag coefficient and the wake amplification factor. The wake amplification factor is a function of the K_C-number.

$$C_D = C_{DS}(\Delta) \cdot \psi(K_C) \tag{78}$$

The dependence of the drag coefficient on surface roughness can be expressed as Equation (79) when the Reynolds number is high ($R_e > 10^6$) and the K_C-number is large. Delta is the ratio between the roughness and the diameter of the cylinder.

$$C_{DS}(\Delta) = \begin{cases} 0,65 & ; \Delta < 10^{-4} \ (smooth) \\ \dfrac{(29 + 4 \cdot \log_{10}(\Delta))}{20} & ; 10^{-4} < \Delta < 10^{-2} \\ 1,05 & ; \Delta > 10^{-2} \ (rough) \end{cases} \tag{79}$$

The wake amplification factor can be found from Figure 2-10. This figure only applies to free flow fields with no proximity to fixed boundaries.
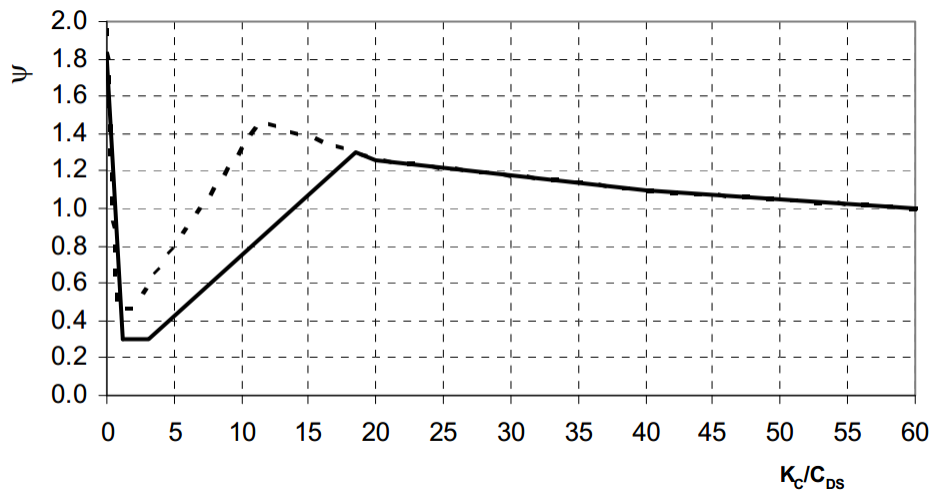
Figure 2-10: Wake amplification factor, ψ, as a function of K_C-number for smooth ($C_{DS} = 0.65$ - solid line) and rough ($C_{DS} = 1.05$ - dotted line) [25].

2.4.3 Slamming

Slamming force acting on an object being lowered through the splash zone is caused by transfer of momentum from the water particles in the vicinity of the object to the object itself. The expression for the slamming force can be found by taking the derivative of the added mass momentum [25].

$$f_s = \frac{d}{dt}(m_a V) = m_a \dot{V} + \frac{dm_a}{dh} V^2 \tag{80}$$

For a constant velocity the first term of the slamming force can be removed. The added mass, which is not constant, can be taken as the high frequency limit of added mass. This assumes that local water particle acceleration due to

water entry of the object is much larger than the acceleration of gravity. This is equivalent to a body oscillating with a high frequency in still water [1]. The slamming force can also be expressed using a slamming coefficient.

$$f_s = \frac{1}{2}\rho C_s A_p V^2$$
(81)

A_p is the projected area of the object and ρ is the fluid density. The slamming coefficient, C_s, can be expressed as Equation (82).

$$C_s = \frac{2}{\rho A_p}\frac{dm_a}{dh}$$
(82)

2.5   Probability Model

A precise prediction of an event containing high randomness, such as marine operations in waves, is impossible. Probability models can be used to obtain proper estimates for exceedance probabilities. Selecting the proper probabilistic model is crucial if the goal is to determine exceedance probabilities for the upper and lower region of a distribution. Several probability models can appear to be valid for the central part of the distribution (around the mean value), but the tail region can have a significant difference in behavior [21]. The tail region (upper and lower region) is often the region of interest when determining characteristic values to be used in marine engineering. These characteristic values can be used to determine operational limitations such as significant wave height and peak period.

A sufficient amount of data is needed to model the distribution of an event. This can either be historical data, to e.g. determine the annual exceedance probability of a certain wave height, or it can be numerical simulations. A set of numerical simulations can be executed to obtain enough data to determine the parameters for the chosen distribution using the method of moments [21].

2.5.1   Extreme Value Theory

As opposed to the central limit theory, which describes the distribution of a sample mean with the normal distribution when the number of cases approaches unlimited, the extreme value theory describes the extreme events. This theory models the tails of the distribution functions using a semi-parametric model [26]. Four common extreme value distributions are presented below, where the last one is a combination of the three first ones.

The Gumbel Distribution

The Gumbel Distribution is commonly used in marine engineering for determining maximum and minimum responses for a system [14]. The use of this distribution is particularly common for environmental data [27]. The cumulative

distribution function is presented below. X is the variable of interest, the scale parameter and the location parameter is denoted by κ and λ, respectively.

$$F_x(x) = e^{-e^{-\left(\frac{x-\lambda}{\kappa}\right)}} \tag{83}$$

There is a difference between the Gumbel minimum distribution and the Gumbel maximum distribution. For determining fractiles in the minimum end of the sample the minimum distribution must be used [28]. Likewise, when determining the fractiles in the maximum end of the sample the maximum Gumbel distribution shall be used. Equation (83) is the Gumbel maximum distribution. When using the methods of moment (ref. section 0) to determine the parameters for the distribution, the equation for the location parameter is slightly changed.

The Fréchet distribution

The Fréchet distribution is, similar to the Gumbel distribution, used to model extreme values for a set of data [14]. The parameters are the same as for the Gumbel distribution, but also including the shape parameter, β. This is a three-parameter distribution and the Gumbel distribution is a two-parameter distribution. The cumulative distribution function is given by Equation (84).

$$F_x(x) = e^{-\left(\frac{x-\lambda}{\kappa}\right)^{-\beta}} \tag{84}$$

The Weibull distribution

The Weibull distribution is a two-parameter distribution just like the Gumbel distribution. This distribution bases on the scale parameter, κ, and the shape parameter, β. Weibull extreme value distribution is commonly used for modeling failures rates for products in order to evaluate their reliability [14].

$$F_x(x) = 1 - e^{-\left(\frac{x}{\kappa}\right)^{\beta}} \tag{85}$$

The generalized extreme value distribution

The three extreme value distributions above have been combined to a generalized extreme value distribution (GEVD) which is equal to the Gumbel distribution when the shape parameter is equal to zero. The GEVD is equal to the Weibull distribution when the shape parameter is negative, and equal to the Fréchet distribution when the shape parameter is positive [14]. This distribution is, like the others, used to model extreme values [27].

$$F_x(x) = e^{-\left(1+\beta\left(\frac{x-\lambda}{\kappa}\right)\right)^{-\frac{1}{\beta}}} \tag{86}$$

2.5.2 **Statistical Inference**

Statistical inference is done in three steps. First a probabilistic model is selected, then the selected model is fitted to the available data by estimating the parameters based on the data. Lastly, the fitted model must be validated against the data to see if it is acceptable. The parameters for the distributions mentioned in section 2.5.1 can be estimated by using the method of moments [21]. The parameters are found by calculating the mean, the variance and the skewness coefficient for the sample data and setting them equal to the same moments of the selected distribution. The three moments of a three-parameter distribution are given in Equation (87) to (89). Equation (90) to (92) represents the mean, variance, and skewness of a sample of data.

$$\mu = E[X] = \int_{-\infty}^{\infty} x f_x(x) dx \tag{87}$$

$$\sigma_x^2 = Var[x] = \int_{-\infty}^{\infty} (x - \mu_x)^2 f_x(x) dx \tag{88}$$

$$\gamma = \frac{E[(X - \mu_X)^3]}{\sigma_x^3} \tag{89}$$

$$\bar{x} = \frac{1}{n} \sum_{i=1}^{n} x_i \tag{90}$$

$$S_x^2 = \frac{1}{n-1} \sum_{i=1}^{n} (x_i - \bar{x})^2 \tag{91}$$

$$g = \frac{\frac{1}{n}\sum_{i=1}^{n}(x_i - \bar{x})^3}{\left[\frac{1}{n-1}\sum_{i=1}^{n}(x_i - \bar{x})^2\right]^{\frac{3}{2}}} \tag{92}$$

Chapter 3

Numerical Models for Hydrodynamic Analysis

3.1   Assumptions and Simplifications

Some assumptions and simplifications are made when defining the numerical model for the hydrodynamic analysis. The software itself assumes that the water can be treated as an ideal and incompressible fluid with no shear forces between the particles. This is further explained in the potential flow theory part of the theory chapter (section 2.1.1). Extra damping needs to be added as input in the roll direction because of the assumption that the water is inviscid.

As a simplification, the second order wave loads are not calculated. This is because the drift loads are not of interest. It is assumed that the vessels dynamic positioning system will counteract the vessels drifting due to waves. The RAO data is obtained by running single wave periods towards the vessel, one at a time [29]. The values in between the analyzed wave periods are determined using interpolation. It is assumed that period steps of 0,25 seconds are small enough increments to realistically reflect the vessels responses in any wave with a period between 2 seconds and 20 seconds.

The natural periods for the vessel are hand calculated using the added mass at infinite frequency to compare with the results for the diffraction analysis. It is assumed that the added mass obtained from the diffraction analysis at the lowest wave period (2 seconds) is close enough to the added mass that would have been obtained at 0 seconds wave period. The lowest analyzed wave period is set to 2 seconds because, according to the Orcawave help documentation [29], a certain amount of mesh panels per wave length is required to obtain realistic results.

3.2   Numerical Tools

Orcawave uses potential flow theory to calculate response and loadings for wet bodies. The basis for the calculations is environmental conditions, inertia properties and constraints from external stiffness or external damping and body shapes. Orcawave needs a separate software to create mesh. This can be done using various software listed in the Orcawave documentation [29]. Gmsh is chosen as the preferred software for this study simply because it is an open source three-dimensional finite element grid generator [30].

3.3   ROV Deployment Vessel

3.3.1   Vessel Dimension and Meshing

The properties of the analyzed vessel are given in Table 3-1. The surface model of the vessel and the damping lid was exported from the CAD-software Inventor [31], and directly imported to Gmsh. An alternative method is to create the nodes and the surfaces in Gmsh. Several meshing algorithms can be used to generate the finite element grid in Gmsh. Since the vessel contains multiple curved surfaces and sharp edges, the "MeshAdapt"-algorithm was chosen (Figure 3-1). The "MeshAdapt" algorithm is, according to the Gmsh documentation [32], a technique based on local mesh modifications, making it the most robust technique for complex curved surfaces. Keeping the XY-plane at the free surface already in Gmsh simplifies the transition into Orcawave.

Table 3-1: ROV deployment vessel properties.

	Value
Length, $[m]$	15
Beam, $[m]$	3,8
Draught, $[m]$	1,4
Distance from keel to COG, $[m]$	1,8
Radii of gyration, X-axis, $[m]$	1,153
Radii of gyration, Y-axis, $[m]$	3,307
Radii of gyration, Z-axis, $[m]$	3,512
Mass, $[t]$	41

Orcawave has the option to import both triangular and quadrilateral meshes. Importing non-planar panels, however, forces Orcawave to project the non-planar panels onto a common plane [29]. Due to triangular mesh always being

planar, and therefore yielding more control over the geometry, it is chosen to be the preferred mesh style for this analysis.
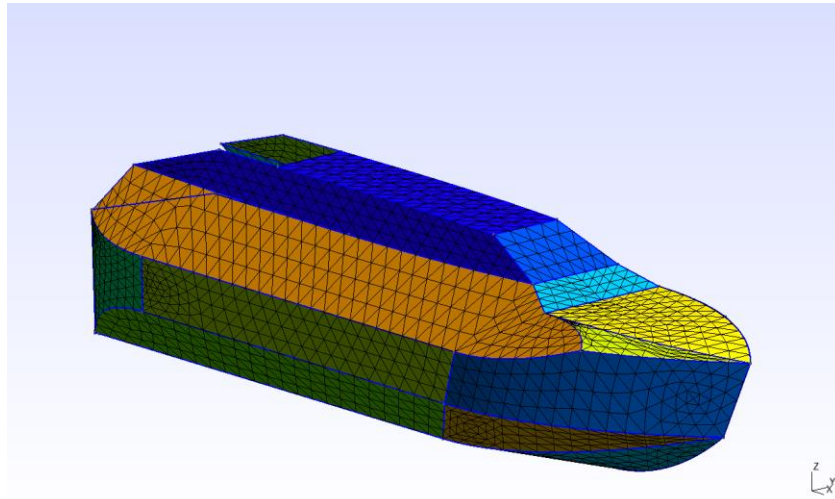
Figure 3-1: Triangular mesh panels produced in Gmsh.

When importing a body to Orcawave the position of the body and the orientation of the body can be altered. This gives an opportunity to run analyses for different loading conditions without regenerating the mesh. In this study the trim angle of the vessel was modified according to the static analysis results, from Orcaflex, with the ROV hanging over the stern. This is considered an approximation, as the center of floatation is changing with the trimming angle. For this case, the center of floatation is located slightly in front of the mesh origin and moves slightly further aft when trimming is induced. The effect of the distance between the mesh origin and the center of floatation is considered negligible. Symmetry can be applied when importing a body into Orcawave. This reduces the number of mesh panels and hence reduces the analysis runtime.

Orcawave imports both the panels above the waterline (dry body panels) and the panels below the waterline (wet body panels). The potential formulation equations only consider the wet body panels and the interior lid panels (internal panels in the horizontal plane embraced by the waterline) [29]. Dry body panels are useful if the initial mesh orientation is altered (Figure 3-5), or the body is chosen to be in a non-equilibrium position. This vessel is assumed to be in equilibrium position, and the behavior is therefore dictated by the radii of gyration and the vertical center of gravity position.
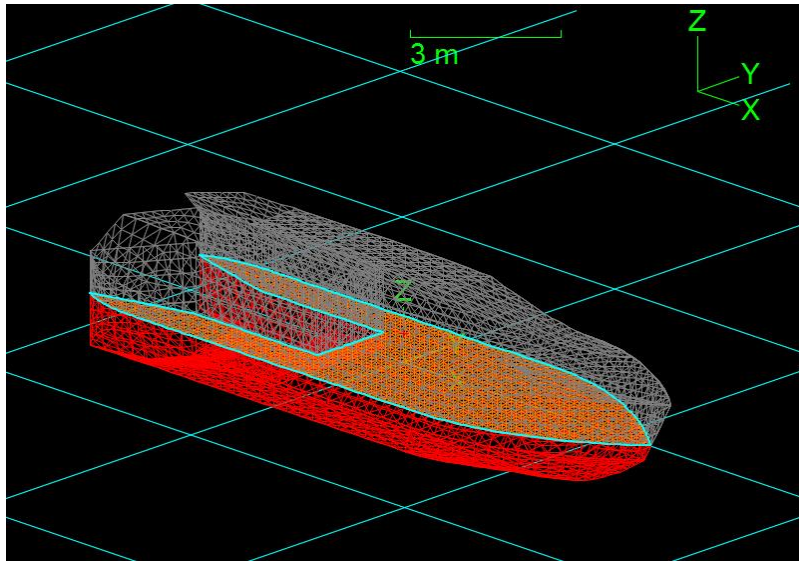
Figure 3-2: Orcawave mesh view.

It is important to maintain a low aspect ratio, which is a metric for how long and slender a panel is, when creating the mesh. Orcawave reports the aspect ratio, which is defined as the square of the longest side divided by the panel area. Special consideration should be given to panel slenderness near the waterline [29].

3.3.2   Modelling of Viscous Damping

Since the potential flow theory assumes that the fluid has no viscosity, there is no damping effect to reduce any fluid resonance effects. This resonance can lead to unrealistic response spikes in the diffraction results [29]. These effects are likely to happen in confined spaces such a narrow gap between two vessels or in a moonpool. For this model the effect is likely to occur in the open stern area. To accommodate for such resonance effects a damping lid can be added. This is a separate mesh covering the free surface of where damping will be applied. Orcawave requires a damping lid factor, ϵ, to be specified. This factor does not correspond to a tabulated physical property of water [29]. The value should be based on experimental or measured data. For this study a damping lid around the entire model and a damping coefficient of 0.2 was applied. This particular factor was based on neither experimental nor measured data. Further investigation is needed to determine if this is an accurate assumption or not. To investigate the effect of the damping lid, Orcwave offers the possibility to add field points to the model, which returns sea state RAO at the location of the points [29]. The damping lid mesh is also generated in Gmsh, via a STEP file from Inventor. The damping lid mesh is a flat surface model, located at the free surface with its normal vector pointing downwards.
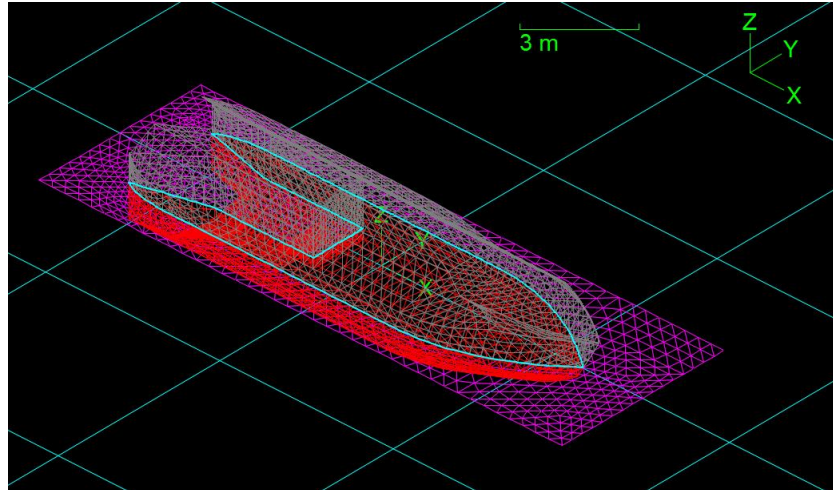
Figure 3-3: Body mesh including damping lid.
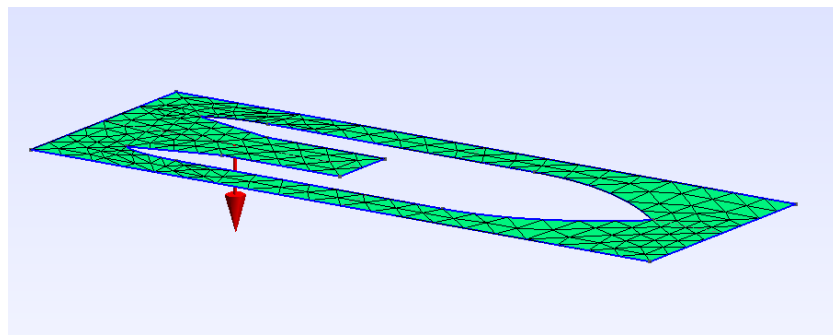
Figure 3-4: Damping lid mesh generated in Gmsh.

Another effect which is not covered when using potential flow theory is the damping which suppresses a body motion resonance, e.g. roll resonance of a ship or heave resonance of a slender spar buoy [29]. The viscous roll damping for this vessel has been determined using Froude scaling on Orcina's example vessel [29]. Since the two vessels don't scale uniformly in all dimensions, the Froude scaling can introduce errors. It is therefore recommended that the viscous roll damping of this particular vessel is further studied using appropriate software. Froude scaling scales each value with a factor that depends on the unit of the value. If R is the scaling factor between two vessel lengths, then the unit dependent factors are given below [29].

Length: R

Mass: R^3

Time: $R^{\frac{1}{2}}$

Since rotational damping has the unit $\frac{kg \cdot m^2}{s}$, or $\frac{mass \cdot length^2}{time}$, the scaling factor becomes $R^{4.5}$. Comparing the width of the Orcina example vessel with the width of the studied vessel gives a roll damping of $56\frac{kNm}{rad/s}$. Refer to Appendix A for calculations.
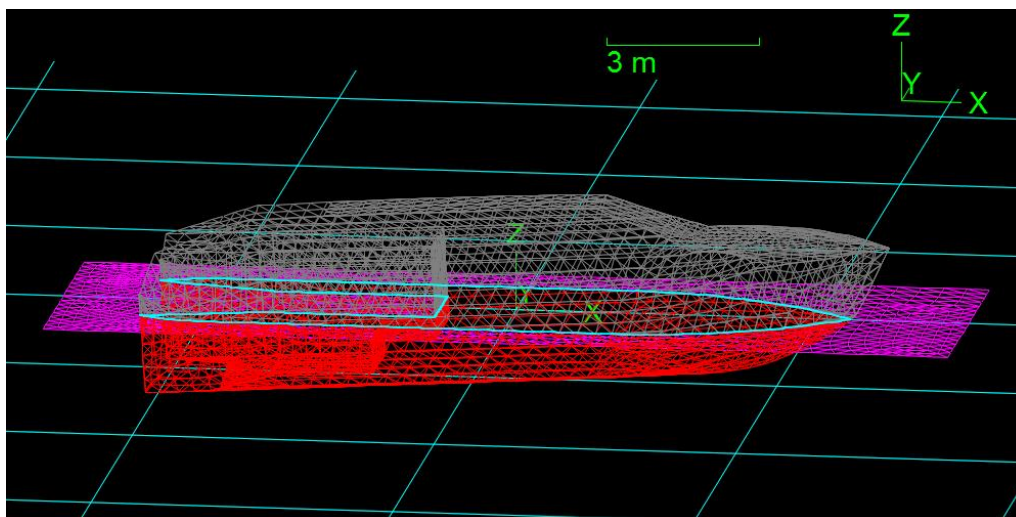
Figure 3-5: Body mesh with 3,66 degrees trim.

3.3.3 Vessel Trimming and Simulation Setup

A separate analysis covering the situation where the ROV is hanging at the stern of the vessel has been conducted. The trimming angle is calculated in Orcaflex using the static simulation function. The result is that the vessel will have a trimming angle of 3,66 degrees while in equilibrium state.

Environmental conditions lay the foundation for the potential theory calculations, where Orcawave uses the classical Green's function [29]. Green's function for finite- or infinite-depth water, which are both defined as the complex potential of the response to a point source in the absence of a body and the absence of damping lid, is triggered by the water depth input. Orcawave will use Green's function for infinite-depth water when specifying infinite water depth. Waves are referred to by the period and the vessel heading relative to the wave direction. An increasing number of wave headings and wave periods will increase the solving time. Periods from 2 seconds to 20 seconds, with 0.25 second increments are considered sufficient for these analyses. Wave headings from 0 degrees to 180 degrees with 45 degrees increments are specified. This covers the most interesting directions. If RAOs for non-analyzed wave headings are required, Orcaflex will interpolate the results.

3.4 ITS Deployment Vessel

The hydrodynamic analysis of the ITS deployment vessel has been conducted using similar method as described in the previous subchapter. Less details are therefore included in this chapter. Two cases have been analysed. The first case analyses the vessel responses in upright position, while the second case analyses the vessel responses when heeling 3 degrees towards port side.

The mesh of the vessel hull is, as for the ROV deployment vessel, created in Gmsh. Since this is a relatively large vessel, using the symmetry feature is key to keep the analysis running time as low as possible. Since the predefined recommendation for numbers of element per wavelength is set to 5 a large number of elements is needed to cover the entire vessel. Using linear wave theory and assuming that the waves are deep-water waves gives Equation (93). For the minimum wave period of 2 seconds this means 5 elements per 6,25 meters. For an overall length of approximately 150 meters this will result in many elements. The element size can be controlled by setting a minimum and maximum element size in the Gmsh meshing options.

$$L = \frac{gT^2}{2\pi} \tag{93}$$

Table 3-2: ITS deployment vessel properties.

	Value
Length, $[m]$	15
Beam, $[m]$	27
Draught, $[m]$	6,56
Distance from keel to COG, $[m]$	10,35
Radii of gyration, X-axis, $[m]$	10,53
Radii of gyration, Y-axis, $[m]$	40,81
Radii of gyration, Z-axis, $[m]$	40,81
Mass, $[t]$	18220
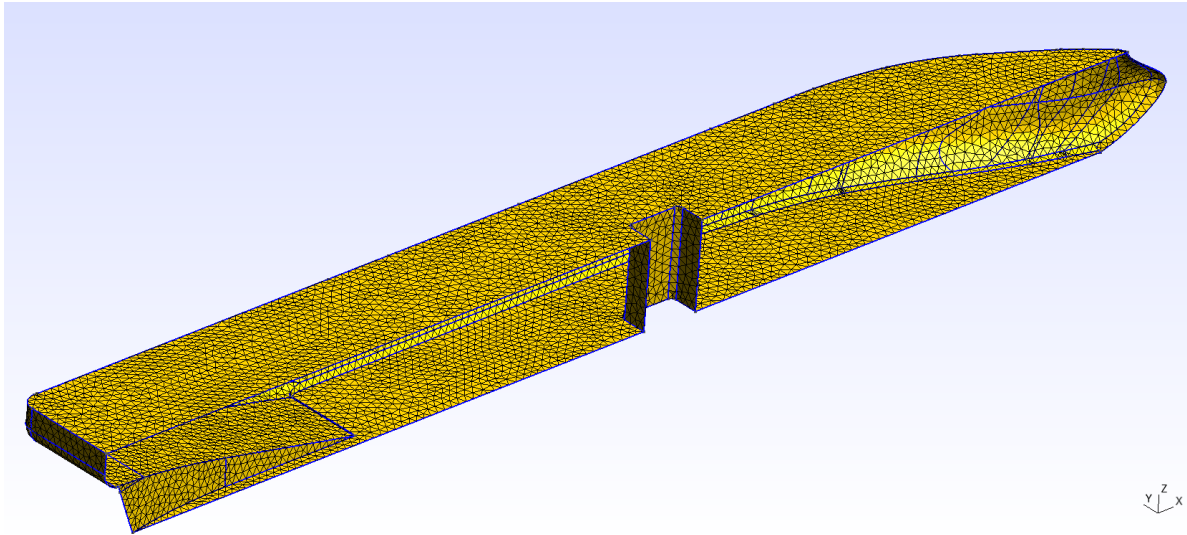
Figure 3-6: ITS deployment vessel - Symmetry mesh in Gmsh.

The faces on the symmetry plane are removed prior to importing the mesh to Orcawave, as shown in Figure 3-6. The other half of the vessel hull is activated in Orcawave, and a damping lid is added in the moonpool to soften the water resonance. The damping coefficient is taken to be 0,04. This value is only determined by running sensitivity studies and comparing the shape of the RAO graphs. The goal is to reduce the spike, as seen in Figure 3-8, without affecting the other RAO results significantly. As mentioned in Section 3.3.2 the value should be properly estimated through experimental or measured data.

The effect of the damping lid can be seen in the RAO results. The spike occurring at around 6 seconds almost vanishes when adding the damping lid. This spike can be seen for several of the responses in all the analyzed wave directions. Figure 3-8 presents the change in heave response for beam waves after the water resonance in the moonpool is damped.
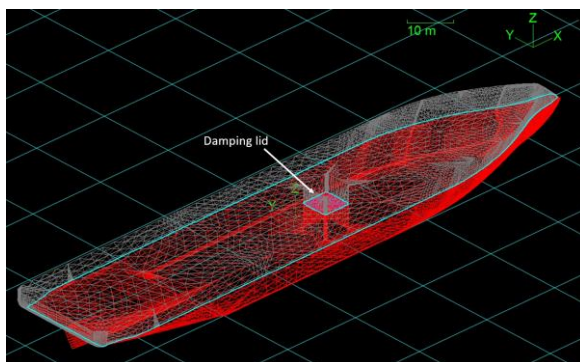
Figure 3-7: ITS deployment vessel - Orcawave model with damping lid.
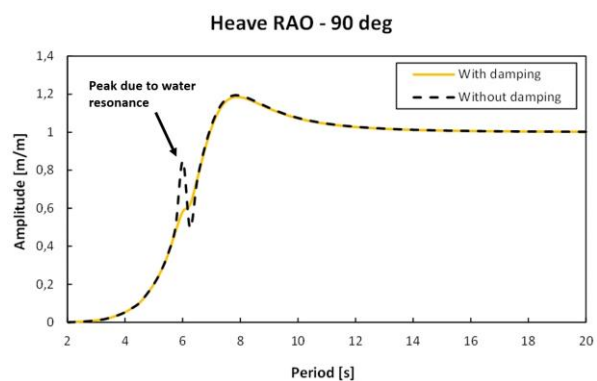
Figure 3-8: The effect of damping lid in the ITS deployment vessel moonpool.

External damping is applied in roll direction due to the inviscid fluid assumption. $4 \times 10^5 \frac{kNm}{rad/s}$ is used as input for the viscous roll damping. This is purely a product of Froude scaling the Orcawave example vessel with regards to the vessel beam. Refer to Appendix A for calculations.

A grid of field points is specified for the analysis to simulate the effect of shielding. The water particles in lee of a large vessel will have a reduced velocity potential compared to the undisturbed waves. Orcawave produces sea state RAOs at the locations of the field points. The sea state RAOs are calculated at the still water level and 3,9 meters below the surface. This is the position where the volume center of the trapped water in the suction can is located when the roof of the suction anchor reaches the sea surface. Ref. Section 5.3.3. The field points are indicated with purple dots in Figure 3-9. The wave component properties are calculated from the spatial gradients of the disturbance RAO. These gradients can either be calculated in Orcaflex or predefined along with the RAOs. It is recommended to calculate the sea state RAO gradients using a diffraction analysis software rather than having Orcaflex estimate the values [22]. This requires more computer power and can be included in the analysis by choosing to solve both potential and source formulation. This study calculates the RAO gradients using Orcawave.
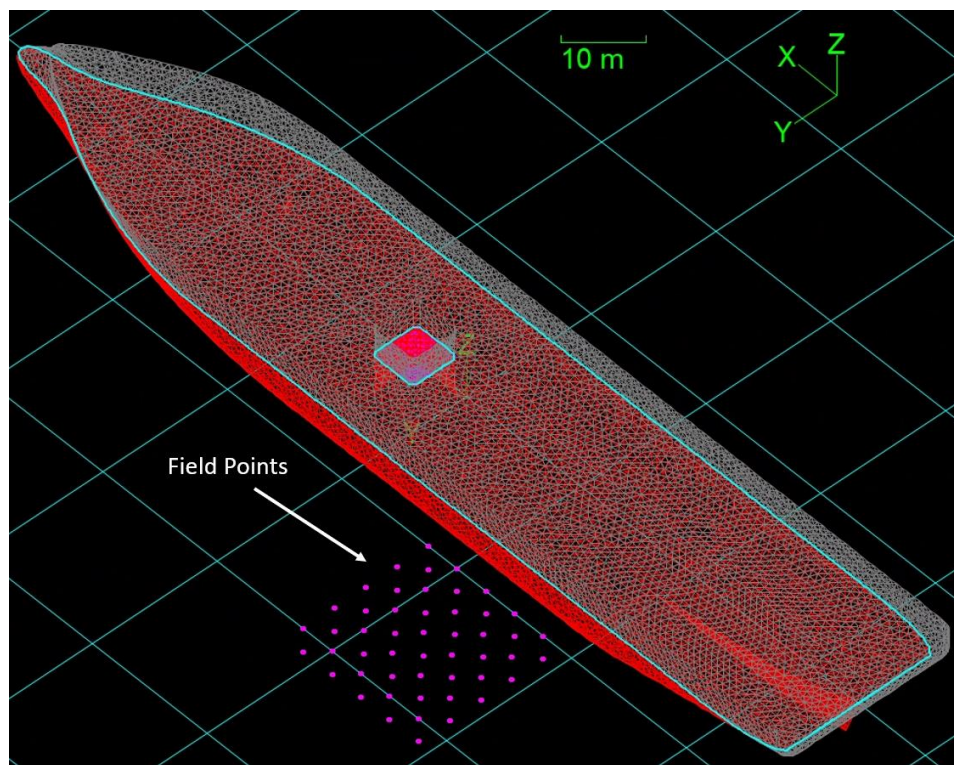
Figure 3-9: ITS deployment vessel - Field points for calculation of sea state RAOs.

Chapter 4

Hydrodynamic Analysis Results

4.1 ROV Deployment Vessel

Four different hydrodynamic analyses were conducted, ref Table 4-1. The last two, Analysis 3 & 4, were later imported to Orcaflex and used as a basis for time domain simulations. The four analyses are compared to highlight the effect of different diffraction analysis settings, and to recreate real-life vessel responses as accurately as possible. The peaks in the RAO-graphs are compared to the calculated natural periods. The natural periods for heave, roll and pitch are calculated for each analysis. Refer to Appendix B for calculations. The same motions are also considered the motions of interest and are therefore the main focus in this chapter. Several different wave headings could be investigated. This thesis focuses on the beam waves (90 degrees) and the head waves (180 degrees) to narrow down the result section.

Table 4-1: Hydrodynamic analysis matrix.

	Damping lid coefficient, $[-]$	Viscous roll damping, $\left[\frac{kNm}{\frac{rad}{s}}\right]$	Trim, $[°]$
Analysis 1	None	0	0
Analysis 2	0,2	0	0
Analysis 3	0,2	56	0
Analysis 4	0,2	56	3,66

4.1.1   **Analysis 1**

As per Table 4-1 the first analysis did not contain any external constraints, damping lids or inclinations. This was only considering the vessel itself under the given environmental conditions. The results are characterized by peaks occuring at similar periods.

Table 4-2: Natural periods – Analysis 1.

	Value
Heave[2], $[s]$	4,7
Heave[3], $[s]$	3,0
Roll[3], $[s]$	6,6
Pitch[3], $[s]$	3,0
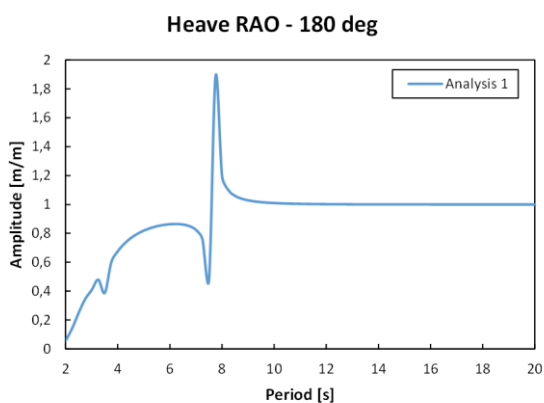
Figure 4-1: Heave RAO for head waves - Analysis 1.
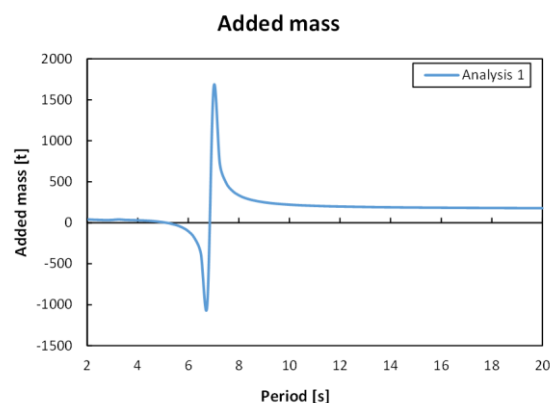
Figure 4-2: Heave added mass - Analysis 1.

The first peak of the graph, located at around 3 seconds, corresponds well with the calculated pure heave natural period of 3 seconds. The second peak could indicate that something is wrong, as it dips before it goes way above the other values. This occurs almost at the same period as the added mass peaks below zero, before jumping back up to a positive peak (Figure 4-2). This gives reason to run an analysis with damping lid (Analysis 2), and check whether it will impact the results.

It can be seen that both pitch RAO (Figure 4-3) and surge RAO (Figure 4-4) have the same spike as the heave RAO does. The pitch RAO has two peaks, where the first one could be explained as the natural period for pitch motions.

---

[2] Calculated using Added mass from DNV-RP-H103, Table A-1

[3] Calculated using Added mass from Orcawave

The calculated natural pitch period is 3 seconds according to Table 4-2. The peak in the RAO graph happens around 3.5 seconds, which gives reason to believe that this is the natural period. The discrepancies in the value could be due to coupling effects.
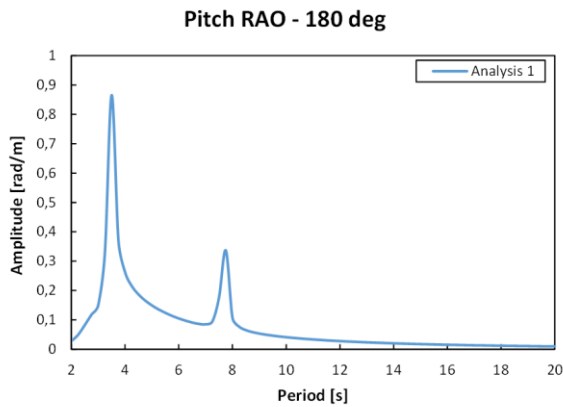
Figure 4-3: Pitch RAO for head waves - Analysis 1.
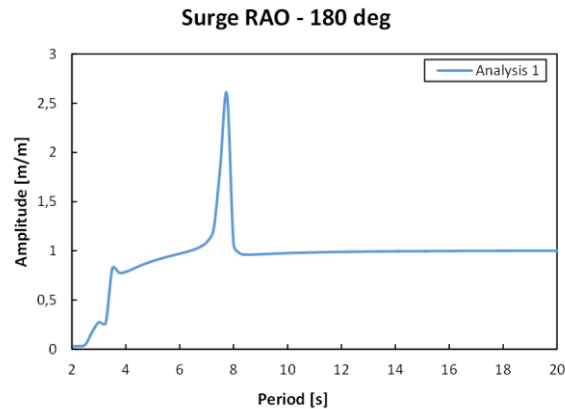
Figure 4-4: Surge RAO for head waves - Analysis 1.

The same natural period peak, as seen in Figure 4-1, can be seen in the heave RAO for beam waves. Some evidence of the same 7,5 second spike can be spotted in Figure 4-5, but with a much lower magnitude. The roll RAO in beam waves indicates a peak of great magnitude around 6 seconds, which corresponds with the calculated natural period of 6,6 seconds. The magnitude of this peak is most likely due the assumption of a non-viscous fluid. A rotation of slightly above 2 radians per meter wave amplitude suggests that the vessel will turn an entire turn in waves with 3 meters amplitude. This gives a reason the run an analysis with added viscous roll damping and compare the results. The roll damping is presented in Figure 4-7.
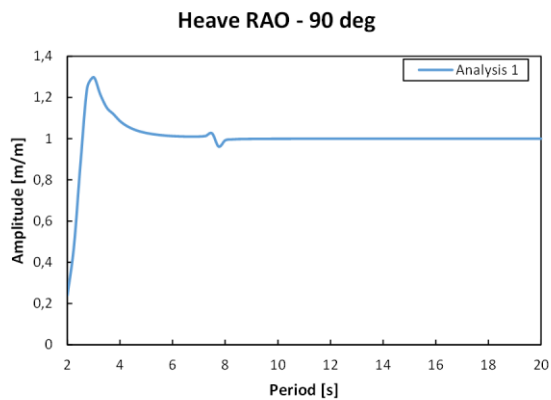
Figure 4-5: Heave RAO for beam waves – Analysis 1.
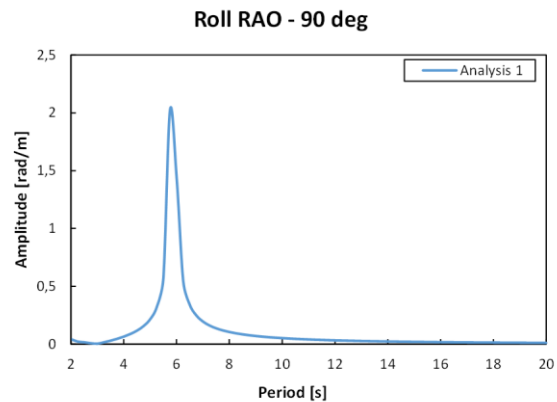
Figure 4-6: Roll RAO for beam waves - Analysis 1.
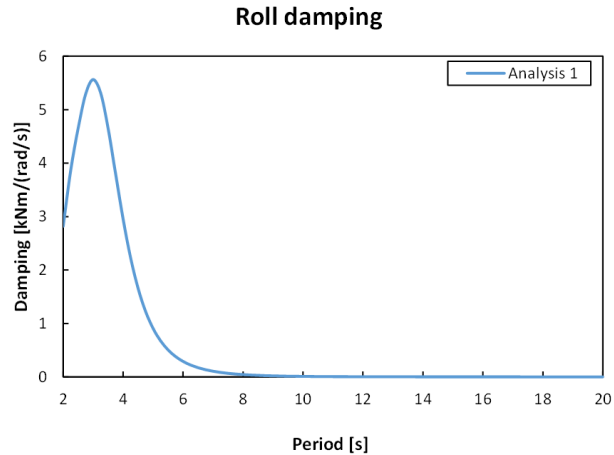
Roll damping

Figure 4-7: Roll damping - Analysis 1.

4.1.2   **Analysis 2 – Adding Damping Lid**

This analysis runs with the same conditions as Analysis 1, but with a damping lid around the vessel (Figure 3-3). The damping lid has a damping coefficient of 0,2. This feature is added to reduce the fluid resonance. The calculated natural periods for this analysis are presented in Table 4-3.

Table 4-3: Natural periods – Analysis 2.

	Value
Heave, $[s]$	3,1
Roll, $[s]$	6,2
Pitch, $[s]$	3,1
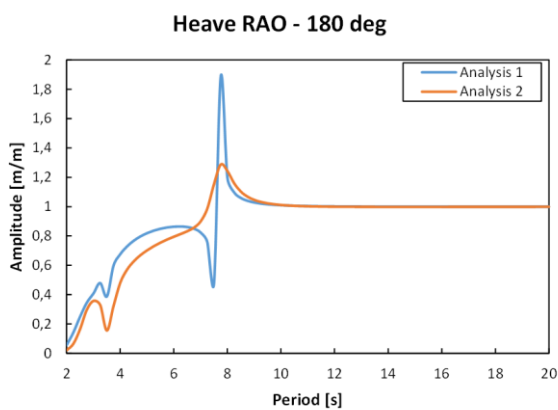
Figure 4-8: Heave RAO for head waves - Analysis 1 & 2.
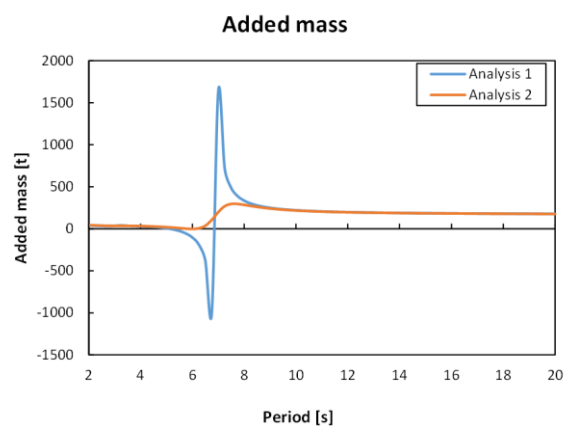
Figure 4-9: Heave added mass - Analysis 1 & 2.

As expected, the damping lid will reduce the response for many periods, which makes it important to further study where to apply the damping lid, and which damping coefficient to use. A sensitivity study using sea state RAO to investigate the fluid resonance is recommended. This was not done for this thesis. The intended effect of reducing the peak around 7,5 seconds can be seen in the plots, and the shape of the two graphs resembles each other. It is reassuring to see that the graphs approach an amplitude of 1 m/m when the wave period increases, since the vessel heave motion should "follow" the waves in high periods. Using a damping lid also makes the added mass stay above zero for all periods.

The new analysis indicates a distinct reduction of the added mass amplitude around the peak point, whereas the added mass for the lower and higher periods remain almost unchanged. This explains why the spike in the heave RAO changed a lot more than the rest of the graph. The heave RAO in beam waves gets an increased peak around 7,5 seconds when adding the damping lid. As with the heave RAO in head waves, the damping lid globally reduce the amplitude of the motion.
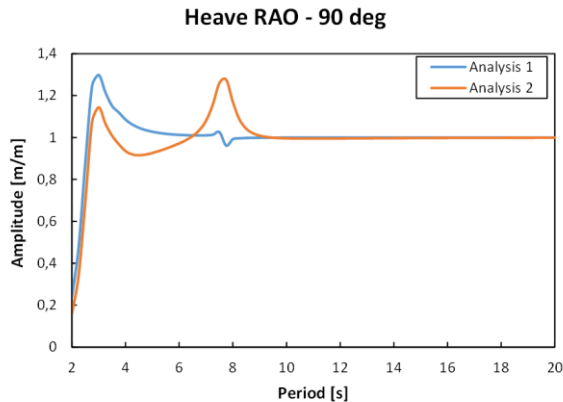
Figure 4-10: Heave RAO for beam waves – Analysis 1 & 2.
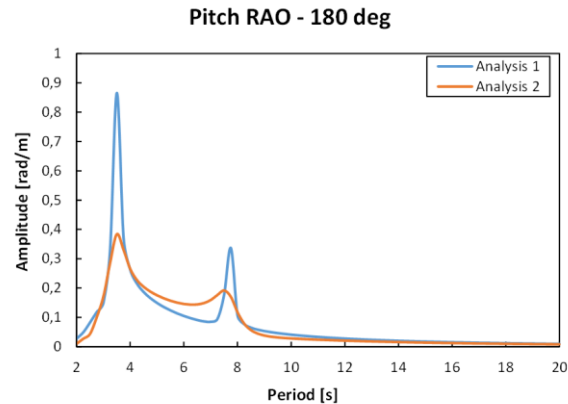
Figure 4-11: Pitch RAO for head waves - Analysis 1 & 2.

Adding the damping lid also "softens" the pitch motion, with the peaks remaining in the same area. The roll response in beam waves is unaffected by the added damping lid
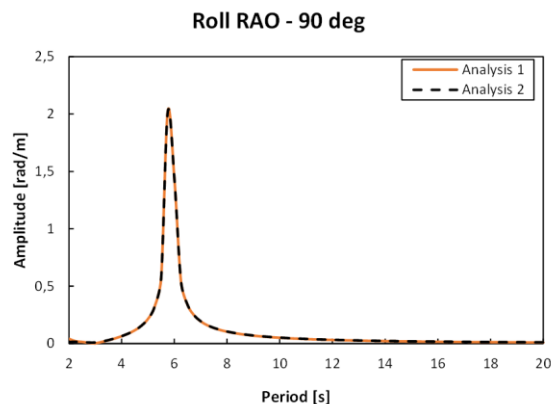
Figure 4-12: Roll RAO for beam waves - Analysis 1.

4.1.3   **Analysis 3 – Adding Viscous Roll Damping**

This analysis runs with the same conditions as Analysis 2, but with extra roll damping added as a constraint. $56\frac{kNm}{rad/s}$ of viscous roll damping is applied. The heave and pitch results are, as expected, unaffected by the additional roll damping. This applies to both beam waves and head waves. The calculated natural periods for this analysis are presented in Table 4-4.

Table 4-4: Natural periods – Analysis 3.

	Value
Heave, [s]	3,1
Roll, [s]	6,2
Pitch, [s]	3,1
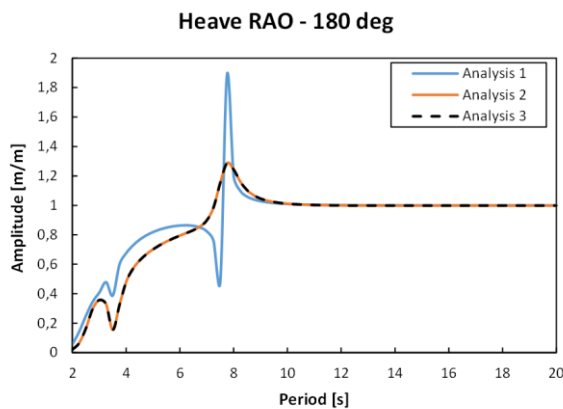
Figure 4-13: Heave RAO for head waves - Analysis 1, 2 & 3.
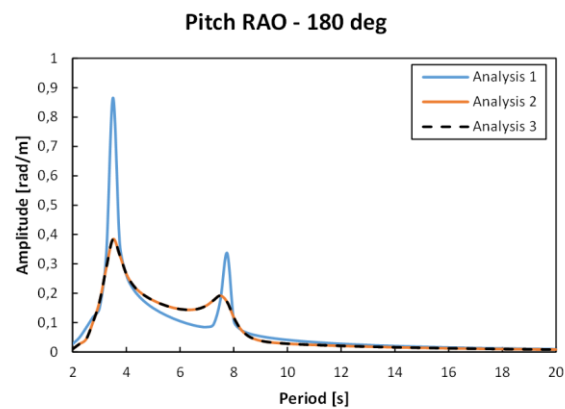
Figure 4-14: Pitch RAO for head waves – Analysis 1, 2 & 3.

The added roll damping does, however, majorly affect the roll responses in beam waves. When having a closer look at the new RAO data (Figure 4-16), it can be seen that the roll natural period coincides with the calculated natural period from Table 4-2. The calculated roll natural period is 6,2 seconds, whereas the peak in the RAO graph is at around 6 seconds.
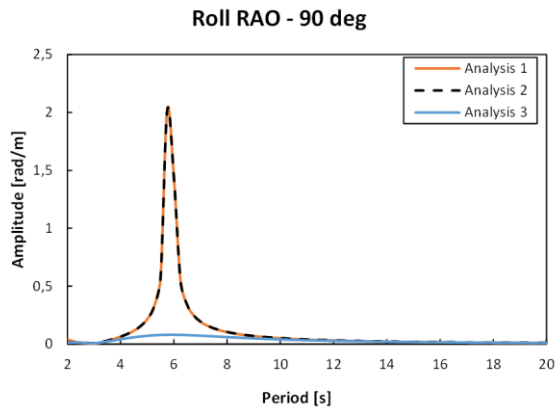
Figure 4-15: Roll RAO for beam waves - Analysis 1, 2 & 3.
Figure 4-16: Roll RAO for beam waves - Analysis 3.
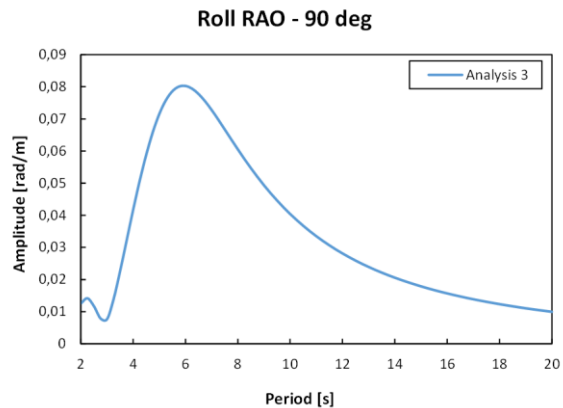
4.1.4 Analysis 4 – Trimmed Vessel

Analysis 4 runs with the same conditions as Analysis 3, but with a 3,66 degrees trim angle, due to external load at the stern of the vessel. Both Analysis 3 and Analysis 4 are exported to Orcaflex and they are therefore the ones being compared in this subchapter. The new natural periods, presented in Table 4-5, shows that roll is the most affected value.

Table 4-5: Natural periods – Analysis 4.

	Value
Heave, [s]	3,1
Roll, [s]	6,8
Pitch, [s]	3,2

The RAO graphs in general have the same shape as the RAO results from Analysis 3. From the heave RAO for head waves it can be seen that the peak at the natural period is slightly increased. The peak of interest in Analysis 1 & 2 has now shifted to the left. This does most likely have a correlation with the stern part of the vessel, which has now moved vertically down. This area is most likely the area where the fluid resonance causes the most "trouble".
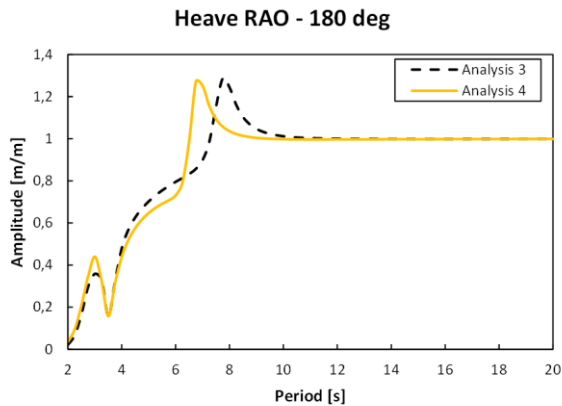
Figure 4-17: Heave RAO for head waves - Analysis 3 & 4.
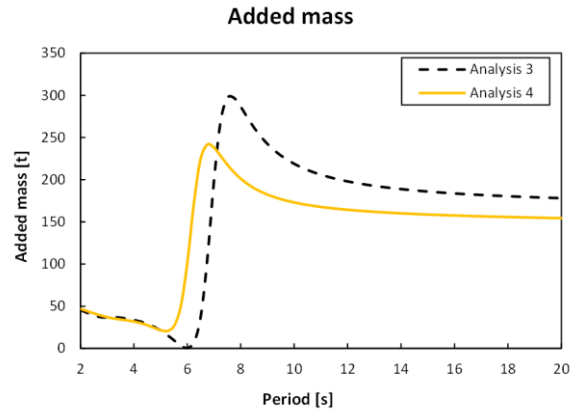
Figure 4-18: Heave added mass - Analysis 3 & 4.

The added mass graph, which still has the same shape, also shifts towards left. This explains why the heave RAO peak shifts towards left. As expected from the added mass information, the pitch peak is also moved towards lower periods. The magnitude of the peaks also changes a bit. The roll responses have the same shape as the responses for the vessel at even keel. The magnitude of the peak, however, is a bit decreased. The peak is slightly shifted towards higher wave periods, which is what the calculated natural period suggests.
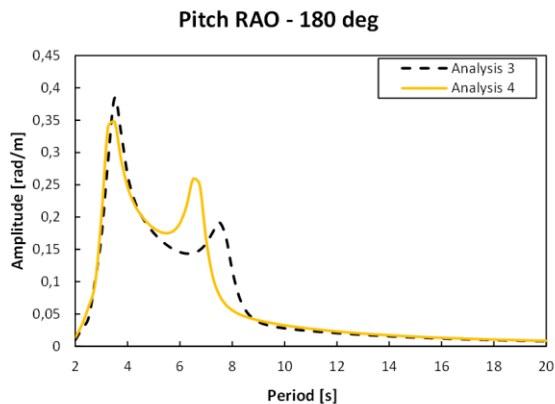
Figure 4-19: Pitch RAO for head waves - Analysis 3 & 4.
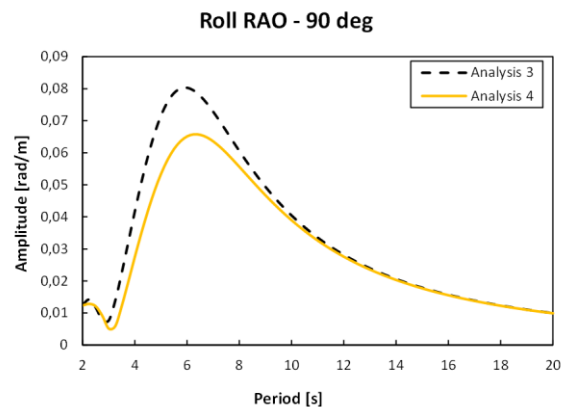
Figure 4-20: Roll RAO for beam waves - Analysis 3 & 4.

The pitch motion increases for the trimmed hydrodynamic analysis because of the difference in wave kinematics at the different levels of submergence. When the vessel is at even keel, the bow and the stern part of the vessel are located at the same submerged depth. When trimming the vessel, the aft part of the vessel will have a larger draught than the fore part of the vessel. This will result in a difference in vertical forces acting on the hull along the longitudinal axis of the vessel. This is further explained in Section 4.2.1.
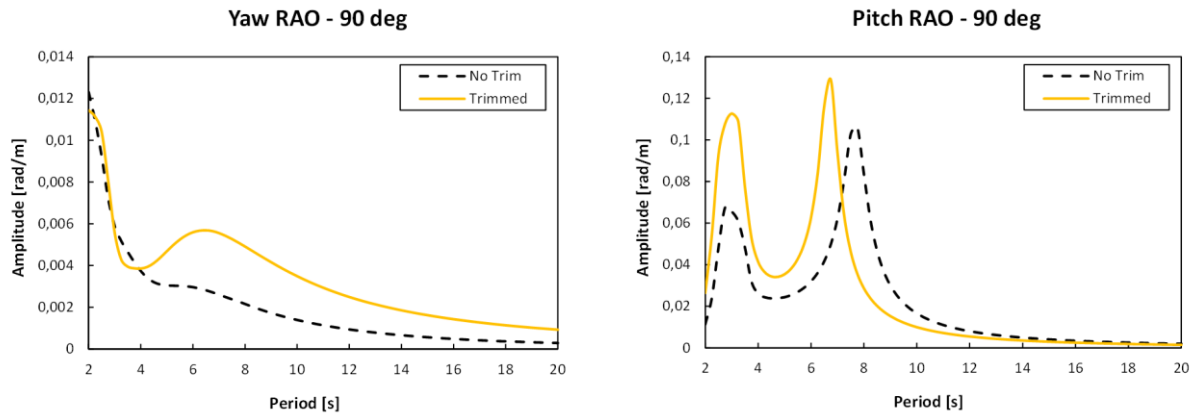
Figure 4-21: Comparison of yaw response and roll response with and without trimming angle for beam waves.

4.2   ITS Deployment Vessel

Since the effects of implementing viscous roll damping and damping lid is covered step by step in Section 3.3, this subchapter focuses on the difference between the vessel in upright position and with 3 degrees heeling angle. The natural period for heave, roll and pitch have been calculated in Appendix B. The results are presented in Table 4-6.

Table 4-6: Natural periods – ITS deployment vessel.

	Upright	3° heeling angle
Heave, $[s]$	7,7	7,8
Roll, $[s]$	12,3	12,3
Pitch, $[s]$	7,4	7,4

The difference in natural periods for the three most interesting responses, when analyzing a lifting operation, are negligible between the two cases.

4.2.1   Response Comparison

The three responses heave, pitch and roll for head sea, beam sea and waves arriving from 165 degrees are presented in Figure 4-22. These are the responses for the vessel when analyzed with no heeling angle. The 165 degrees responses are presented because this is the vessel heading that is normal to use during deployment of heavy objects.

Heave RAO - Upright
Heave RAO - 3 deg heeling angle
Roll RAO - Upright
Roll RAO - 3 deg heeling angle
Pitch RAO - Upright
Pitch RAO - 3 deg heeling angle
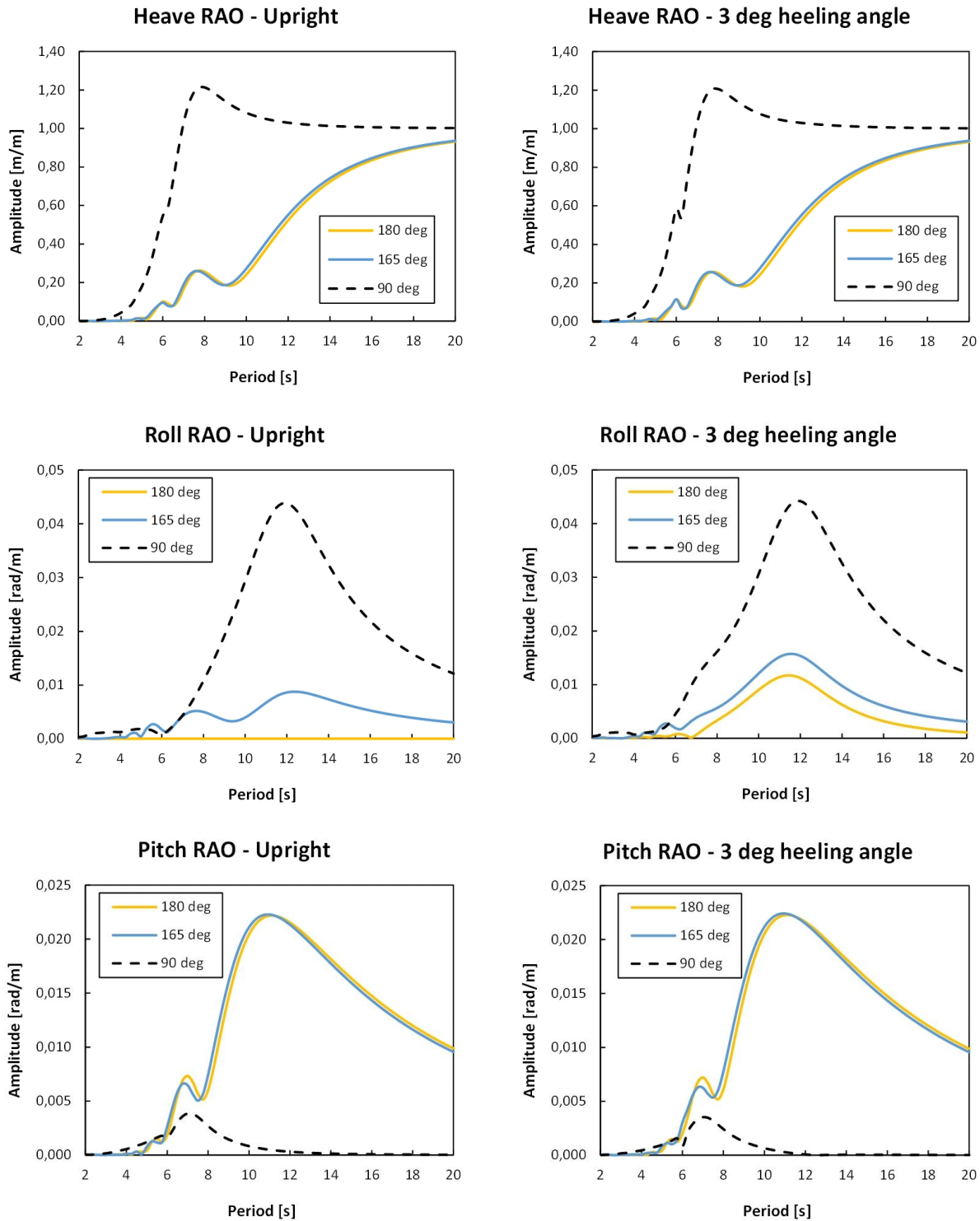
Figure 4-22: ITS deployment vessel – Heave, pitch and roll RAO.

Most of the responses are unaffected when introducing a 3 degrees heeling angle to the model. Neither the shape nor the size of the water plane area have changed a lot when listing the vessel towards port side. This means that the

hydrostatic properties such as stiffness in heave, roll and pitch direction stays relatively unchanged. This is reflected in the natural periods for the selected motions (Table 4-6). It can be seen in Figure 4-23 that the roll response in head waves have significantly changed. Normally the vessel will not experience roll motion when pointing towards the waves.

Roll RAO - 180 deg
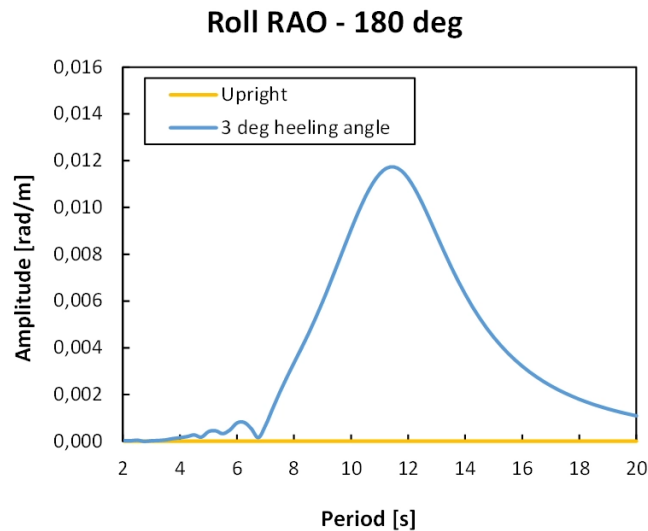
Figure 4-23: ITS deployment vessel - Comparison between roll responses for head waves.

The roll response in waves coming from 165 degrees has also increased, but not as significant as the head waves response. This can be explained by looking at the geometry rather than numbers. Figure 4-24 is the front view of the vessel while heeling 3 degrees. For a vessel with a 27 meters beam, a 3 degrees heeling angle will result in a 1,42 meters maximum difference in draught for each side of the vessel. When waves approaching the vessel directly towards the bow hits the hull, the port side and the starboard side will experience different magnitudes of wave kinematics at the same instant of time. This difference in wave kinematics will make the vessel roll.
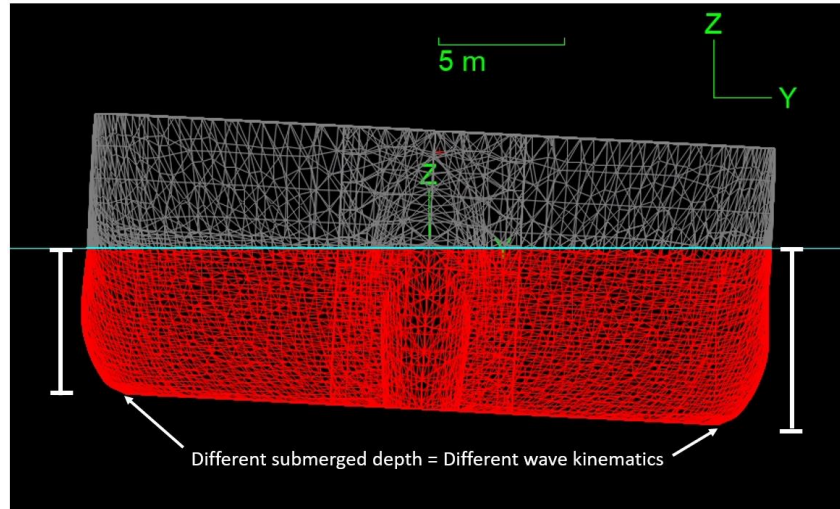
Figure 4-24: Front view of ITS deployment vessel.

For the sake of validating the results, the natural periods can be compared to the RAO graphs. All the graphs have peaks corresponding to the calculated natural periods. Some minor deviations are expected since the natural periods have been calculated using the infinite frequency added mass, while Orcawave uses the added mass for that given instant. An example of peak due to natural period is presented in Figure 4-25. It can also be seen in the same figure that the operator approaches 1 when the period increases. This means that for large periods the vessel will follow the "slow" motions of the waves. The time-dependent added mass for heave motion can be found in Figure 4-26. Same peak around 6 seconds can be seen in both the RAO graph and the added mass graph. This is due to the fluid resonance damped by the damping lid.
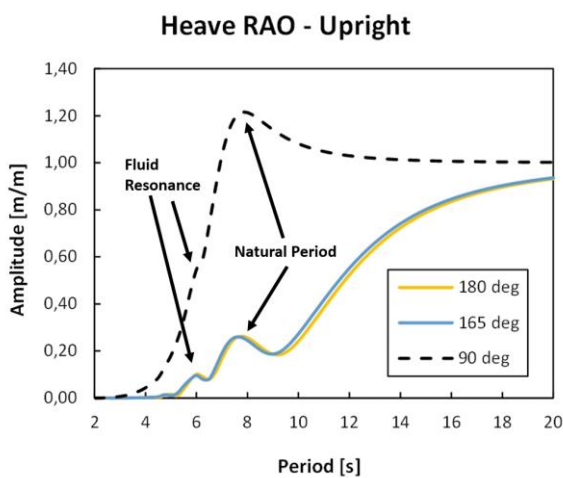
Figure 4-25: ITS deployment vessel – Upright heave RAO.
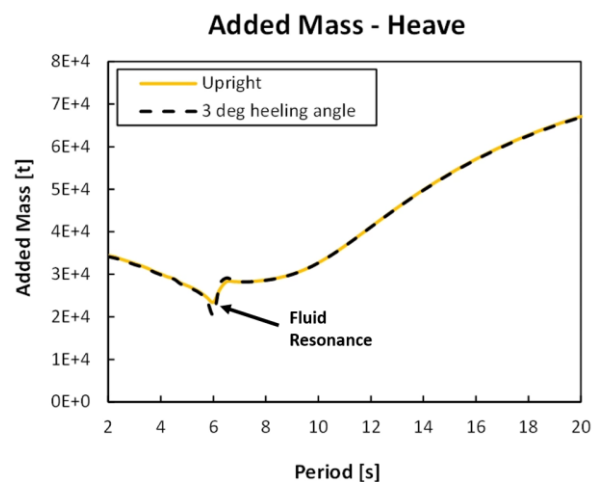
Figure 4-26: ITS deployment vessel – Heave added mass.

4.2.2 Shielding Results

The shielding results have been plotted as contour plots to show how the velocity potential RAO changes with the distance from the vessel and the distance from the vessel origin (Increasing distance from origin equals increasing distance from bow). The shielding effects has been estimated for all wave directions, but only the results for waves approaching from 165 degrees are presented in this subchapter. The difference between the calculated velocity potential RAO at the still water level and 3,9 meters submergence turned out to be negligible.

Li et al. [13] have investigated the effect of vertical decay when modeling the shielding effect for installation of offshore wind turbines. Their results indicate the same as this study. The rate of change with respect to depth is small for disturbed wave kinematics operators.
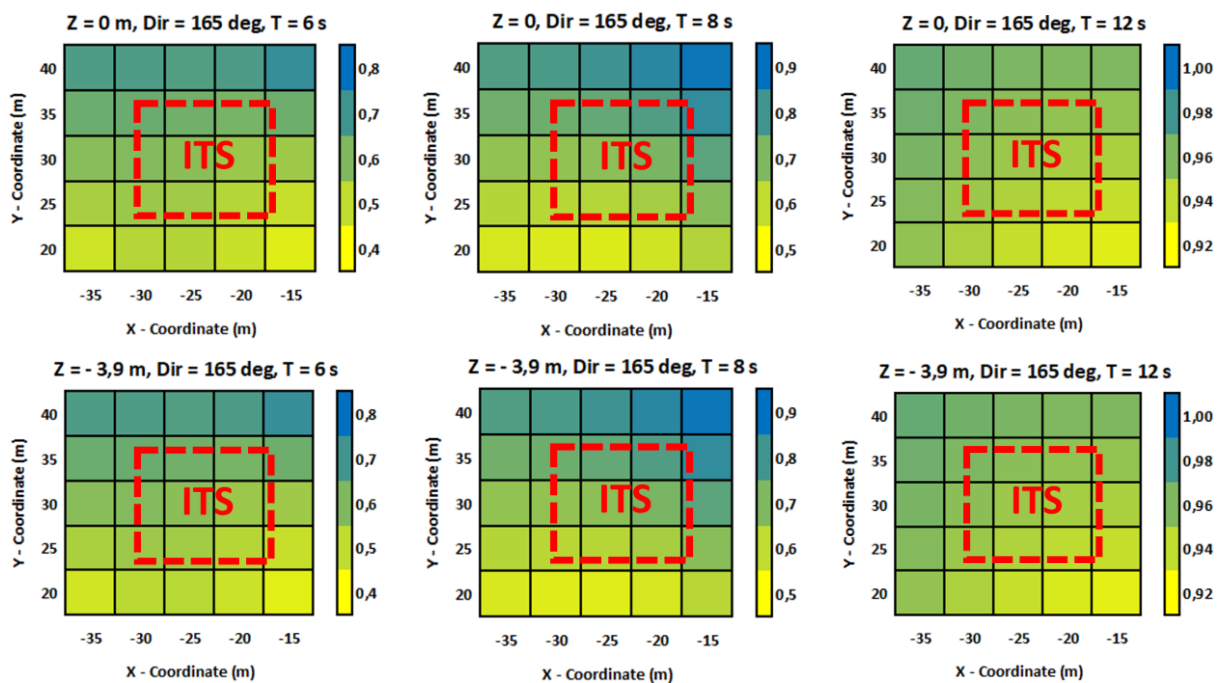
Figure 4-27: Velocity potential RAO near ITS deployment vessel.

Chapter 5

Numerical Models for Time Domain Simulations

This chapter presents the numerical models for both the ROV deployment and the ITS deployment. Both time domain simulations are conducted in the simulation software Orcaflex.

5.1 Numerical Tools

The results from the hydrodynamic analysis performed in Orcawave are imported directly into the analysis software Orcaflex. Orcawave produces both displacement - and load RAO, which can both be imported to Orcaflex. Wave load RAO defines the force and moment which a wave exerts on the vessel. Displacement RAO completely defines the vessel motion [22]. Using the load RAO combined with the vessels mass and inertia and any other load acting on the vessel, Orcaflex can determine the vessel motion from the equation of motion. Orcaflex can perform a wide range of static and dynamic analyses with buoys, vessel, etc. as typical boundary conditions. Orcaflex is widely used in the offshore industry, and covers among other: Risers, Moorings, Installation Analysis, Buoy systems, Hose systems, etc [22].

5.2 ROV Deployment

The ROV Vessel model is a combination of vessel, winch, lines and 6d buoys. The vessel is stationary, and the winch is paying out at a constant speed. Two different cases are described in this subchapter. The only difference between the two cases is the vessel RAO data.
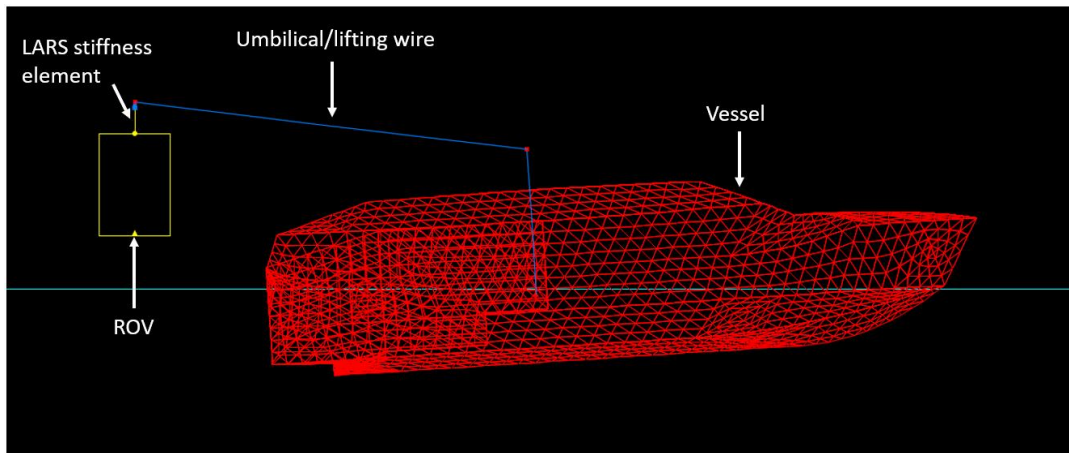
Figure 5-1: ROV deployment vessel in Orcaflex.

5.2.1   **Vessel Setup**

Two different vessel types are imported from Orcawave to the Orcaflex environment. One of them contains the RAO data for a vessel at even keel, while the other contains the RAO data for the same vessel with 3,66 degrees trim. This is to compare the responses of the vessel with and without the altered RAO data due to the load of the ROV hanging at the stern.

The vessel in the ROV deployment analysis is set up with Displacement RAO as a superimposed motion. This means that the predefined responses from Orcawave are used to calculate the motion of the vessel based on the incoming wave train. The forces acting from the ROV or any other external forces will not influence the motion of the vessel. The coupling between the vessel and the ROV will, however, make sure that the vessel motion influences the motion of the ROV. The RAO data includes an out-of-phase correlation to the wave amplitude, defining the timing of the motion relative to the wave. Displacement RAO has been chosen because it is difficult for the numerical tool to remove all the second-order wave load and the vessel will therefore in many cases tend to drift away. According to DNV-RP-H103 it is normally conservative to apply displacement vessel RAO as the lifted object in most cases will reduce the vertical motion [1].

5.2.2   **LARS Setup**

The Umbilical/lifting wire for the ROV system is modeled as a winch and includes the wire stiffness of the Umbilical. The wire stiffness for this launch and recovery system is 15000 kN. The winch is located near the vessel origin and is routed through a sheave on the LARS. This launch and recovery system extends and carries the ROV from deck to just outside of the vessel. From here the ROV is lowered into the sea at a constant velocity of 0,25 m/s. A 5 second period with payout rate of change is modeled to avoid going from zero to full speed on the winch in an instant of time. The LARS itself is not modeled. The sheave of the extended LARS is simply modeled as a point rigidly connected to

the vessel. The receptacle, which connects the lifting wire to the TMS, is modeled as a line element. This line element has a constant length, as opposed to the winch wire, and therefore it includes the constant stiffness of the launch and recovery frame. This is to ensure that the stiffness of the LARS frame do not change when the wire pays out.

Table 5-1: ROV vessel - Winch simulation settings.

	Stage duration, $[s]$	Simulation time at stage end, $[s]$	Mode	Value, $\left[\frac{m}{s}\right]$
Stage 0	65	0	Payout rate	0
Stage 1	30	30	Payout rate	0
Stage 2	5	35	Payout rate change	0,25
Stage 3	60	95	Payout rate	0,25

Table 5-2: Line element (LARS stiffness) properties.

	Value
Length, $[m]$	0,55
Axial stiffness, $[kN]$	1085,7

The simulation covers 65 seconds of build up before the ROV will be hanging in the LARS, released from the latching system, in 10 seconds. The winch starts to pay out at 30 seconds and increases the payout rate from 0 m/s to 0,25 m/s in a 5 second stage. The last stage is a 60 second stage where the winch pays out at a rate of 0,25 m/s.

5.2.3   **ROV System**

The ROV in this study is a "Panther Plus" light construction work ROV. The Panther Plus is deployed inside an entry garage TMS which has an overall height of 2,1 m and a length of 1,8 m. The width is 1,5 m. For the sake of the analysis this ROV-TMS combination is considered one unit, a rectangular box. The properties for the ROV studied in this thesis is given in Table 5-3 and Table 5-4.

Figure 5-2: Panther Plus ROV [33].

Table 5-3: ROV general properties.

	Value
Length, $[m]$	1,79
Width, $[m]$	1,49
Height, $[m]$	2,1
Mass, $[t]$	1,9
Volume, $[m^3]$	0,878

Table 5-4: ROV Inertia and geometric properties.

	X	Y	Z
Mass moment of inertia, $[m^2 t]$	1,21	1,05	0,86
Centre of mass, $[m]$	0	0	0
Centre of volume, $[m]$	0	0	0

5.2.4 Modeling of Hydrodynamic Forces

The Orcaflex model of the ROV consists of two lumped buoys. One of the buoys contains all the geometrical and hydrodynamic properties of the ROV-TMS system. The other buoy, called the slam buoy, has all negligible properties except the slamming coefficient, the slamming area and the height. The slamming area must be specified for the lumped buoys in Orcaflex when using constant slamming data. This is because the lumped buoys do not have a specific

geometry. Applying the slamming load using constant data gives a discontinuous step change in applied load to the buoy. This causes problem when running a time domain simulation. To mitigate this in Orcaflex the slamming load is ramped up to its full value during the first 10% of the buoy submergence. The same exercise is done for the last 10% of the buoy submergence to avoid a discontinuous step change when reducing the load [22]. The slamming force is slightly increased during the 80% in the middle to make sure that the total slam impulse is correct (Figure 5-3).
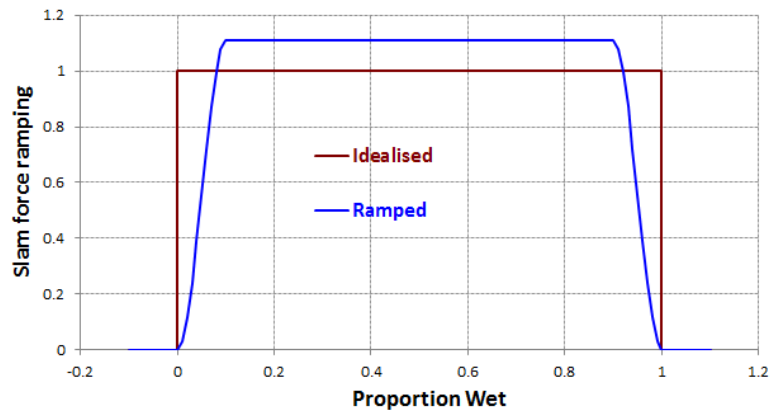
Figure 5-3: Lumped buoy slam force ramping [22].

Proportion wet is the ratio between total buoy volume and submerged buoy volume. The slamming load is applied to the instantaneous center of wetted volume for lumped buoys. To ensure that the slamming load is applied to the bottom of the TMS, the slam buoy height must be as short as possible. If the slamming buoy is too short and the time step for the time domain simulations are large, the slamming buoy might pass through the water surface entirely without the slamming force being included. Finding a proper height for the slam buoy can be done by running sensitivity studies. The slam buoy height for the ROV deployment simulations in the study is set to 0,1 m.
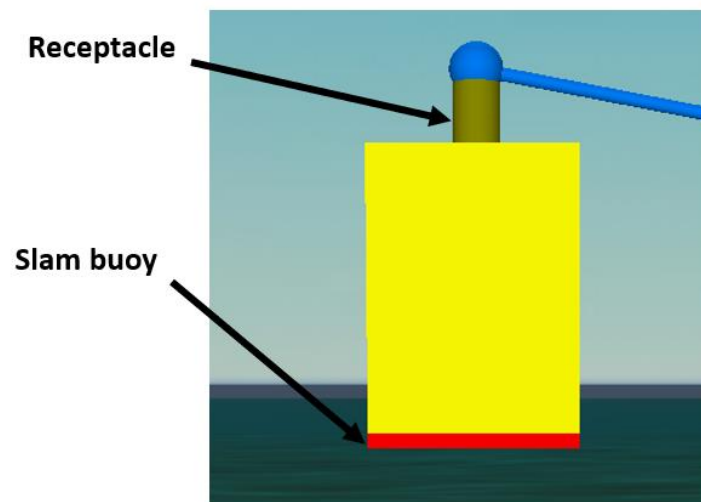
Figure 5-4: ROV model in Orcaflex.

The hydrodynamic properties for the ROV is calculated according to DNV's recommended practice for modeling and analysis of marine operations, [1] and the Orcaflex 6d buoy documentation [22]. The full set of calculations is presented in APPENDIX C.

Translational Drag Coefficient

The drag coefficient for the ROV is calculated according to Appendix B in DNV's recommended practice for modeling and analysis of marine operations [1]. The rectangular flat plate properties have been used since length-to-width ratio exceeds the limits for the square rod parallel to flow. The drag coefficient is approximately 1,16 in both horizontal directions. According to the guidance note in the recommended practice, the drag coefficient for typical subsea structures in oscillatory flow can be taken as 2,5. This is applicable in the absence of a specific CFD analysis. The drag coefficient in vertical direction is therefore taken as 2,5 for this study.
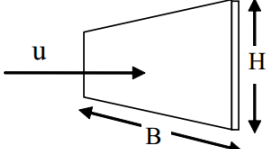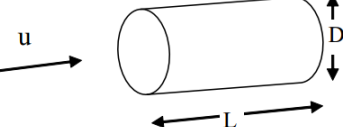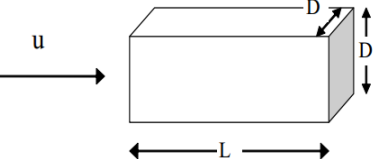
Geometry	Dimensions	C_{DS}
Rectangular plate normal to flow direction	B/H	
	1 5 10 ∞	1.16 1.20 1.50 1.90
		$R_e > 10^3$
Circular cylinder. Axis parallel to flow.	L/D	
	0 1 2 4 7	1.12 0.91 0.85 0.87 0.99
		$R_e > 10^3$
Square rod parallel to flow	L/D	
	1.0 1.5 2.0 2.5 3.0 4.0 5.0	1.15 0.97 0.87 0.90 0.93 0.95 0.95
		$R_e = 1.7 \cdot 10^5$

Figure 5-5: DNV-RP-H103, Table B-2: Drag coefficient on three-dimensional objects for steady flow [1].

Translational Added Mass

The translational added mass is calculated according to Appendix A in DNV-RP-H103 [1], using the analytical added mass for flat plates. The flat plate added mass is then converted to added mass for a three-dimensional body. This is a simplified method for heave direction, but it is assumed to also be valid as an approximation for horizontal direction. The added mass is given as a relation between the fluid density, the added mass constant and the reference volume.

$$A_{33o} = \rho C_A V_R \qquad (94)$$

The reference volume is the volume that is being moved by the motion of the body. Equation (95) relates the added mass for flat plates to added mass for three-dimensional bodies. A_p is the area of submerged part of the object projected on a horizontal plane (vertical plane when investigating the horizontal added mass).

$$A_{33s} = \left(1 + \sqrt{\frac{1 - \lambda^2}{2(1 + \lambda^2)}}\right) \cdot A_{33o} \qquad (95)$$

$$\lambda = \frac{\sqrt{A_p}}{h + \sqrt{A_p}} \qquad (96)$$

The effect of perforation is taken into account by assuming a 10% perforation in each of the 3 directions. According to the recommended practice from DNV [1], the perforation can roughly be estimated by the use of Equation (97).

$$A_{33} = \begin{cases} A_{33s} & ; p \leq 5 \\ A_{33s} \cdot \left(0{,}7 + 0{,}3 \cos\left(\frac{\pi(p - 5)}{34}\right)\right) & ; 5 < p < 34 \\ A_{33s} \cdot e^{\frac{10 - p}{28}} & ; 34 \leq p \leq 50 \end{cases} \qquad (97)$$

The intention of the guidance in DNV-RP-H103 [1] is to ensure that the influence of perforation is conservatively accounted for when estimating the influence on the added mass. Figure 5-6 shows a comparison between the curve from DNV (Equation (97)) and a number of different model tests. Following this guidance will in most cases significantly overestimate the added mass.
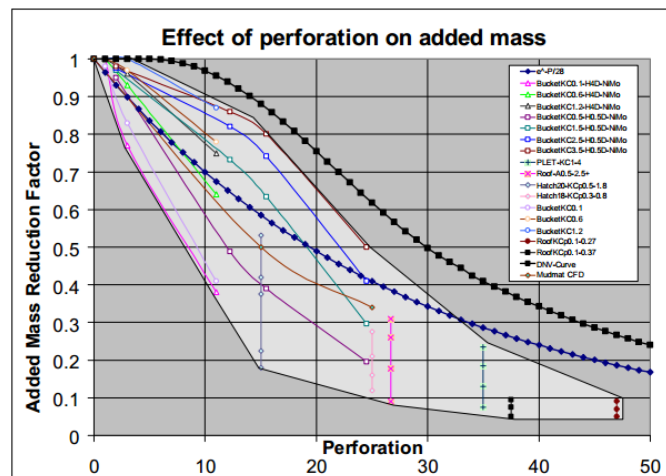
Figure 5-6: Added mass reduction factor as function of the perforation rate (percentage) [1]..

The final step is to divide the calculated added mass on the hydrodynamic mass to obtain the added mass constant that Orcaflex requires as input.

Translational Inertia Coefficient

Orcaflex uses an extended form of the Morrison equation, much like Equation (74) which is presented in section 2.4. By comparing the equation from Section 2.4 and the equation Orcaflex uses it can be seen that $C_m = 1 + C_a$. This is also the value Orcaflex uses if no input is given [22].

$$f(t) = \left(C_m \Delta a_f - C_a \Delta a_b \right) + \frac{1}{2} \rho C_d A |v_r| v_r \tag{98}$$

C_m = Inertia coefficient

a_f = Fluid acceleration

C_a = Added mass coefficient

Δ = Mass of fluid displaced by the body

a_b = Body acceleration relative to earth

C_d = Drag coefficient

v_r = Fluid velocity relative to body

Summary of Translational Hydrodynamic Properties

The ROV translational hydrodynamic properties, used as input for this time domain simulation, are presented in Table 5-5.

Table 5-5: ROV translational hydrodynamic properties.

	X	Y	Z
Drag area, $[m^2]$	3,76	3,13	2,67
Drag coefficient, $[-]$	1,16	1,16	2,5
Hydrodynamic mass, $[t]$	0,9	0,9	0,9
Added mass coefficient, $[-]$	5,49	4,22	3,45
Inertia coefficient, $[-]$	6,52	5,19	4,45

Rotational Drag Coefficient

The rotational properties are calculated according to Orcina's guidance note for hydrodynamic properties for rectangular boxes [22]. The drag moment is calculated based on the drag force contribution on an area at a certain distance from the rotational axis. The box in Figure 5-7 is considered to be rotating around the x-axis. Drag forces on both area A_y and area A_z contributes to cause a moment around the x-axis. The drag force on the elementary strip

shown in the figure can be written as Equation (99). The moment caused by the force on the elementary area can be written as Equation (100). Integrating this equation over the entire area gives the total moment around the x-axis caused by drag forces in y-direction(Equation (101)).
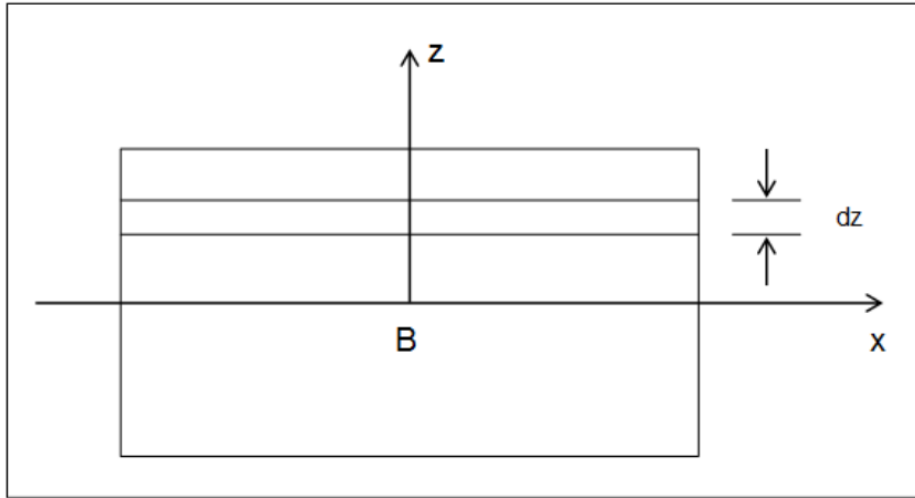
Figure 5-7: Integration for rotational drag properties [22].

$$df = \frac{1}{2}\rho\omega z|\omega z|C_d x dz \tag{99}$$

$$dm = \frac{1}{2}\rho\omega|\omega|z^3 C_d x dz \tag{100}$$

$$m = \frac{1}{2}\rho\omega|\omega|C_d \frac{xz^4}{32} \tag{101}$$

$$A_m = \frac{xz^4}{32} \tag{102}$$

Both the rotational drag moment of area, A_m, and the rotational drag coefficient are input for Orcaflex. By simply setting the rotational drag coefficient equal to 1 the rotational drag moment of area can be calculated as per Equation (103) [22]. This equation is an example for rotation around the x-axis and includes contribution from both the y-area and the z-area.

$$A_{mx} = \frac{x}{32}(z^4 C_{dy} + y^4 C_{dz}) \tag{103}$$

Rotational Added Mass Coefficient

DNV's recommended practice for modelling and analysis of marine operations [1] does not contain information about rotational added mass. The Orcaflex help documentation [1] refers to John Newman's Marine Hydrodynamics [34] which presents information about rotational added mass for spheroids. It is assumed that the rotational added mass for spheroids can be used as a basis for calculation of the rotational added mass for rectangular boxes [22]. The added inertia in Marine Hydrodynamics [34] refers to the moment of inertia of the displaced mass (Equation (104)). This equation covers rotation about the x-axis. The added mass coefficient can be found by calculating the ratio between half the length in flow direction, a, and the equivalent radius normal to flow, b. The ratio will then be used as input for Figure 5-8, where m''_{55} is the rotational added mass coefficient. When $\frac{b}{a} < 1{,}6$ the upper part of the figure can be used directly in correlation with the hydrodynamic inertia. If the lower part is used, the added mass coefficient must be corrected to be related to the hydrodynamic inertia. The equations below are examples for rotation about the x-axis.

$$HI_x = \frac{\Delta(y^2 + z^2)}{12} \tag{104}$$

$$a = \frac{x}{2} \tag{105}$$

$$\pi b^2 = yz \;\rightarrow\; b = \sqrt{\frac{yz}{\pi}} \tag{106}$$

$$\frac{b}{a} = \frac{2\sqrt{\frac{yz}{\pi}}}{x} \tag{107}$$

$$C_a = CA \cdot \frac{2b^3}{a(a^2 + b^2)} \tag{108}$$
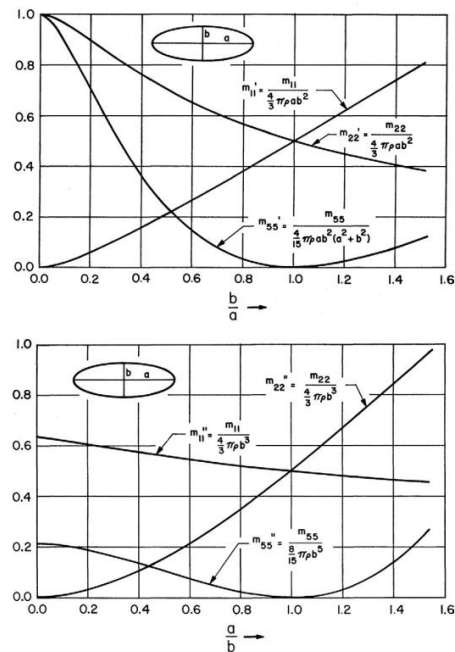
Figure 5-8: Added mass coefficient for a spheroid with length 2a and maximum diameter of 2b [34].

Summary of rotational hydrodynamic properties

The ROV rotational hydrodynamic properties, used as input for this time domain simulation, are presented in Table 5-6.

Table 5-6: ROV rotational hydrodynamic properties.

	X	Y	Z
Drag moment of area, $[m^5]$	2,25	1,96	1,16
Drag coefficient, $[-]$	1	1	1
Hydrodynamic inertia, $[m^2 Te]$	0,57	0,50	0,41
Added mass coefficient, $[-]$	0,1	0,01	0,02

Slamming Properties

The slamming properties are added to a separate buoy, rigidly connected to the main buoy. This buoy is located at the bottom of the main buoy and has only negligible properties, except slamming properties. The slamming area is simply the bottom area of the ROV, which is a separate input in Orcaflex for lumped buoys. The slamming coefficient (Equation (110)) is calculated according to DNV's recommended practice for modeling and analysis of marine

operations [1]. The rate of change is the total added mass for the ROV in vertical direction divided by the height of the slamming buoy. The exit slamming coefficient can be written as half the entry slamming coefficient.

$$\frac{dA_{33}}{dh} = \frac{A_{33}}{h} \tag{109}$$

$$C_{s.Entry} = \frac{2}{\rho A_p v_s} \frac{dA_{33}}{dt} = \frac{2}{\rho A_p} \frac{dA_{33}}{dh} \tag{110}$$

$$C_{s.Exit} = \frac{1}{\rho A_p} \frac{dA_{33}}{dh} = \frac{C_{s.Entry}}{2} \tag{111}$$

Table 5-7: ROV slamming properties.

	Value
Slamming area, $[m^2]$	2,627
Slam force coefficient - Entry, $[-]$	23,65
Slam force coefficient - Exit, $[-]$	11,82

5.2.5   **Environmental Conditions**

The waves are randomly generated as a wave train using the JONSWAP wave spectrum. Reference is made to Section 2.1.3 and Equation (30). Several combinations of significant wave heights, H_s, and Spectral peak periods, T_p are analyzed in order to search for the allowable sea state. Increments of 0,25 m for the significant wave height is chosen for this study. The spectral parameters are listed in Table 5-8, where the sigma values relate to the average JONSWAP spectrum [1]. The mean zero up-crossing period for this study has increments of 1 second.

Table 5-8: Spectral parameters.

	Value
Gamma, γ	Equation (32)
Sigma 1, σ_1	0,07
Sigma 2, σ_2	0,09
Zero-up-crossing periods, T_z	Equation (31), 1 second increments
Significant wave height, H_s	0,25 m increments
Spreading coefficient, n	2

The spectral parameters result in a frequency spectrum similar to the example presented in Figure 5-9.
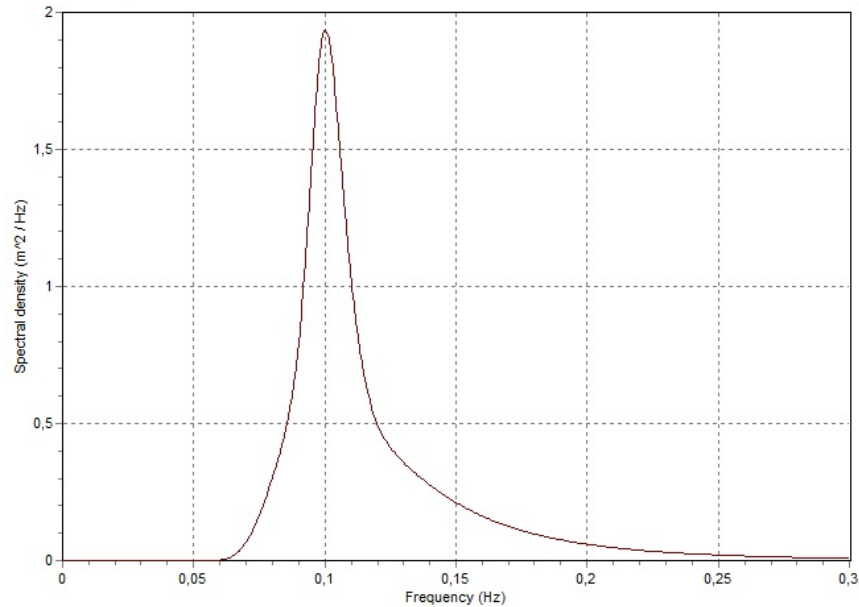
Figure 5-9: Example spectral density for wave train in Orcaflex (Hs=1 m, Tp=10 s)

The waves are modeled in two different directions to capture whether beam seas or head seas causes the lower allowable operational sea state.

5.2.6   Simulation Setup

The simulations are performed as implicit time domain simulations with a constant time step as recommended [22]. The default time step of 0,1 seconds is kept, and the simulation time is set to be 95 seconds. The build-up time is set to be 65 seconds. The long build-up period is required to remove any asymmetry in the loading that can appear in short build-up periods.

Table 5-9: Time domain simulation matrix – ROV Deployment

	RAO Input	Vessel Motion	Wave Direction [°]	T_z [s]
Simulation Set 1	Even Keel	Uncoupled	180	2-13
Simulation Set 2	Even Keel	Uncoupled	90	2-13
Simulation Set 3	Trimmed	Uncoupled	180	2-13
Simulation Set 4	Trimmed	Uncoupled	90	2-13

5.3 ITS Deployment

The construction vessel model is a coupled model including vessel, lines, 6d buoys, 3d buoys, winch, links and constraints. The model is set up to start with the ITS ready in lowering position before the ITS is lowered down below the sea surface. Two different cases are described in this subchapter. The only difference between the two models is the vessel RAO data.
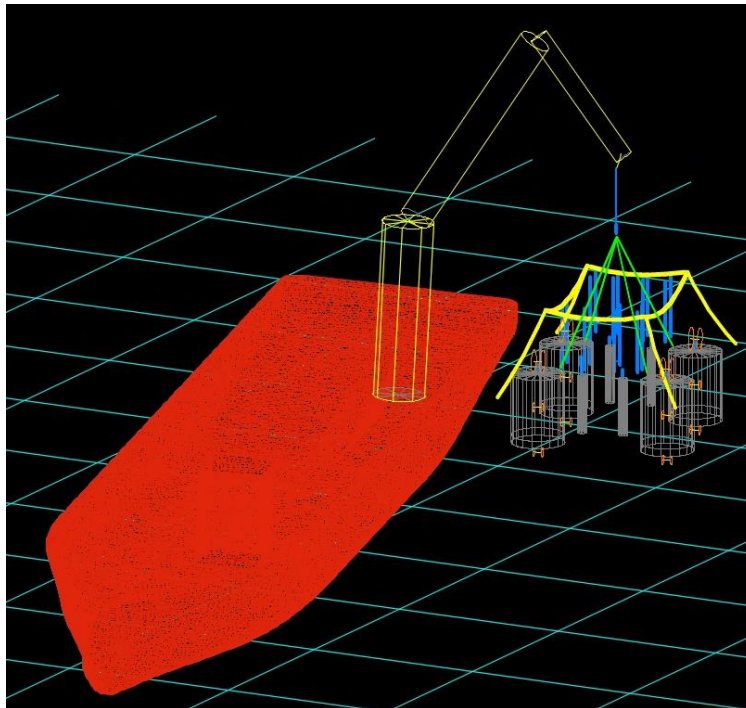
Figure 5-10: ITS deployment vessel numerical model.

5.3.1 Vessel Setup

As described in Section 3.4, two sets of load RAO have been created using Orcawave. The first set of RAO data describes the vessel responses in upright position, while the second set of RAO data describes the vessel responses with a three degrees heeling angle.

As mentioned in the section about vessel setup for the ROV deployment vessel (ref. Section 5.2.1), use of load RAO requires some strategically positioned links to keep the vessel from drifting out of position. All the three links used to keep the vessel in position have vertical connection points at the same height as the free surface. They are modeled as linear springs with a stiffness of 50 kN/m and a length of 1000 meters. The two links restraining sway and yaw motion are connected at the longitudinal center line, in each their end of the vessel. The surge restraining link is connected at the RAO origin and points along the longitudinal axis of the vessel.

The link setup is verified by running a set of simulations with different zero up-crossing wave periods. The simulations have a build-up time of 100 seconds, and a normal simulation time of 1 hour. Both beam and head sea have been scanned. The purpose of the simulations is to compare the displacement RAO responses with the load RAO responses when the links are attached to the vessel defined by load RAO. Too soft springs will not sufficiently restrain the vessel in horizontal direction and may allow it to become unstable. Too stiff links will reduce the energy in the three motions of interest: heave, roll and pitch. The examples in Figure 5-11 demonstrate that a link stiffness of 50 kN/m is found to be acceptable. The links are 1000 meters long to minimize their contribution in the vertical direction.
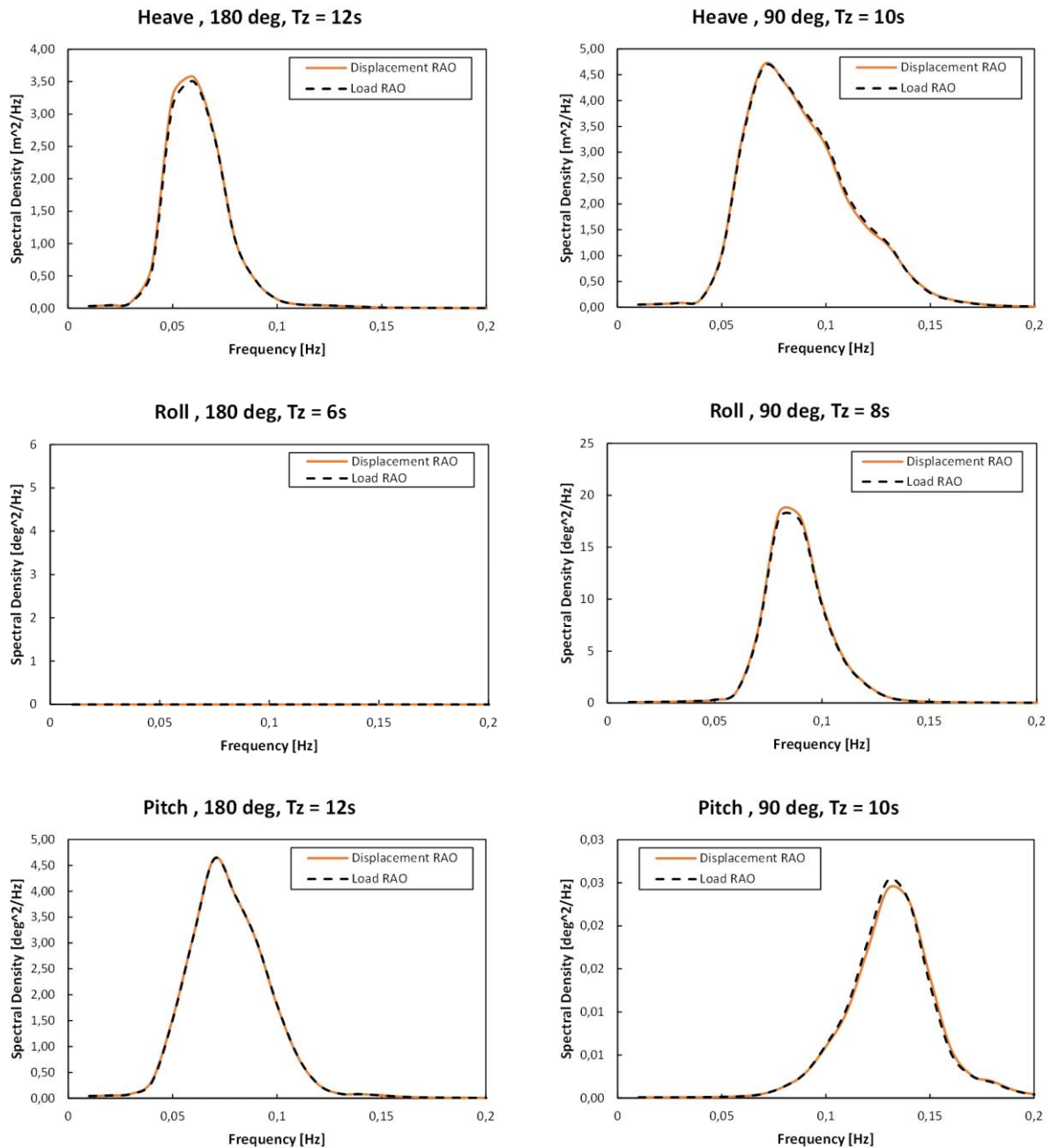
Figure 5-11: Spectral density comparison between displacement RAO and load RAO in Hs = 2 m.

5.3.2   **Lifting Setup**

The crane is modeled using constraints and shapes (shapes are only used to visualize and has no impact on the numerical model). The constraints make it possible to manipulate the crane in terms of slewing angle, crane boom angle, etc. This is not necessary for this study, but it can be useful if the overboarding phase of the lift were to be studied. The constraint positions and orientations are given in Table 5-10. They correspond to a crane radius of 24,5 m and a crane tip position of (-23.5, 35.0, 34.2) relative to the RAO origin.

Table 5-10: Crane constraint specifications.

	Connected to	X, [m]	Y, [m]	Z, [m]	Azimuth, [°]	Declination, [°]	Gamma, [°]
Crane pedestal	Vessel	-23,45	10,5	1,02	90,0	0,0	0,0
Crane boom	Crane pedestal	0,75	0,0	20,50	0,0	30,0	0,0
Crane jib	Crane boom	0,0	0,0	26,0	0,0	111,0	0,0
Crane tip[4]	Crane jib	0,0	0,0	16,0	-	-	-

The azimuth, declination and gamma angle are defined as rotation around the z-, y- and x-axis. The coordinates are relative to the axis of the object/constraint that the constraint is connected to.

Figure 5-12: ITS lifting setup.

---

[4] The crane Tip is not a constraint, but a connection point for the crane stiffness line.

The crane stiffness is modeled in a similar manner as the LARS stiffness for the ROV vessel except that the line element is located above the winch wire. The ITS is lifted using a 4-part lifting set. The lifting slings are connected in each their corner of the ITS (at the location of the designated lifting points) and joined in a 3d buoy representing the crane block. The crane block has a mass of 12,8 Te and no hydrodynamic properties. The 4-part lifting arrangement is modeled with 4 individual links. Links can either be acting as springs or tethers, which decides how they act when passing the point of 0 tension. The lifting slings are modeled as tethers meaning that they will become slack if no tension is present. The winch wire is set to pay out according to Table 5-11. The winch wire has an initial length of 8 m and a constant stiffness of 1 238 000 kN.

Table 5-11: Construction vessel - Winch simulation settings.

	Stage duration, $[s]$	Simulation time at stage end, $[s]$	Mode	Value, $\left[\frac{m}{s}\right]$
Stage 0	8	0	Payout rate change	0,2
Stage 1	120	120	Payout rate change	0

Table 5-12: Line element (crane stiffness) properties.

	Value
Length, $[m]$	1
Axial stiffness, $[kN]$	6000
Rayleigh damping ratio (stiffness proportional), $[\%]$	2,0

The lifting slings in the 4-part lifting arrangement have linear properties according to Table 5-13.

Table 5-13: Lifting slings properties.

	Value
Unstretched length, $[m]$	15,575
Axial stiffness, $[kN]$	195e3

5.3.3   **ITS Model**

The ITS is a typical subsea template, which is to be installed on the seabed. It consists of 4 suction anchors, 4 tailpipes, 16 guideposts, a base frame and a top structure. The suction anchors are hollow with a roof plate on top. These roof plates have two ventilation holes each, which are too small to evacuate the trapped water while lowering the template.

The tailpipes are open ended and will therefore have negligible added mass in vertical direction. The main properties for the template are given in Table 5-14. The vertical center of gravity for the entire structure is located approximately at the same height as the top of the suction anchors.

The ITS model is a combination of lines, 3d buoys and 6d buoys. Everything is connected to a common 6d buoy called the master node. This buoy has only negligible properties and serves its only purpose by connecting everything together. The suction anchors and the tailpipes are modeled as 6d spar buoys. The guideposts are represented with 3d buoys. The base frame, which connects the tailpipes, suction anchors and guideposts together, are modeled as 12 individual lumped 3d buoys. The top structure, which serves as a protection for the template, is modeled using line elements.

Normally, several tugger winches are connected in such heavy lifts. They are mainly present to control the horizontal motion during the overboarding phase of the lift, but they are left connected until the object is lowered to approximately 50 m water depth. At this stage the ROV disconnects the tugger wires from the object. The tugger winches have been excluded from this study since they are not considered necessary for pendulum control during lowering through the splash zone.

Table 5-14: ITS main properties.

	Value
Overall length, $[m]$	29,0
Overall width, $[m]$	20,8
Overall height, $[m]$	16,5
Mass, $[t]$	335,0
Weight in water, $[kN]$	2546,2
Suction anchor OD, $[m]$	6,0
Suction anchor height, $[m]$	7,9
Tailpipe OD, $[m]$	1,0
Tailpipe height, $[m]$	6,5
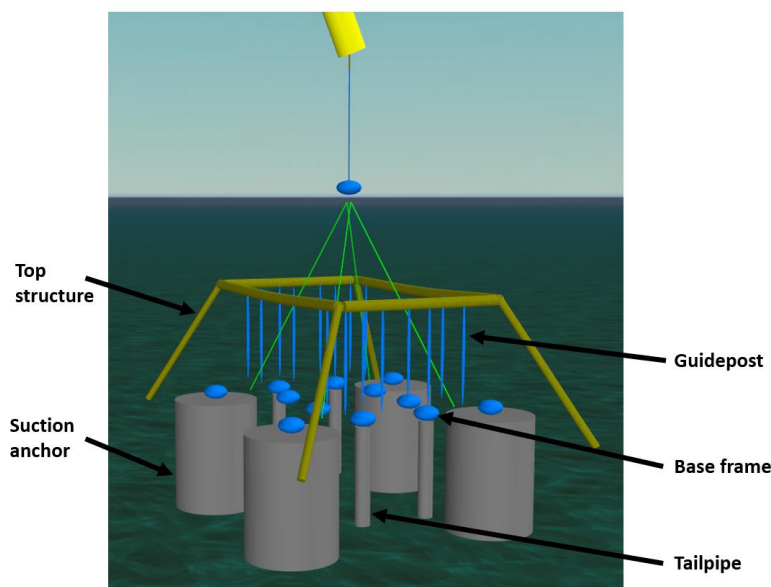
Figure 5-13: ITS model.

The hydrodynamic properties for the ITS is calculated according to DNV's recommended practice for modeling and analysis of marine operations, [1]. The full set of calculations is presented in APPENDIX D.

Table 5-15: Inertia properties.

	X	Y	Z
Mass moment of inertia, $[m^2t]$	16000	19000	27000

5.3.4 **Modeling of Hydrodynamic Forces**
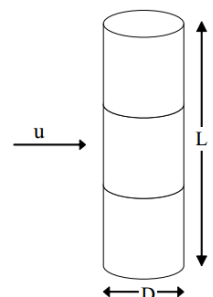
Morison's equation should only be used on slender elements relative to the size of the wave. The diameter of the element should not be larger than the wavelength divided by 5 (ref. section 2.4). This means that the lowest wave period, where the estimation of the added mass and drag is valid, is 4,4 seconds. This applies to the suction anchor, which is the element with the largest diameter. Deep water waves are assumed since the study is not field specific.

$$T \geq \sqrt{\frac{10D \cdot \pi}{g}}$$
(112)

Drag Coefficient for Circular Members

The horizontal drag coefficient is calculated according to DNV's recommended practice for modeling and analysis of marine operations [1]. This method is applied to all main circular members present on the template (i.e. suction anchors,

tailpipes, guideposts and top structure members). The 2d steady flow drag coefficient is taken as the coefficient for rough cylinders, $C_{DS}^{\infty} = 1,05$. The 3d steady flow drag coefficient, C_{DS}, is found as the product of the reduction factor, κ, and the 2D steady drag coefficient. As mentioned in section 2.4.2, the drag coefficient in oscillating flow is the product of the wake amplification factor, $\psi(K_c)$, and the steady flow drag coefficient (Equation (78)). The wake amplification factor can be found from Figure 2-10, where the KC-number in deep water (at still water level) is given by Equation (113) [19].

Circular cylinder normal to flow.		L/D	Sub critical flow $R_e < 10^5$	Supercritical flow $R_e > 5 \cdot 10^5$
			κ	κ
		2	0.58	0.80
		5	0.62	0.80
		10	0.68	0.82
		20	0.74	0.90
		40	0.82	0.98
		50	0.87	0.99
		100	0.98	1.00

$$C_{DS} = \kappa C_{DS}^{\infty}$$

κ is the reduction factor due to finite length. C_{DS}^{∞} is the 2D steady drag coefficient.

Figure 5-14: Drag for circular cylinder normal to flow [1].

$$KC = \frac{\pi L}{D} \tag{113}$$

Drag Coefficient for Bottom Structure

The drag coefficient for the bottom structure is calculated in a similar manner as the translational drag coefficients for the ROV in Section 5.2.3. The horizontal drag properties are calculated using the rectangular flat plate from Figure 5-5. This gives the 3d steady flow drag coefficient which should have been corrected with a wake amplification factor in order to represent the drag force in oscillatory flow. Since no extensive data is given for wake amplification for rectangular elements in DNV's recommended practices and the horizontal drag forces on the bottom structure are not crucial in this study, the approximation is found to be close enough. Hence, the oscillatory coefficient is taken as the steady flow coefficient. DNV recommends that the drag coefficient for oscillatory flow should not be less than 2,5 in absence of a CFD analysis [1]. The vertical drag coefficient is therefore, as it is for the ROV in Section 5.2.3, taken as 2,5.

Added Mass Coefficient Normal to Circular Members

The horizontal added mass coefficient for all the circular members have been calculated according to Table A-2 in the DNV-RP-H103 [1]. This table provides the analytical added mass coefficient for three-dimensional bodies in infinite

fluid. The added mass coefficient in the table can be found using interpolation, and it will approach a value of 1 as the element becomes more and more slender. The coefficient from the table relates the reference volume (ref Section 2.4.1) to the total added mass for the object. Orcaflex calculates added mass as a product of the added mass coefficient and the mass of the submerged volume, which means that the added mass for the object must first be calculated. The added mass is then divided by the "hydrodynamic mass" to find the added mass coefficient input for Orcaflex (equation (114)). The reference volume for added mass normal to cylinders is equal to the volume of the cylinder and the above-mentioned operation is therefore not necessary for this specific estimation.
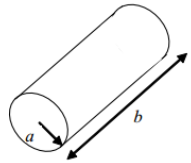
Table A-2 Analytical added mass coefficient for three-dimensional bodies in infinite fluid (far from boundaries). Added mass is $A_{ij}=\rho C_A V_R$ [kg] where V_R [m³] is reference volume (Continued)

Body shape		Direction of motion	C_A		V_R
			b/2a	C_A	
Right circular cylinder		Vertical	1.2 2.5 5.0 9.0 ∞	0.62 0.78 0.90 0.96 1.00	$\pi a^2 b$

Figure 5-15: Analytical added mass for circular cylinder [1].

$$C_a = \frac{A_{ij}}{\rho g V} \tag{114}$$

Vertical Added Mass for Suction Anchors

The vertical added mass for suction anchors can be divided into 3 parts: the reference mass above the anchor, the reference mass below the anchor and the mass of the trapped water inside the anchor. The added mass above and below the anchor is calculated based on the same principle as for the ROV. The added mass is a product of the added mass for a flat plate with the shape equal to the projected area and an adjustment factor based on the height of the object and the size of the projected area (Equation (95) & (96)). The projected area of the suction anchors is a circular flat plate. Table A-2 in DNV-RP-H103 provides the details for calculation of the added mass for flat plates [1].

Table A-2 Analytical added mass coefficient for three-dimensional bodies in infinite fluid (far from boundaries). Added mass is $A_{ij} = \rho C_A V_R$ [kg] where V_R [m³] is reference volume
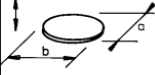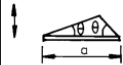
Body shape		Direction of motion	C_A				V_R
Flat plates	Circular disc	Vertical	$2/\pi$				$\frac{4}{3}\pi a^3$
	Elliptical disc	Vertical	b/a	C_A	b/a	C_A	$\frac{\pi}{6}a^2 b$
			∞	1.000	5.0	0.952	
			14.3	0.991	4.0	0.933	
			12.8	0.989	3.0	0.900	
			10.0	0.984	2.0	0.826	
			7.0	0.972	1.5	0.758	
			6.0	0.964	1.0	0.637	
	Rectangular plates	Vertical	b/a	C_A	b/a	C_A	$\frac{\pi}{4}a^2 b$
			1.00	0.579	3.17	0.840	
			1.25	0.642	4.00	0.872	
			1.50	0.690	5.00	0.897	
			1.59	0.704	6.25	0.917	
			2.00	0.757	8.00	0.934	
			2.50	0.801	10.00	0.947	
			3.00	0.830	∞	1.000	
	Triangular plates	Vertical	$\frac{1}{\pi}(\tan\theta)^{3/2}$				$\frac{a^3}{3}$

Figure 5-16: Analytical added mass for flat plates in infinite fluid.

The added mass due to trapped water inside the suction anchor is equal to the weight of the trapped water.
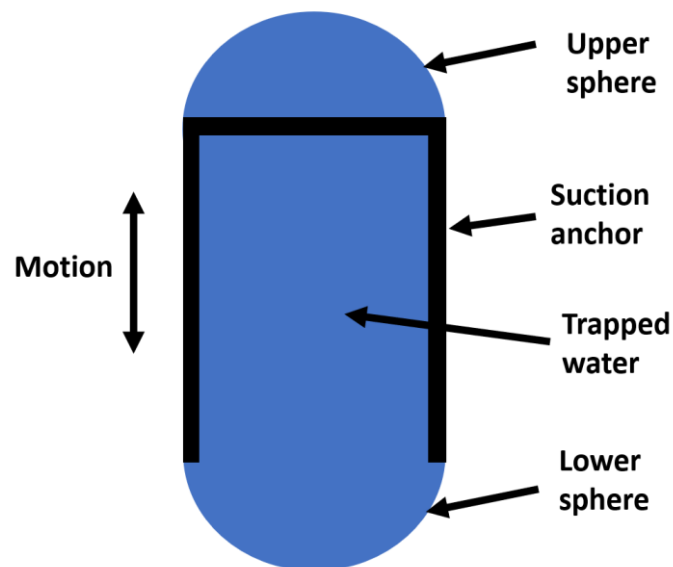
Figure 5-17: Added mass for suction anchor.

The added mass for the numerical model of the suction anchors has not been included in the 6d buoys which represents the suction anchor. It has been modeled as 3 separate line elements which are all connected to the master node. This

is to ensure that the wave kinematics at the correct depth is used. Using the wave kinematics at the free surface would be too conservative. The middle and the bottom line elements have a diameter and length of 1 m. Both the added mass and rate of change for added mass has been included as depth dependent coefficients such that the added mass will be activated when the roof of the suction anchor reaches the free surface. The top line element represents the added mass due to the water above the suction anchor, which do not contribute to the slamming force, and the rate of change is therefore not included for this element. The radius of the line element is equal to the distance from the suction anchor roof to the center of mass for upper sphere.
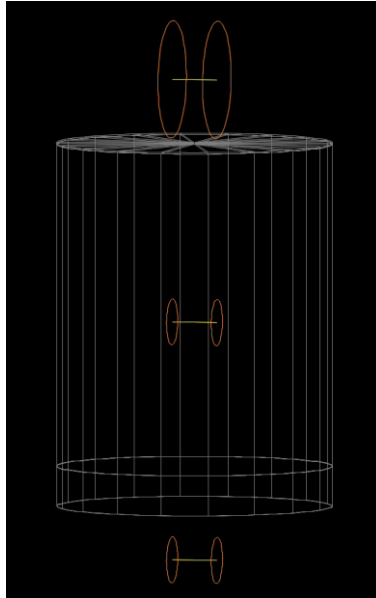
Figure 5-18: Suction anchor numerical model with line elements representing added mass.

The rate of change of the added mass is based on Figure 3-5 from DNV-RP-H103 [1]. This figure presents the high frequency limit of vertical added mass coefficient and its derivative as a function of water depth for horizontal cylinders. The horizontal axis shows the normalized submergence (depth divided by radius of cylinder).
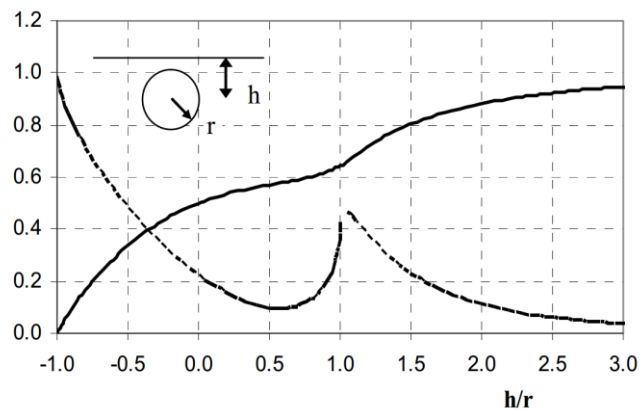
Figure 5-19: Vertical added mass coefficient and its derivative as a function of water depth [1].

The depth-dependent coefficients for the suction anchor are presented in Figure 5-20.
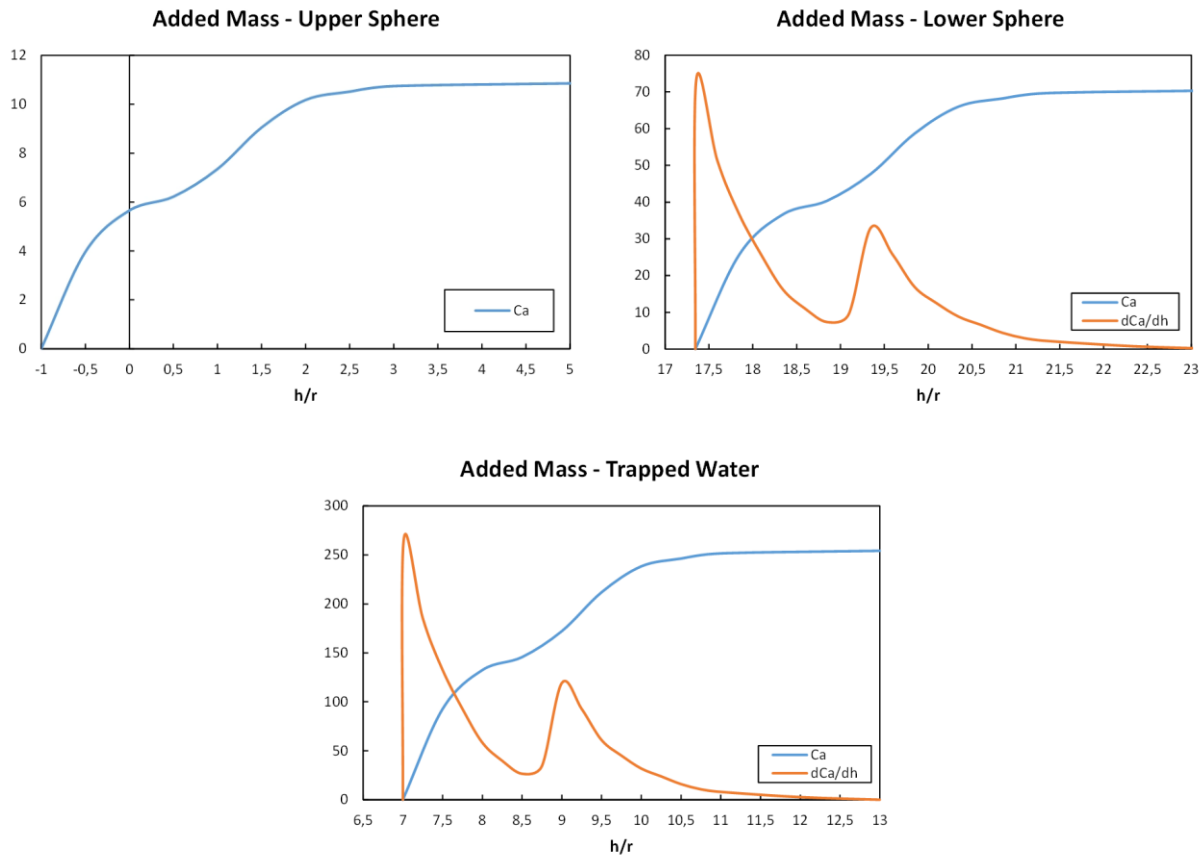
Figure 5-20: Depth-dependent added mass input for suction anchors.

Suction Anchor Numerical Model Input

The input for modelling of the 4 suction anchors are presented in Table 5-16 to

Table 5-18. As described above, the suction anchors are modeled as 6D Spar buoys with line elements representing the added mass properties. Each suction anchor has a dry weight of 30 t.

Table 5-16: Suction anchor hydrodynamic properties – 6d buoy.

	Normal	Axial
Drag area, $[m^2]$	47,40	0
Drag coefficient, $[-]$	0,67	0
Added mass coefficient, $[-]$	0,63	0
Inertia coefficient, $[-]$	1,63	0

Table 5-17: Suction anchor inertia properties – 6d buoy.

	X	Y	Z
Mass moment of inertia, $[m^2 t]$	290,0	290,0	270,0
Centre of mass, $[m]$	0	0	5,0

Table 5-18: Suction anchor added mass properties – Line elements.

	Upper sphere line element	Trapped water line element	Lower sphere line element
Added mass coefficient, $[-]$	Figure 5-20	Figure 5-20	Figure 5-20
Added mass rate of change, $[-]$	N/A	Figure 5-20	Figure 5-20
Outer diameter, $[m]$	2,55	1,0	1,0
Inner diameter, $[m]$	2,54	0,98	0,98
Vertical distance from bottom of suction anchor, $[m]$	9,18	4,0	-1,17

Tailpipe Numerical Model Input

The input for modeling of the 4 Tailpipes on the template is presented in Table 5-19 and Table 5-20 below. They are modeled with 6d spar buoys and have a dry weight of 3,1 t each. No added mass or drag is included for the vertical direction since the pipes are open ended.

Table 5-19: Tailpipe properties – 6d buoy.

	Value
Normal drag area, $[m^2]$	6,5
Normal drag coefficient, $[-]$	1,05
Normal added mass coefficient, $[-]$	0,92
Normal inertia coefficient, $[-]$	1,92

Table 5-20: Tailpipe inertia properties – 6d buoy.

	X	Y	Z
Mass moment of inertia, $[m^2 t]$	11,4	11,4	0,8
Centre of mass, $[m]$	0	0	4,0

Top Structure Numerical Model Input

The top structure consists of two types of pipes. They are modeled as line elements with each their line type. The two line types are presented in Table 5-21 to Table 5-22. Pipe 1 (the horizontal elements) have a total length of 62 m and a total dry weight of 27,8 t. Pipe 2 (the oblique elements) have a total length of 44 m and a weight of 11,1 t. Depth-dependent coefficients are considered as negligible for this part of the template.

Table 5-21: Pipe 1 properties – Line element-

	Value
Outer diameter, $[m]$	0,7
Inner diameter, $[m]$	0,646
Normal drag coefficient, $[-]$	1,03
Normal added mass coefficient, $[-]$	1,0
Normal inertia coefficient, $[-]$	2,0
Added mass rate of change normal to cylinder, $[-]$	N/A

Table 5-22: Pipe 2 properties – Line element.

	Value
Outer diameter, $[m]$	0,5
Inner diameter, $[m]$	0,47
Normal drag coefficient, $[-]$	0,97
Normal added mass coefficient, $[-]$	1,0
Normal inertia coefficient, $[-]$	2,0
Added mass rate of change normal to cylinder, $[-]$	N/A

Guidepost Numerical Model Input

The 16 guideposts are represented as 3d buoys, with only translational properties.

Table 5-23: Guidepost size properties – 3d buoy.

	Value
Mass, $[t]$	1,4
Volume, $[m^3]$	0,177
Height, $[m]$	0,97

Table 5-24: Guidepost hydrodynamic properties – 6d buoy.

	X	Y	Z
Drag area, $[m^2]$	1,4	1,4	0
Drag coefficient, $[-]$	0,97	0,97	0
Added mass coefficient, $[-]$	1,24	1,24	0

Bottom Structure Numerical Model Input

The bottom structure is modeled as 12 individual 3d buoys to ensure that the mass and hydrodynamic properties are distributed at the location of the actual frame instead of at the center of the template.

Table 5-25: Bottom structure buoys size properties – 3d buoy.

	Value
Mass, $[t]$	12,1
Volume, $[m^3]$	1,5
Height, $[m]$	1,0

Table 5-26: Bottom structure buoys hydrodynamic properties – 6d buoy.

	X	Y	Z
Drag area, $[m^2]$	1,0	1,0	14,0
Drag coefficient, $[-]$	1,5	1,5	2,5
Added mass coefficient, $[-]$	1,6	1,5	4,1

5.3.5   Environmental Conditions

The environmental conditions are similar to the conditions for the ROV vessel (ref. section 5.2.5), but the direction is changed to be 165 degrees. This is to capture the effect of shielding while also minimizing the roll motion of the vessel.
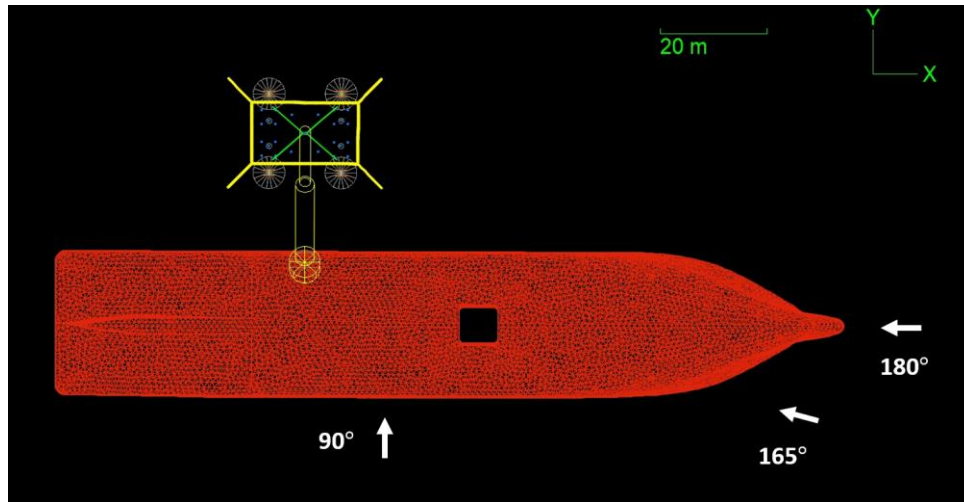
Figure 5-21: ITS deployment - Wave direction.

5.3.6   Shielding Effect

The shielding effect is captured by importing sea state RAO results from Orcawave to Orcaflex. The sea state RAO is amplitude operators which describes the disturbed wave velocity potential relative to the undisturbed wave velocity potential. Orcaflex uses this to calculate the new sea surface elevation, fluid velocity and acceleration in the disturbed sea state [22]. The vessel will serve as an obstruction for the waves approaching the ITS and therefore reduce the wave velocity potential.

5.3.7   Simulation Setup

The simulations are performed as Implicit time domains with the recommended constant time step [22]. The default time step of 0,1 seconds is kept, and the simulation time is set to be 128 seconds. The build-up time is set to be 65 seconds. The long build-up period is required to remove asymmetry in the loading that can appear in short build-up periods.

Table 5-27: Time domain simulation matrix – ROV deployment.

	RAO input	Shielding	Vessel motion	Wave direction [°]	T_z [s]
Simulation set 1	Upright	Yes	Coupled	165	2-13
Simulation set 2	Heeling	Yes	Coupled	165	2-13
Simulation set 3	Upright	Yes	Uncoupled	165	2-13
Simulation set 4	Upright – Increased Roll	Yes	Coupled	165	2-13

Chapter 6

Assessment of Allowable Sea States for ROV Deployment

6.1   Operational Criteria

The operational criteria are a set of criterions which, in conjunction with the time domain simulation results, will determine if the marine operation can be conducted. The operational criteria are compared to the extreme responses from the time domain simulation, which are determined by fitting a statistical model to the sample. The extreme values are directly related to the desired probability of exceedance. The desired probability of exceedance is normally in the range between 0,1 and 0,01 [8]. This number is related to the risk associated with the operation. Choosing a too high value will increase the uncertainty around whether this incident will happen or not. Combining a too low value with a small sample size (amount of seeds) may reduce the reliability of the predicted extremes. An exceedance probability of 0,05 is considered appropriate for the ROV Deployment operation. This exceedance probability is implemented in the investigation of three different extreme value criteria:

- Clashing between ROV and vessel hull
- Sea surface clearance underneath ROV when in "safe position"
- Maximum tension in umbilical

50 wave seeds are simulated for each sea state in order to create a proper statistical basis. Each sea state is assessed with regards to the operational criteria. The consequences of increasing or decreasing the number of wave seeds has been investigated by Amer [14].

6.1.1   Clashing Between ROV and Vessel Hull

Excessive pendulum motion can cause the ROV to collide with the stern of the vessel. The clearance between the vessel hull and the ROV is taken as the difference between the time history of the vessel x-coordinate and the time

history of the x-coordinates of the bottom corners on the ROV. The minimum clearance for each of the wave seeds are used to estimate the parameters in the probability model, before using this model to predict the extreme value with a 5% probability of exceedance. This value is compared to the criterion of minimum 0,1 m distance between the ROV and the vessel.
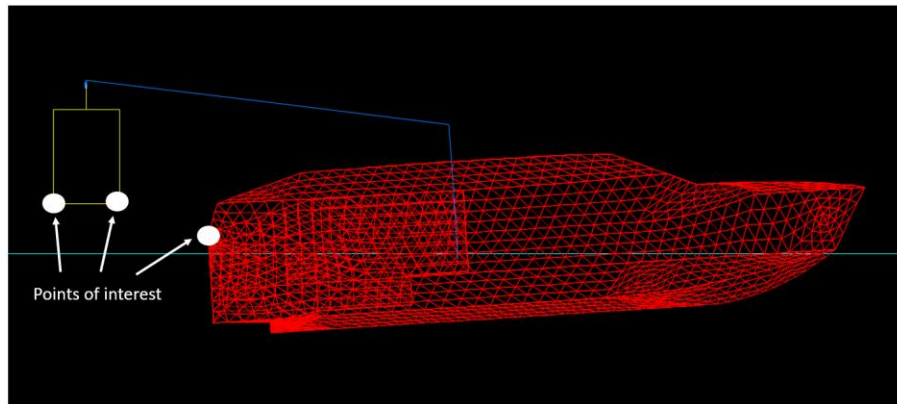
Figure 6-1: Points of interest for horizontal clearance check.

A time history graph of the x-coordinates for the vessel aft part and the four points of interest on the ROV is presented in Figure 6-2. The minimum clearance which is later used to estimate parameters for the probability model is located at 21,5 seconds and is reported to be 0,7 meters. This happens prior to deployment. For this particular case it can be seen from the crossing of the scatter plot for point 2 and point 3 that the ROV rotates almost 90 degrees before being deployed. It starts to rotate back during deployment. The graph also indicates a slight deviation between the x-coordinates for the two foremost points and between the two aftmost points. This is due to the simulation build-up period.
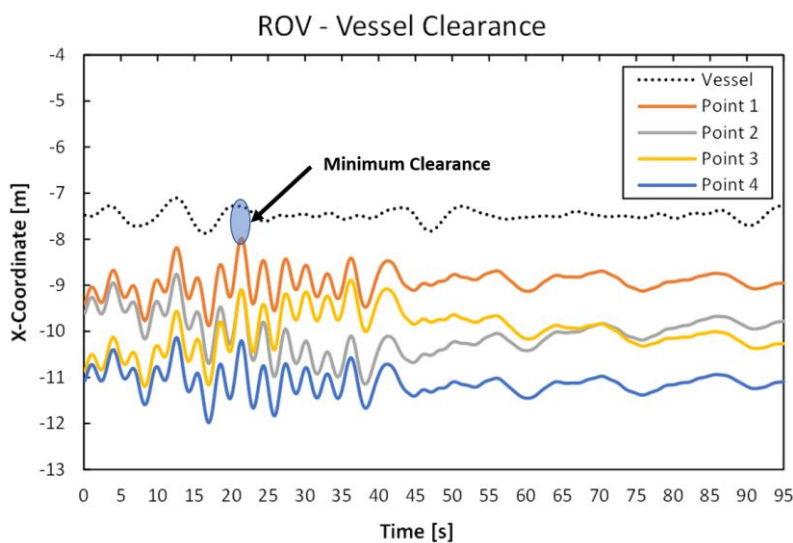
Figure 6-2: ROV and vessel X-coordinates (Hs = 0,75 m and Tz = 8 s).   Figure 6-3: Reported time history points.
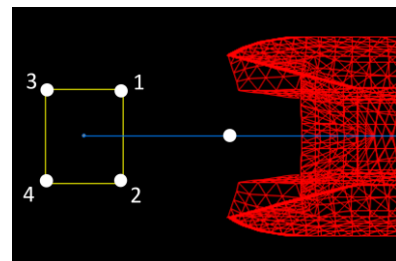
6.1.2   Sea Surface Clearance Underneath ROV When in "safe zone"

At the stage where the ROV is released from the latching system, and ready to be deployed, it shall be clear from the sea surface. This is to avoid inducing "unnecessary" forces to the launch and recovery system, specially the latching mechanism. A minimum clearance of 0,1 m to the sea surface is required during this stage. This criterion is compared to the minimum clearance results during simulation stage 1, prior to deployment (0 s – 30 s).
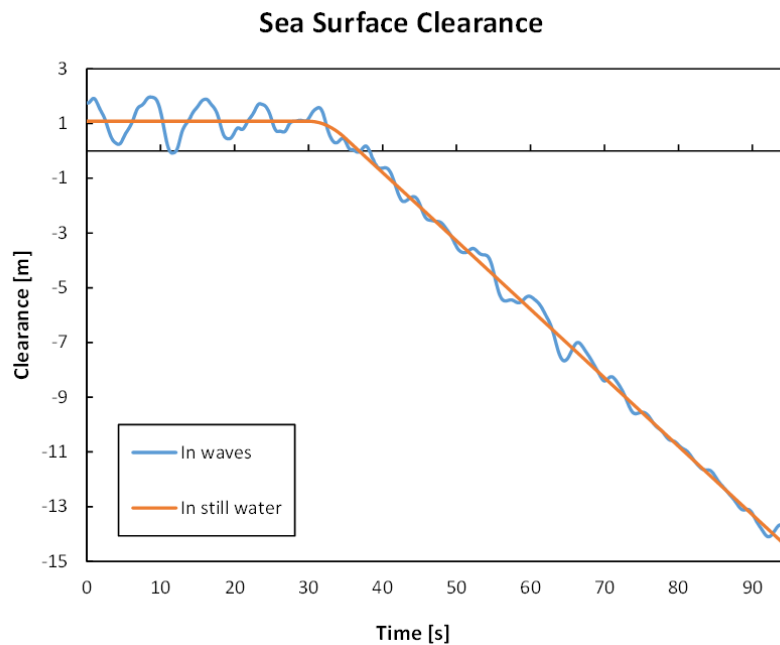
Figure 6-4: Sea surface clearance underneath ROV (Hs = 2,25 m and Tz = 8 s).

Figure 6-4 visualizes the sea surface clearance during the entire simulation period, which verifies that the mean value for the oscillating clearance in waves is close to the clearance in still water. The operational criterion is violated at approximately 12 seconds for this particular case.

6.1.3   Maximum Tension in Umbilical

The lifting wire tension, and subsequently the forces induced to the LARS, is considered one of the critical responses. During crossing of the splash zone, large slamming forces in the opposite direction of the gravity may occur. This contributes negatively to the relative motion between the crane tip and the lifted object and may induce large peak loads to the lifting wire. According to DNV-GL-RP-H103, a 10 % margin against slack lifting wire is required. This means that the minimum tension in the lifting wire shall be more than 10 % of the object's submerged weight [1]. This is not used as a criterion for this study since ROVs are equipped with a fair amount of buoyancy modules to decrease

the submerged weight. This makes the system so prone to slack sling incidents that it is considered unrealistic to set operational limitations based on this criterion.

The maximum tension in the umbilical shall be less than the maximum allowable load for the LARS and the maximum allowable load for the umbilical. The maximum allowable load of the LARS is taken as the safe working load times the design dynamic amplification factor for the system. The design dynamic amplification factor for this system is 3.0. The launch and recovery system is designed according to DNV's old lifting appliances standard [35].

$$\text{Lars allowable load} = SWL \cdot DAF = 29{,}43 \, kN \cdot 3 = 88{,}29 \, kN$$

According to DNVGL-ST-N001 the safety factor for the umbilical shall be taken as the maximum values of the two values in equation (115). Since the Umbilical is steel braided the largest calculated safety factor is 2,54.

$$\gamma_{sf} = max \left\{ \begin{matrix} \gamma_h \gamma_c \gamma_r \gamma_w \gamma_m \\ 2{,}3 \gamma_r \gamma_w \end{matrix} \right\} \tag{115}$$

$$\text{Umbilical allowable load} = \frac{MBL}{\gamma_{sf}} = \frac{300 \, kN}{2{,}54} = 118 \, kN$$

The capacity of the launch and recovery system is the governing criterion.
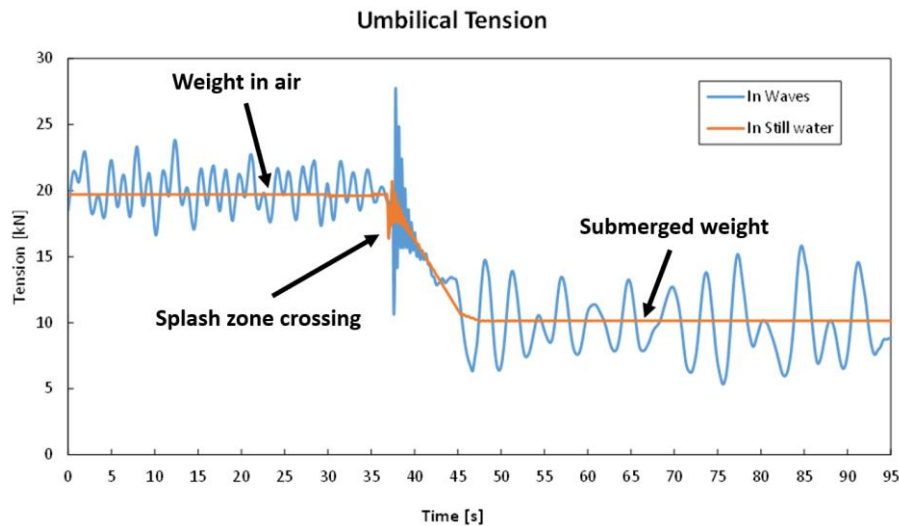
Figure 6-5: Time history of umbilical tension (Hs = 0,75 m and Tz = 6 s).

The effect of the slamming force during crossing of the splash zone where the sudden upward pointing force increases the amplitude of the oscillating tension, and thus increasing the maximum tension value, can be seen in Figure 6-5.

6.2   Fitting Probability Model

Each wave realization produces its own set of dynamic responses. This is due to the randomly generated phase angle, ϵ_n. This is further explained in Section 2.1.3, and Equation (38). The differences can be seen when comparing time history of a response for different realizations of the same sea state. Figure 6-6 is a time history graph of the tension in the umbilical/lifting wire during the full simulation period for two different realizations/seeds. Large deviation in maximum tension can be seen when studying the period where the ROV starts crossing the splash zone (between 35 s and 40 s). Equation (81) defines slamming as a function of the relative velocity between the lowered object and sea surface, since the added mass is infinitesimally at the instant of time when the object hits the sea surface.
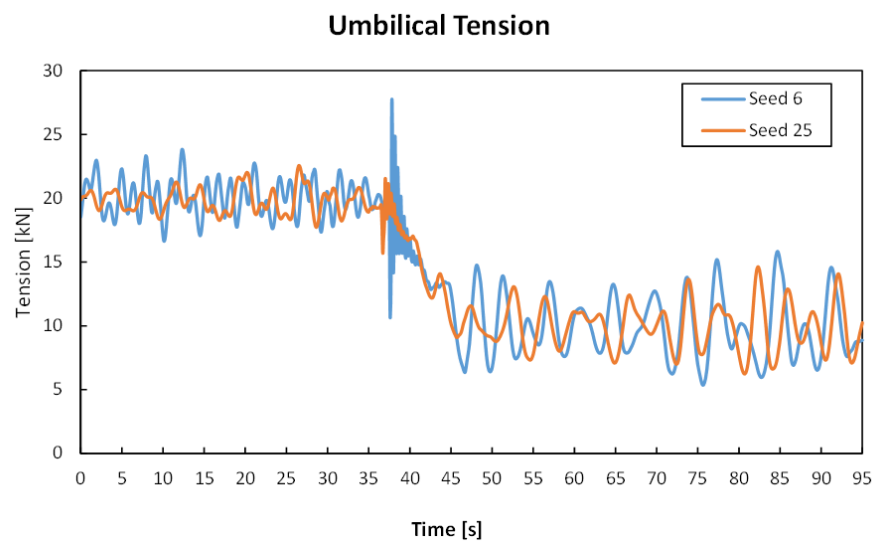
Figure 6-6: Umbilical tension for seed 6 and seed 25 (Hs = 0,75 m and Tz = 6 s).

Figure 6-7 is time history of the relative velocity in the period where the splash zone crossing happens. Positive velocity indicates that the ROV and sea surface is moving towards each other, while negative indicates that they are moving apart. The crossings in each seed happen approximately one second from each other because of the dynamic and randomized sea surface clearance. The relative velocity time history complies with the tension time history in Figure 6-6. The relative velocity when the ROV crosses the sea surface in wave seed 6 is significantly larger than the velocity during the sea surface crossing in wave seed 25, which induces significantly larger slamming forces.
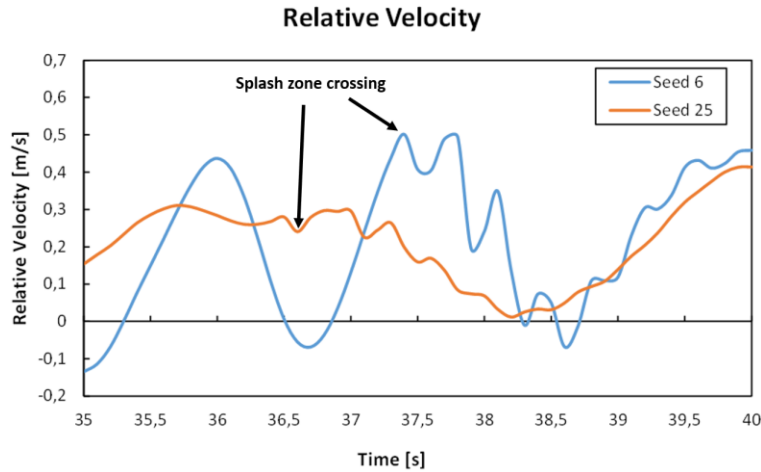
Figure 6-7: Relative velocity between ROV and sea surface during splash zone crossing (Hs = 0,75 m and Tz = 6 s).

The Gumbel distribution model usually provides a proper fitting for extreme values during lowering through splash zone [8]. As mentioned in Section 2.5, the Weibull probability model might also be a good fit for modeling extreme values. Probability papers for three arbitrary sea states (Hs = 0,75 m and Tz = 6 s to 8 s) are presented in Figure 6-8 - Figure 6-10. This has been plotted both to verify the use of the chosen probability model and to compare the Gumbel probability model with the 2-parameter Weibull probability model. The black lines in the figures are linear trendlines following each their mean zero up-crossing period. The goal with this exercise is to choose a probability model where the plotted sample follows a more or less straight line. The first two plots, Figure 6-8 and Figure 6-9, show that the maximum tension is better modeled with the Gumbel probability model than the Weibull probability model near the tails of the distribution. When estimating the extreme values, the precision at the tail in each end of the distribution is of particular interest.
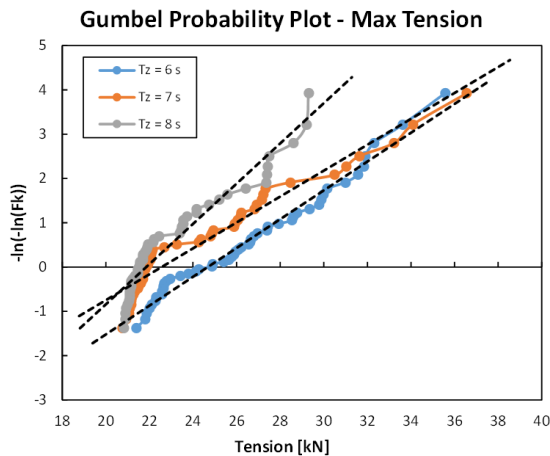
Figure 6-8: Gumbel probability plot for maximum tension (Hs = 0,75).
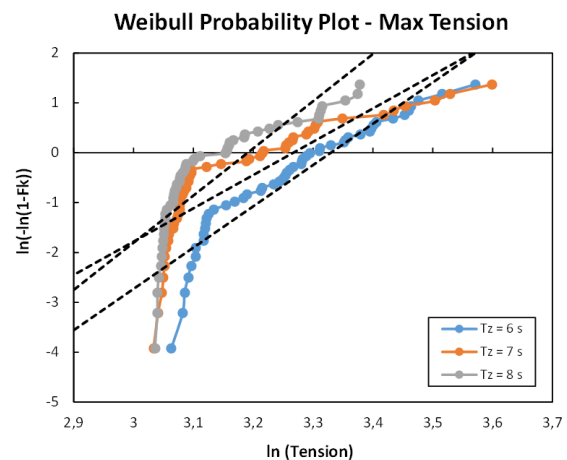
Figure 6-9: Weibull probability plot for maximum tension (Hs = 0,75).

Plotting the probability density functions for the same sample along with a histogram from the sample indicates that none of the distributions are completely wrong, but the Gumbel distribution fits the sample slightly better. This histogram displays the density of each range plotted with a total probability of 1.
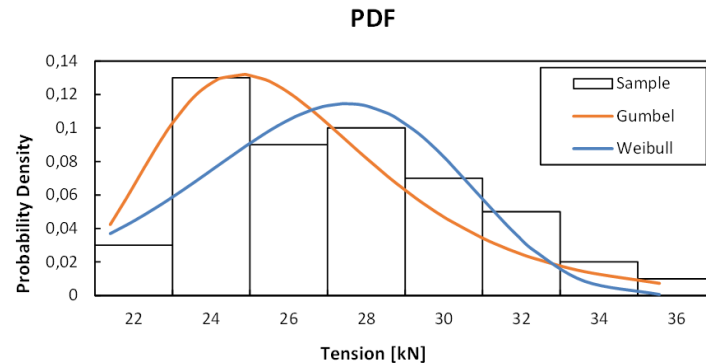
Figure 6-10: PDF fitting for maximum tension (Hs = 0,75 m and Tz = 6 s).

Figure 6-11 and Figure 6-12 indicates the both types of probability model suits the sea surface criterion well. Both distributions seem to follow a straight line, but with some discrepancies near the lower tail. Focusing on the lower tail for both distributions it can be seen that the minimum sample value for the mean zero up-crossing period of 6 seconds ends up on the right side of the trendline. Using the probability models for this mean zero up-crossing period could be a bit conservative. On the other hand, it can be seen that the minimum value for Tz = 8 seconds appears on the left side of the trendline. Using the probability model for this Tz may lead to overestimating the operational limits. Using a probability approach will never give a "perfect" answer.
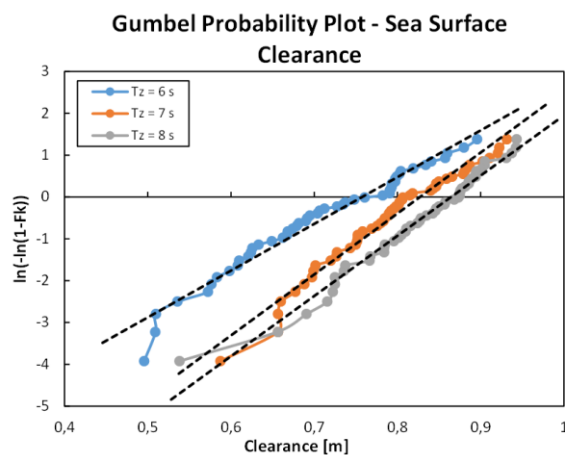
Figure 6-11: Gumbel probability plot for sea surface clearance (Hs = 0,75).
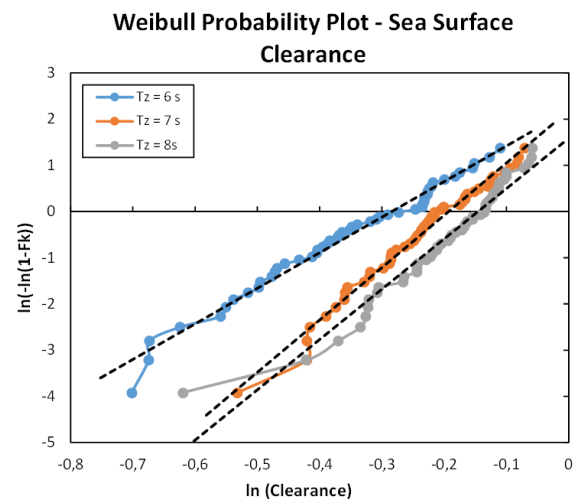
Figure 6-12: Weibull probability plot for sea surface clearance (Hs = 0,75).

The probability plots for the horizontal clearance between the ROV and the stern of the vessel, Figure 6-13 and Figure 6-14, seems to have a similar level of compatibility with the sample. Even though they seem similar, the discrepancies for the Weibull distribution are larger than directly observed in the graph. This is because the "x-values" are logarithmic values.
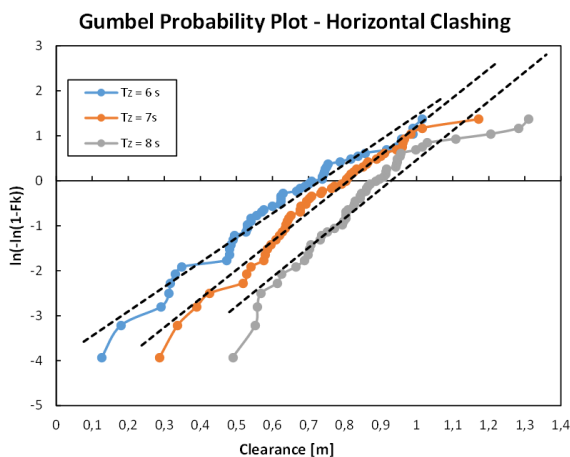
Figure 6-13: Gumbel probability plot for horizontal clashing (Hs = 0,75).
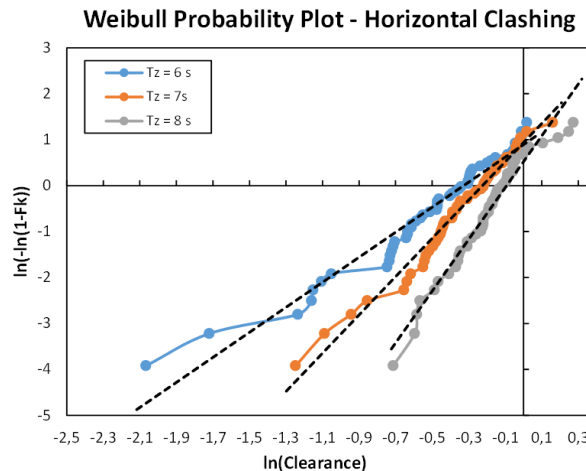
Figure 6-14: Weibull probability plot for horizontal clashing (Hs = 0,75).

The probability density function for both distributions, along with the histogram for the sample of Hs = 0,75 m and Tz = 6 s results, is presented in Figure 6-15. Both distributions correspond well with the histogram. It can be seen that the amount of simulations with minimum clearance between 0,85 m and 0,95 m is a bit lower than expected from the two distributions. There will always be a deviation between the obtained results and the expected results since the wave realizations are randomized.
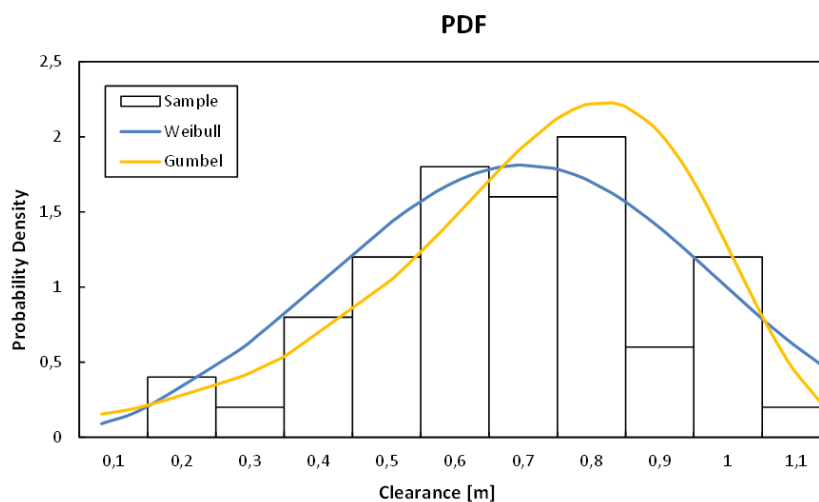
Figure 6-15: PDF fitting for horizontal clearance (Hs = 0,75 m and Tz = 6 s).

6.3   Even Keel Allowable Sea States

Results for both head waves and beam waves are presented and compared in this subchapter. The governing criterion is horizontal clashing for all analyzed sea states. The results for the two wave directions are very similar in terms of the allowable sea states due to this horizontal clashing criterion. The maximum umbilical tension and the sea surface clearance results are less severe for the beam waves. With the ROV being deployed at the stern of the vessel it is reasonable that the wave direction (head waves) that causes the largest pitch motions also causes the largest maximum umbilical tension and the lowest clearance to the sea surface.
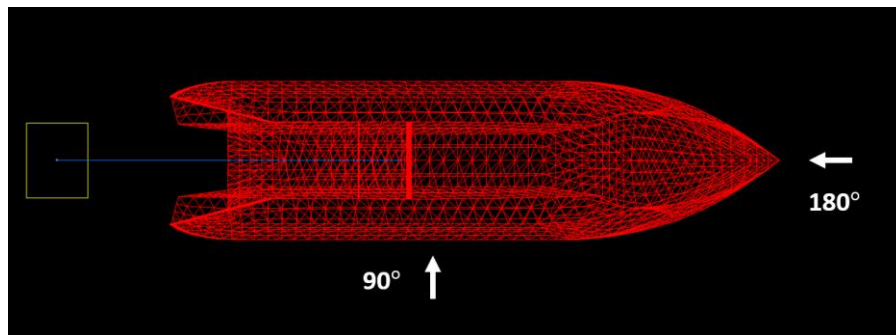
Figure 6-16: Wave directions.

The allowable sea state results for the ROV deployment in head sea and beam sea are presented in Figure 6-17 and Figure 6-18. The boxes marked green represent sea states where the operation can take place, while the orange boxes represent sea states where the probability to exceed one or more of the criteria is above 5%. The numbers marked with white are the values that violate the predefined criteria. The grey boxes are omitted sea states due to the braking wave criterion from DNV-RP-H103 [1]. The table for allowable sea states demonstrates a clear relation between decreasing wave period and increasing dynamic responses. This is covered in Section 2.1.3. There are several reasons why the responses are larger for smaller wave periods.

The pitch motion strongly influences the heave motion of the ROV. The heave motion for the ROV can be written as equation (116) [20], where z is the heave motion of the vessel. x_b and y_b is the longitudinal and transverse position of the point. θ and ϕ is the pitch and roll motion of the vessel. Since the ROV is located on the centerline, the pitch motion is the only rotational motion which influences the heave motion of the ROV. According to Figure 4-19 the natural period for pitch motion in head waves is around 3-4 seconds, making the system prone to pitch motions in the low range of spectral peak periods. The spectral peak period is according to DNV-RP-H103 [1] between 1,17 to 1,29 times the zero up-crossing period, depending on the spectral shape factor. The width of the wave spectrum is decided by the spectral shape parameter, which is a function of the significant wave height and the zero up-crossing period (Equation (32)). The wave spectrums are mostly wide for significant wave heights up to 3 meters. The width increases

when the zero up-crossing period increases, meaning that several short waves will be generated even for longer spectral peak periods.

The pendulum motion of the ROV is the governing criterion for the allowable sea states. The natural period for the pendulum motion of the ROV is given by Expression (117), where the initial length of the lifting wire is 0,6 m. This gives a natural period of 1,6 s. This value will increase slightly before the ROV hits the water.

$$z_p = z - x_b \theta + y_b \phi \tag{116}$$

$$T_0 = 2\pi \sqrt{\frac{L}{g}} \tag{117}$$

With regards to the tension criterion, the vertical water particle velocity increases when the wave period decreases. This can give higher slamming forces. This is given by Equation (118), which is a deep water simplification of linear wave theory. Combining this with the dispersion relation for deep water waves and setting z equal to zero gives the maximum velocity at the sea surface.

$$w = \frac{\xi_0 k g}{\omega} e^{kz} \cos(\omega t - kx) \tag{118}$$

$$w_{max} = \frac{2\pi\xi_0}{T} \tag{119}$$

| Allowable Sea State - No Trim - 180 deg | | | | | | | | | | | | | |
Tz / Hs	2	3	4	5	6	7	8	9	10	11	12	13	Criterion
0,5	60,2	64,9	38,4	33,0	29,3	25,9	24,2	24,2	23,4	22,5	22,3	21,9	Tension, [kN]
	0,64	0,49	0,61	0,69	0,73	0,77	0,83	0,87	0,90	0,94	0,96	0,97	Sea Surface Clearance, [m]
	-0,30	-0,47	0,02	0,26	0,50	0,70	0,78	0,80	0,98	1,02	1,27	1,21	Horizontal Clashing, [m]
0,75	71,9	125,9	63,8	42,8	33,0	31,7	27,7	25,4	24,9	22,7	22,6	22,4	Tension, [kN]
	0,32	0,15	0,38	0,43	0,52	0,64	0,68	0,78	0,80	0,86	0,90	0,93	Sea Surface Clearance, [m]
	-0,77	-0,71	-0,49	-0,06	0,24	0,39	0,53	0,64	0,73	0,80	0,91	0,91	Horizontal Clashing, [m]
1		194,4	109,1	60,7	40,1	34,7	34,5	29,6	27,5	26,0	24,2	23,2	Tension, [kN]
		-0,36	0,04	0,23	0,35	0,44	0,52	0,63	0,71	0,79	0,84	0,86	Sea Surface Clearance, [m]
		-1,08	-0,82	-0,38	0,02	0,19	0,34	0,46	0,54	0,68	0,75	0,77	Horizontal Clashing, [m]
1,25			141,2	104,3	49,6	38,7	39,4	31,8	28,6	28,6	25,9	25,9	Tension, [kN]
			-0,09	0,13	0,12	0,35	0,42	0,61	0,62	0,74	0,81	0,80	Sea Surface Clearance, [m]
			-0,99	-0,55	-0,29	0,08	0,06	0,32	0,47	0,43	0,56	0,72	Horizontal Clashing, [m]
1,5			164,7	129,1	74,2	60,8	40,1	35,5	31,5	27,4	27,0	26,1	Tension, [kN]
			-0,19	-0,13	0,08	0,14	0,34	0,44	0,56	0,65	0,68	0,77	Sea Surface Clearance, [m]
			-1,34	-1,02	-0,52	-0,44	0,02	0,13	0,16	0,39	0,43	0,52	Horizontal Clashing, [m]
1,75			174,4	159,0	93,9	63,9	42,4	36,7	37,2	31,9	27,7	27,7	Tension, [kN]
			-0,38	-0,29	-0,16	-0,03	0,18	0,31	0,51	0,59	0,64	0,71	Sea Surface Clearance, [m]
			-1,12	-0,87	-0,74	-0,49	-0,17	0,05	0,23	0,18	0,27	0,34	Horizontal Clashing, [m]
2			199,2	170,1	106,4	86,1	57,3	42,6	39,5	34,9	30,0	31,3	Tension, [kN]
			-0,53	-0,54	-0,44	-0,14	0,06	0,24	0,34	0,47	0,58	0,64	Sea Surface Clearance, [m]
			-1,17	-1,09	-0,95	-0,48	-0,30	-0,17	-0,07	0,15	0,15	0,23	Horizontal Clashing, [m]
2,25				166,2	146,9	86,4	56,8	52,1	41,8	36,9	32,7	29,6	Tension, [kN]
				-0,72	-0,52	-0,39	-0,03	0,11	0,24	0,43	0,47	0,55	Sea Surface Clearance, [m]
				-1,13	-0,91	-0,75	-0,53	-0,25	-0,21	-0,05	-0,05	0,17	Horizontal Clashing, [m]
2,5				202,1	168,0	119,9	88,7	47,8	40,3	32,3	33,3	31,6	Tension, [kN]
				-0,57	-0,67	-0,50	-0,17	0,06	0,17	0,31	0,39	0,54	Sea Surface Clearance, [m]
				-1,28	-1,10	-0,88	-0,70	-0,45	-0,16	-0,10	0,00	0,18	Horizontal Clashing, [m]
2,75				200,9	161,8	123,2	87,5	65,8	48,6	36,4	34,6	32,9	Tension, [kN]
				-0,64	-0,76	-0,61	-0,34	-0,04	0,05	0,24	0,35	0,50	Sea Surface Clearance, [m]
				-1,33	-1,34	-1,01	-0,74	-0,49	-0,47	-0,25	-0,12	0,05	Horizontal Clashing, [m]

Figure 6-17: Allowable sea state for even keel RAO in head sea with 0,05 exceedance probability.

The allowable sea states increase when the vessel operates in beam seas. This is because of the position of the launch and recovery system. As mentioned above, the heave motion of the ROV is related to the heave and pitch motion of the vessel. The pitch responses in beam sea is negligible, except for the waves not coming in from 90 degrees due to directional spreading (Section 2.1.3). When studying Figure 6-19 it can be seen that the pitch response in beam sea is generally lower than the pitch response in head sea, but still influential. This can be explained by looking at the pitch RAO data for both 180 degrees and 135 degrees. The pitch response in 135 degrees waves is almost as large as the pitch response in 180 degrees waves. It can be concluded that the directional spread is the reason why the vessel is experiencing this much pitch motion in beam sea. Running the simulation without spreading would increase the difference between the amplitude of the two time history graphs. The difference in responses are less significant for the horizontal clearance. This is because the vertical offset of the lifting point induces horizontal motion in transversal direction when the vessel experience roll motion. This effect does also occur for pitch motion in longitudinal direction. Even though the critical motion is the longitudinal motion and the major motion in this case is transversal, the minimum values becomes almost as low as for head waves. The directional spreading contributes to create a circular motion of pendulum, which causes the low minima values.

Tz \ Hs	2	3	4	5	6	7	8	9	10	11	12	13	Criteria
Allowable Sea State - No Trim - 90 deg													
0,5	51,3	55,9	41,7	29,5	27,1	23,8	24,6	22,9	22,5	22,1	22,0	21,6	Tension, [kN]
	0,65	0,71	0,78	0,77	0,79	0,83	0,87	0,90	0,94	0,96	0,98	0,99	Sea Surface Clearance, [m]
	-0,33	-0,49	0,10	0,40	0,53	0,78	0,84	0,91	1,01	1,07	1,31	1,14	Horizontal Clashing, [m]
0,75	71,0	94,5	48,1	39,4	29,7	28,2	24,4	24,5	24,5	23,2	22,7	21,7	Tension, [kN]
	0,37	0,52	0,64	0,60	0,67	0,75	0,76	0,82	0,87	0,91	0,93	0,96	Sea Surface Clearance, [m]
	-0,92	-0,77	-0,35	0,05	0,40	0,50	0,61	0,80	0,82	0,89	1,06	0,99	Horizontal Clashing, [m]
1		114,4	75,2	51,3	39,6	32,3	27,9	26,3	25,4	23,9	23,8	23,0	Tension, [kN]
		0,24	0,47	0,48	0,48	0,51	0,69	0,77	0,83	0,84	0,87	0,90	Sea Surface Clearance, [m]
		-0,93	-0,52	-0,31	0,03	0,23	0,44	0,50	0,60	0,78	0,89	0,89	Horizontal Clashing, [m]
1,25			97,9	63,4	45,1	35,1	33,4	30,9	27,5	26,1	25,4	22,9	Tension, [kN]
			0,33	0,37	0,35	0,53	0,60	0,67	0,75	0,78	0,81	0,88	Sea Surface Clearance, [m]
			-0,74	-0,56	-0,20	0,04	0,17	0,37	0,58	0,63	0,74	0,87	Horizontal Clashing, [m]
1,5			114,6	79,1	49,4	41,5	39,9	32,3	29,8	26,3	24,5	25,6	Tension, [kN]
			0,14	0,15	0,20	0,34	0,48	0,53	0,64	0,71	0,77	0,79	Sea Surface Clearance, [m]
			-0,82	-0,61	-0,37	0,01	0,14	0,24	0,44	0,49	0,62	0,76	Horizontal Clashing, [m]
1,75			130,2	91,7	65,7	44,5	40,7	33,7	31,9	30,1	26,7	26,2	Tension, [kN]
			-0,11	0,03	0,01	0,21	0,38	0,49	0,58	0,67	0,71	0,81	Sea Surface Clearance, [m]
			-1,00	-0,81	-0,50	-0,39	0,04	0,13	0,32	0,44	0,52	0,55	Horizontal Clashing, [m]
2			142,9	105,6	81,6	49,9	38,8	36,8	33,6	30,0	28,4	27,2	Tension, [kN]
			-0,12	-0,25	-0,03	0,14	0,29	0,45	0,51	0,57	0,67	0,75	Sea Surface Clearance, [m]
			-0,93	-0,86	-0,68	-0,56	-0,29	-0,01	0,15	0,30	0,48	0,49	Horizontal Clashing, [m]
2,25				110,9	101,0	69,2	46,8	39,9	36,7	32,7	31,0	28,1	Tension, [kN]
				-0,20	-0,22	-0,01	0,17	0,30	0,41	0,51	0,64	0,68	Sea Surface Clearance, [m]
				-0,99	-0,77	-0,54	-0,34	-0,16	0,07	0,18	0,32	0,47	Horizontal Clashing, [m]
2,5				131,3	94,8	67,8	62,2	38,6	39,6	34,8	29,9	30,8	Tension, [kN]
				-0,34	-0,39	-0,13	0,00	0,17	0,39	0,50	0,55	0,65	Sea Surface Clearance, [m]
				-1,03	-0,92	-0,75	-0,58	-0,31	-0,04	0,20	0,24	0,29	Horizontal Clashing, [m]
2,75				142,1	120,9	92,2	52,1	48,0	40,3	33,4	30,9	34,0	Tension, [kN]
				-0,60	-0,62	-0,23	-0,02	0,17	0,28	0,42	0,54	0,58	Sea Surface Clearance, [m]
				-1,12	-1,04	-0,91	-0,59	-0,48	-0,08	0,07	0,23	0,20	Horizontal Clashing, [m]
3				152,2	118,7	97,9	78,2	51,2	43,0	35,3	34,7	36,9	Tension, [kN]
				-0,70	-0,92	-0,44	-0,22	0,02	0,15	0,35	0,40	0,53	Sea Surface Clearance, [m]
				-1,33	-1,34	-1,01	-0,74	-0,49	-0,47	-0,25	-0,12	0,05	Horizontal Clashing, [m]

Figure 6-18: Allowable sea state for even keel RAO in beam sea with 0,05 exceedance probability.
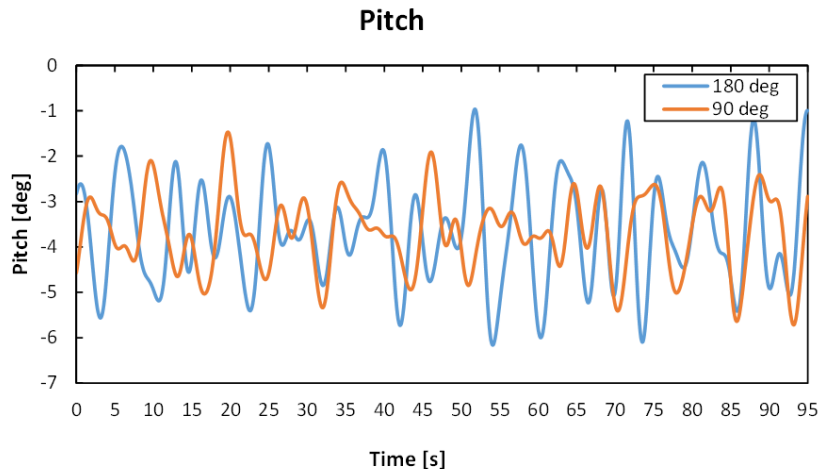
Figure 6-19: Comparison of time history of pitch motion for beam sea and head sea (Hs = 1,5 m and Tz = 9 s).

Even though motions like surge, sway and yaw are normally controlled by the vessels dynamic positioning system, and not very interesting for lifting operations, including them in the analysis will affect the results. The maximum tension and the sea surface clearance will not be very affected by the horizontal motions, but the horizontal clearance can be.
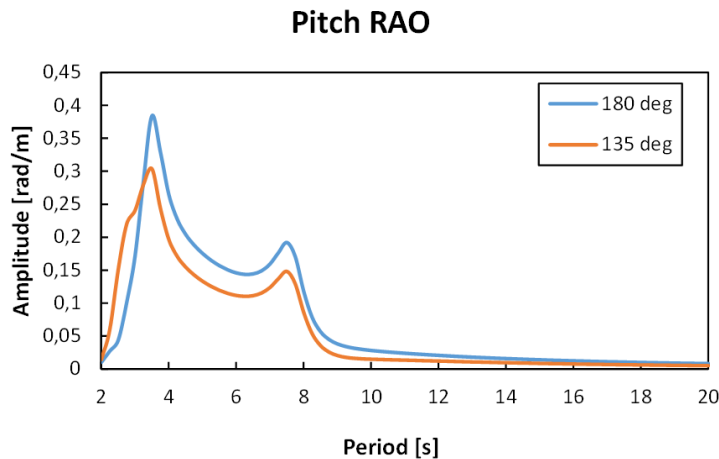
Figure 6-20: Pitch RAO for 180 deg. waves and 135 deg. waves.

As mentioned above, the difference in tension and sea surface clearance is larger than the difference in horizontal movement. This can be seen in Figure 6-21, where the area underneath the graph contains the allowable sea states. The gap between the two plots with the horizontal clearance criterion omitted is clearly bigger than the gap between the two plots for overall allowable sea state (The allowable sea state graph for the tension criterion and the sea surface clearance criterion only ranges from 4 s to 10 s zero up-crossing period).
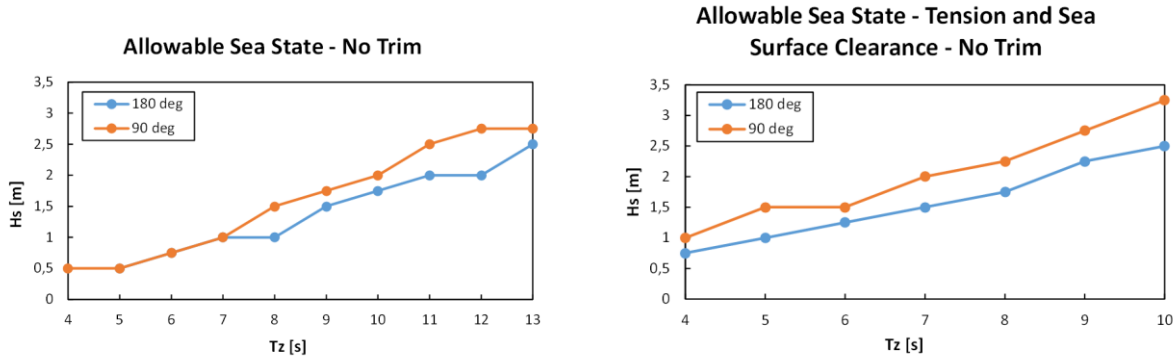
Figure 6-21: Allowable sea state comparison between beam sea and head sea for even keel RAO.

6.4 Trimmed Dynamic Responses

The allowable sea state results for the trimmed RAO simulations follows the same pattern as the allowable sea state results for the even keel RAO. This is expected since the simulation setup is identical except for the vessel RAO. It can be seen in Section 4.1.4 that the shape of the two compared sets of response amplitude operators resemble each other. Some minor discrepancies in the results are to be expected as the basis for the results are probability, based on a sample created using randomized variables. The horizontal pendulum motion is the governing criterion when using the altered RAO. This is similar for both cases. Some extra discrepancies may also be expected for the case of snap loads. Snap loads can be difficult to model numerically since a very small time-step could be necessary to capture the snapping incident. If the time-step is to large, then the maximum load due to the snapping incident could potentially "pass through the filter" without being noticed.

Allowable Sea State - Trimmed - 180 deg													
Tz / Hs	2	3	4	5	6	7	8	9	10	11	12	13	Criteria
0,5	55,5	56,8	41,3	33,0	28,8	26,5	24,6	23,3	23,4	22,5	22,2	21,9	Tension, [kN]
	0,60	0,45	0,56	0,60	0,75	0,78	0,84	0,88	0,93	0,95	0,97	0,99	Sea Surface Clearance, [m]
	-0,03	-0,46	0,16	0,36	0,50	0,63	0,71	0,92	1,05	1,17	1,38	1,26	Horizontal Clashing, [m]
0,75	68,2	128,3	64,9	43,9	38,0	30,6	27,8	25,5	25,0	23,8	24,1	22,7	Tension, [kN]
	0,35	-0,04	0,34	0,45	0,49	0,64	0,74	0,79	0,85	0,88	0,90	0,94	Sea Surface Clearance, [m]
	-0,17	-0,82	-0,47	-0,04	0,07	0,29	0,57	0,62	0,67	0,95	1,14	1,04	Horizontal Clashing, [m]
1		191,8	105,1	63,2	43,2	36,6	32,7	26,7	26,7	26,0	25,0	23,8	Tension, [kN]
		-0,43	0,05	0,23	0,31	0,42	0,59	0,67	0,76	0,82	0,85	0,88	Sea Surface Clearance, [m]
		-1,12	-0,81	-0,31	-0,11	0,17	0,34	0,49	0,58	0,60	0,84	0,82	Horizontal Clashing, [m]
1,25			152,9	87,3	55,6	40,9	36,9	30,8	28,3	26,9	27,6	25,7	Tension, [kN]
			-0,15	-0,02	0,17	0,32	0,51	0,58	0,66	0,75	0,80	0,83	Sea Surface Clearance, [m]
			-0,81	-0,69	-0,38	-0,03	0,09	0,25	0,45	0,48	0,71	0,56	Horizontal Clashing, [m]
1,5			182,3	130,6	79,7	46,8	44,6	34,7	31,0	29,2	27,9	26,7	Tension, [kN]
			-0,25	-0,16	-0,05	0,14	0,39	0,53	0,56	0,65	0,72	0,76	Sea Surface Clearance, [m]
			-1,17	-0,92	-0,52	-0,30	-0,02	0,15	0,23	0,36	0,40	0,49	Horizontal Clashing, [m]
1,75			212,5	160,2	101,6	71,9	47,9	36,7	33,8	33,1	29,2	28,3	Tension, [kN]
			-0,53	-0,48	-0,28	0,05	0,22	0,34	0,41	0,57	0,68	0,70	Sea Surface Clearance, [m]
			-1,08	-1,03	-0,78	-0,37	-0,26	0,05	0,06	0,17	0,31	0,39	Horizontal Clashing, [m]
2			220,0	172,5	118,3	75,0	54,0	42,2	34,9	32,5	30,8	29,0	Tension, [kN]
			-0,56	-0,70	-0,47	-0,08	0,05	0,14	0,43	0,54	0,57	0,72	Sea Surface Clearance, [m]
			-1,26	-1,05	-0,90	-0,49	-0,40	-0,19	0,06	0,17	0,22	0,32	Horizontal Clashing, [m]
2,25				184,9	132,3	98,6	64,9	45,5	39,4	34,4	31,5	28,5	Tension, [kN]
				-0,99	-0,59	-0,31	-0,07	0,13	0,31	0,47	0,54	0,63	Sea Surface Clearance, [m]
				-1,09	-0,93	-0,70	-0,54	-0,46	-0,21	0,03	0,00	0,23	Horizontal Clashing, [m]
2,5				209,1	172,1	115,4	80,6	62,7	42,1	35,2	36,0	32,2	Tension, [kN]
				-0,94	-0,61	-0,64	-0,19	-0,06	0,25	0,34	0,49	0,57	Sea Surface Clearance, [m]
				-1,23	-1,21	-0,84	-0,65	-0,39	-0,26	-0,06	-0,11	0,07	Horizontal Clashing, [m]

Figure 6-22: Allowable sea state for trimmed RAO in head sea with 0,05 exceedance probability.

The gap between allowable sea states for the two wave directions, for the even keel vessel condition, at shorter wave periods is not present for the analyses conducted with the vessel in trimmed condition. The gap for longer wave periods is, however, still present. The allowable sea states were lower in head sea than in beam sea for the simulations conducted with the vessel in even keel condition. Since the pitch motion in beam sea has increased for the vessel in trimmed condition, due to variation in draught along the length of the vessel (further explained in Figure 4-24), the horizontal motion of the ROV for beam sea will now be as large as it is for head sea. The allowable sea states will therefore be the for shorter wave periods (Figure 6-24). The increased peak in pitch RAO for shorter wave periods can be seen in Figure 4-21.

Tz / Hs	2	3	4	5	6	7	8	9	10	11	12	13	Criteria
Allowable Sea State - Trimmed - 90 deg													
0,5	50,3	60,4	48,6	33,6	27,8	26,9	23,3	23,1	22,1	22,2	21,9	21,8	Tension, [kN]
	0,67	0,66	0,70	0,78	0,81	0,84	0,90	0,94	0,95	0,97	0,99	1,01	Sea Surface Clearance, [m]
	-0,38	-0,67	-0,27	0,31	0,59	0,70	0,80	0,87	0,99	1,14	1,38	1,16	Horizontal Clashing, [m]
0,75	68,4	104,0	61,4	39,6	33,7	29,2	28,4	24,8	23,7	22,1	22,4	21,9	Tension, [kN]
	0,42	0,46	0,59	0,59	0,69	0,69	0,79	0,85	0,89	0,91	0,95	0,97	Sea Surface Clearance, [m]
	-1,05	-0,77	-0,44	-0,06	0,24	0,57	0,51	0,73	0,79	0,88	1,17	0,96	Horizontal Clashing, [m]
1		142,8	98,6	58,2	46,6	36,1	31,5	27,2	25,7	24,8	23,3	22,8	Tension, [kN]
		0,15	0,44	0,44	0,54	0,57	0,75	0,73	0,85	0,87	0,90	0,93	Sea Surface Clearance, [m]
		-1,05	-0,71	-0,65	-0,05	0,18	0,37	0,48	0,60	0,73	0,93	0,82	Horizontal Clashing, [m]
1,25			106,1	78,6	51,0	40,7	32,6	31,4	27,5	24,2	25,3	23,7	Tension, [kN]
			0,33	0,25	0,38	0,50	0,62	0,70	0,75	0,83	0,85	0,88	Sea Surface Clearance, [m]
			-0,80	-0,59	-0,45	-0,04	0,08	0,36	0,50	0,56	0,77	0,77	Horizontal Clashing, [m]
1,5			124,8	82,7	65,5	49,4	42,4	32,9	29,6	28,5	24,8	28,5	Tension, [kN]
			0,20	0,15	0,26	0,36	0,45	0,65	0,69	0,74	0,79	0,85	Sea Surface Clearance, [m]
			-0,86	-0,77	-0,53	-0,31	-0,07	0,21	0,32	0,56	0,60	0,62	Horizontal Clashing, [m]
1,75			145,0	105,9	78,2	54,5	47,9	36,6	34,3	27,0	27,4	29,3	Tension, [kN]
			-0,02	-0,02	0,18	0,31	0,45	0,54	0,65	0,71	0,73	0,83	Sea Surface Clearance, [m]
			-1,05	-1,03	-0,62	-0,38	-0,22	0,06	0,26	0,42	0,35	0,53	Horizontal Clashing, [m]
2			149,4	117,8	84,5	59,8	46,8	41,7	35,0	30,1	28,9	29,7	Tension, [kN]
			-0,13	-0,25	-0,10	0,19	0,38	0,55	0,58	0,63	0,67	0,79	Sea Surface Clearance, [m]
			-1,08	-1,13	-0,90	-0,58	-0,43	-0,14	-0,08	0,34	0,41	0,42	Horizontal Clashing, [m]
2,25				110,9	101,0	69,2	46,8	39,9	36,7	32,7	31,0	28,1	Tension, [kN]
				-0,20	-0,22	-0,01	0,17	0,30	0,41	0,51	0,64	0,68	Sea Surface Clearance, [m]
				-1,16	-0,96	-0,67	-0,48	-0,20	-0,03	0,14	0,38	0,31	Horizontal Clashing, [m]
2,5				131,3	94,8	67,8	62,2	38,6	39,6	34,8	29,9	30,8	Tension, [kN]
				-0,34	-0,39	-0,13	0,00	0,17	0,39	0,50	0,55	0,65	Sea Surface Clearance, [m]
				-1,49	-1,15	-0,90	-0,66	-0,34	-0,22	0,13	0,22	0,25	Horizontal Clashing, [m]
2,75				162,2	129,9	107,3	66,6	53,0	42,8	33,5	32,0	39,6	Tension, [kN]
				-0,59	-0,44	-0,17	0,01	0,25	0,33	0,43	0,55	0,69	Sea Surface Clearance, [m]
				-1,03	-1,25	-0,84	-0,76	-0,49	-0,26	-0,10	0,02	0,13	Horizontal Clashing, [m]
3				167,1	120,7	106,5	80,2	65,8	47,3	33,9	33,5	42,0	Tension, [kN]
				-0,96	-0,66	-0,41	0,02	0,05	0,28	0,39	0,50	0,63	Sea Surface Clearance, [m]
				-1,27	-1,47	-1,25	-0,91	-0,80	-0,42	-0,27	-0,12	-0,09	Horizontal Clashing, [m]

Figure 6-23: Allowable sea state for trimmed RAO in beam sea with 0,05 exceedance probability.

The allowable sea states for launching of the ROV in head waves will only reduce slightly when running the simulations with a set of trimmed response amplitude operators. It can be seen on the overall allowable sea state graphs in Figure 6-24 that the gap between the two wave directions is still there, but it is smaller. The biggest difference in the allowable sea states can be seen between 7 seconds and 10 seconds for the beam waves. Comparing the responses in beam waves for the RAO data calculated at even keel and the RAO data calculated at 3,66 degrees trimming angle, it can be seen that yaw motion is increased for the same wave periods. Figure 4-21 shows that the vessel experiences more pitch motion in beam waves when it is trimmed. This contributes directly to the horizontal motion that causes clashing between the ROV and the vessel. Along with a decreased roll motion before 8 seconds (Figure 4-20), the RAO graph for pitch and yaw responses (Figure 4-21) can explain why the horizontal movement of the ROV has increased.
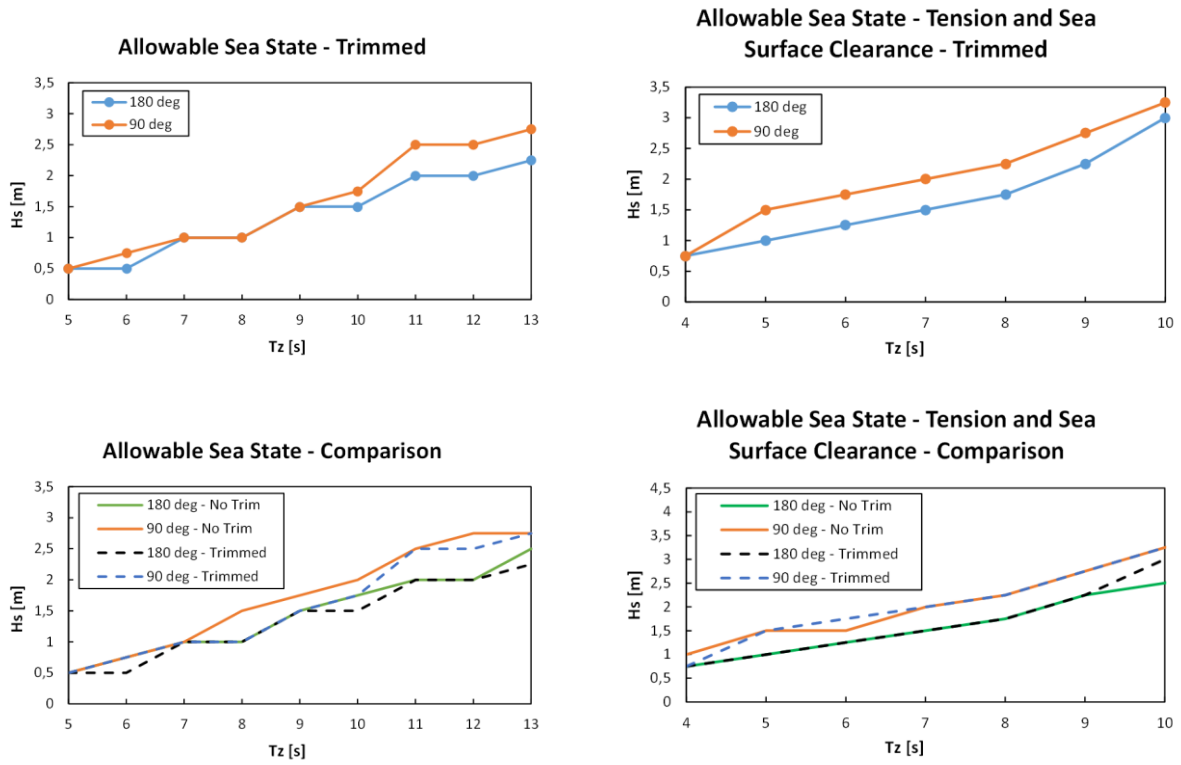
Figure 6-24: Allowable sea state for trimmed condition RAO compared with allowable sea states for even keel RAO.

Chapter 7

Assessment of Allowable Sea States for ITS Deployment

7.1 Operational Criteria

The splash zone crossing of the ITS is governed by two criteria. The maximum dynamic hook load (DHL) shall not exceed the capacity of the crane, and neither of the four lifting slings between the hook and the ITS shall never become slack. There is no defined maximum sling load limit for the lifting slings. These will normally be designed based on information from the time domain simulations. Each sea state is simulated 50 times with different wave seeds for each to achieve statistical confidence for the maximum and minimum sling forces. Maximum values are based on a 95% probability of non-exceedance. The minimum values are estimated using the same probability of non-exceedance as the maximum values. A comparison between the dynamic hook load in waves and the dynamic hook load in still water can be seen in Figure 7-1. The figure shows that oscillating forces can cause high maximum loads. These oscillating forces are induced by the slamming loads which occurs when the suction anchors cross the splash zone (less relative velocity between the lifted object and the sea surface is present for the simulation in still water). The "Lifting Sling Tension" graph in Figure 7-1 is presented to illustrate that each of the 4 lifting slings experience fluctuating loads, just like the main lifting wire.
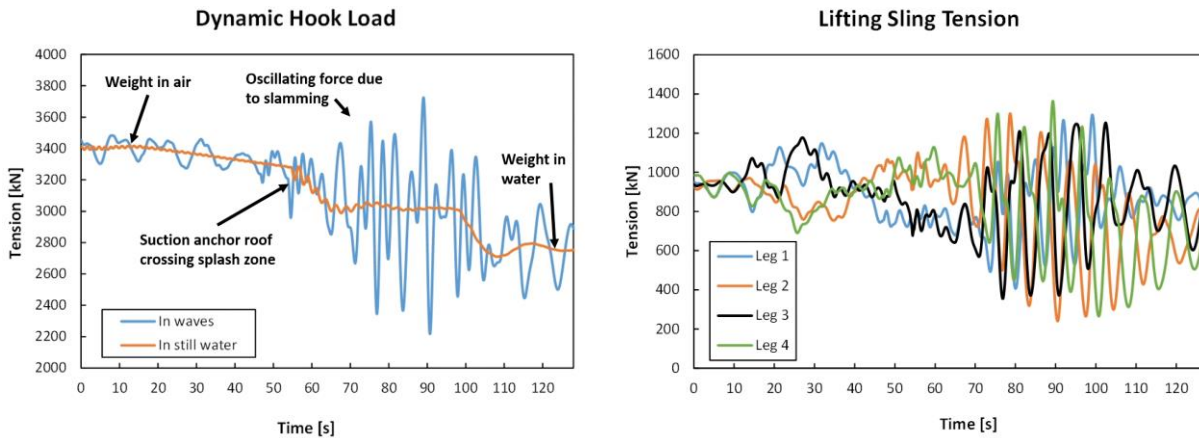
Figure 7-1: Time history of DHL and sling tension (Hs = 2,5 m and Tz = 7 s).

7.1.1　Minimum Load Criterion

According to DNV's recommended practice for modeling and analysis of marine operations [1], slack slings shall as far as possible be avoided. Equation (120) shall be fulfilled to have a sufficient margin against snap forces due to slack sling. The submerged weight of the template corresponds to a mass of 270 Te. Combining this with the 10 % margin against slack sling gives that the minimum dynamic hook load, reported from the time domain simulations, shall not be below 27 Te. The tension in each of the lifting slings when taking 60 degrees sling angles into account shall always be above 7,8 Te.

$$F_{hyd} \leq 0,9 \cdot F_{static-min} \tag{120}$$
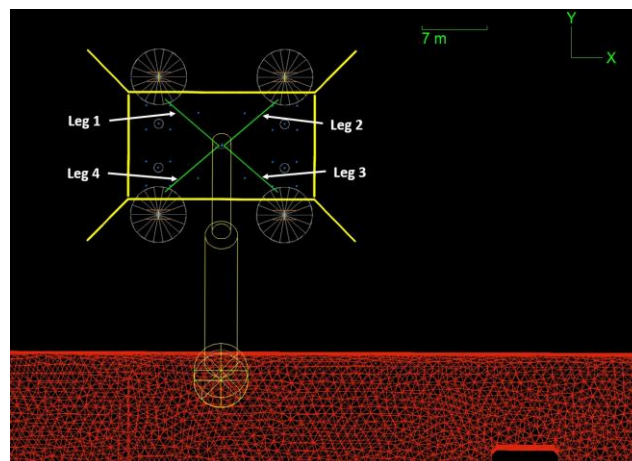
Figure 7-2: Lifting slings for ITS deployment.

7.1.2 **Maximum Load Criterion**

As mentioned above, the maximum DHL shall not exceed the dynamic capacity of the crane. It is, however, considered acceptable that dynamic peak loads exceed the SWL of the crane. The main crane on the ITS deployment vessel has a DHL capacity of 420 Te at a radius of 24,5 meter. A higher dynamic capacity could have been achieved by reducing the working radius on the crane. This radius is chosen because it coincides with the constrains for the overboarding phase. Alternatively, the radius could be reduced after finishing the slewing motion, but this increases the free hanging time of the ITS. It could be further discussed which of the two alternatives is the most favorable, but this study is limited to the splash zone crossing part of the installation and the radius of 24,5 m is therefore kept.

7.2 **Fitting Probability Model**

Like the extracted data from the time domain simulations of the ROV deployment, the maximum and minimum tension values from the ITS deployment simulation needs to be fitted to a probability model. The same technique, using a probability paper to see if the values follows a pattern, have been utilized for the ITS deployment case. A comparison of the time history of the DHL between two different wave seeds of the same sea state has been presented in Figure 7-3 to visualize the difference between wave realization with the same environmental properties. The peak load due to slamming forces in the splash zone exceeds the maximum DHL criterion for seed 42, while the maximum dynamic load in seed 27 is almost the same as the maximum static load. The same relation between the relative object – sea surface velocity, as presented in Figure 6-7, and the dynamic forces in the lifting wire is applicable for the deployment of the ITS.
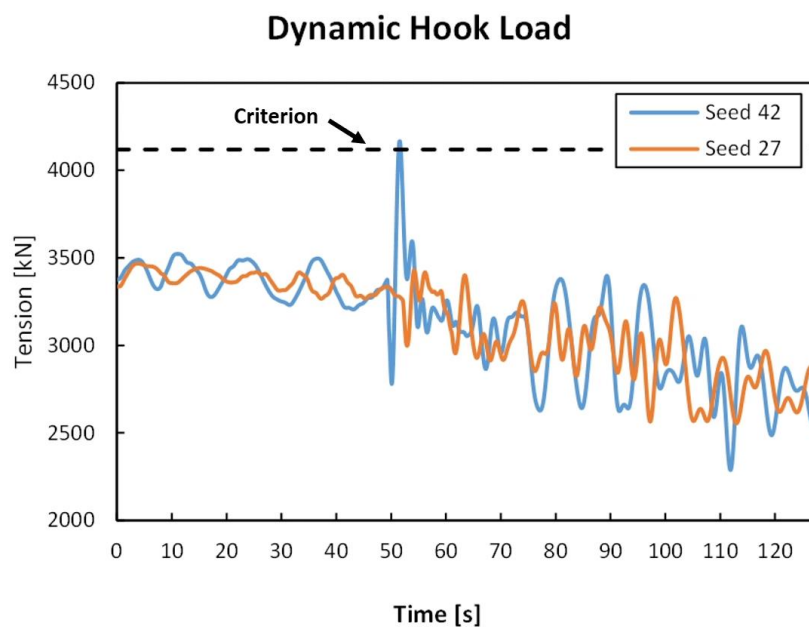
Figure 7-3: Dynamic hook load for seed 27 and seed 42 (Hs = 3,5 m and Tz = 9 s).

Figure 7-4 shows that a Gumbel maximum probability model is a more suitable model than the Weibull probability model. The sample values are closer to following a straight line for the Gumbel plot. This trend is also present for other sea states than the displayed sea state with significant wave height of 4,25 meters. A yellow dashed line is added to the Gumbel probability plot to represent the criterion of a non-exceedance probability of 95%. The intersection between this line and the trendlines gives the tension value for respective zero up-crossing period. It can be seen that the Gumbel probability model is non-conservative if the fractile were to be increased. The linear trendline is located on the left side of the maximum points for both 9 second and 10 second mean zero up-crossing periods. The maximum dynamic load criterion will be violated in waves with significant wave height of 4,25 meters and mean zero up-crossing period of 8 seconds according to Figure 7-4.
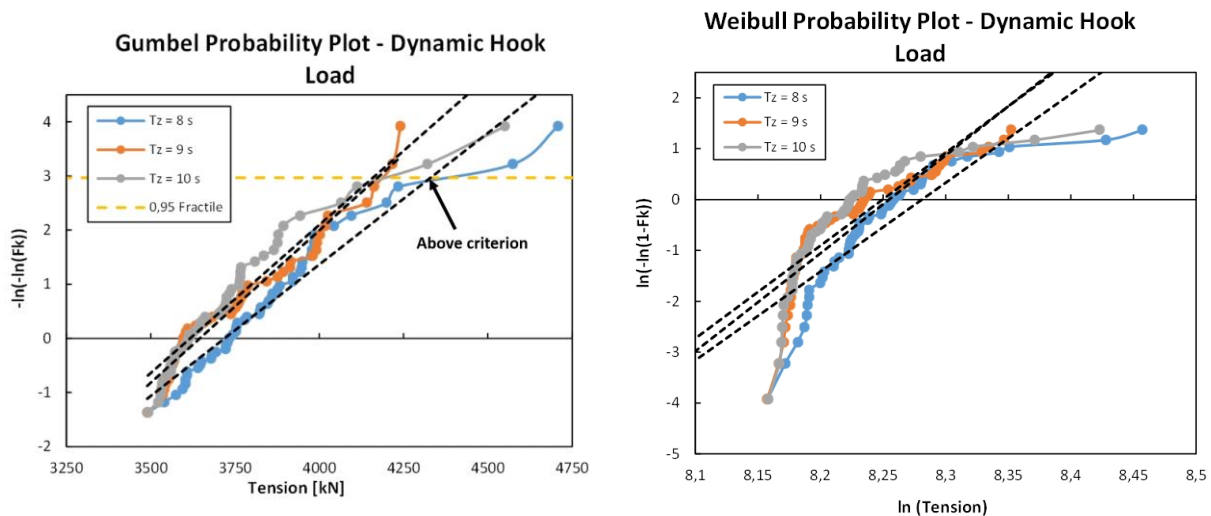
Figure 7-4: Probability plot for DHL (Hs = 4,25 m).

When plotting the probability papers for the minimum tension in the lifting slings, the Weibull model seems to fit better than for the maximum dynamic hook load. It is important to keep in mind that the x-values in the Weibull probability paper is the logarithm of the tension and not the tension itself. This can make the plot look more suitable than it is. The Gumbel minimum distribution also provides a sufficient modeling of the extreme values for the minimum tension in the lifting slings. Probability plots of both models for the tension in lifting sling number 2 is presented in Figure 7-5. Sling number 2 is the sling experiencing the most severe dynamic loads. This is further discussed in subchapter 7.3. The dashed yellow line, representing the 0,05 fractile, crosses the trendline for mean zero up-crossing period of 8 seconds at a value below the allowable minimum sling tension. This is the same sea state that violates the maximum dynamic hook load criterion. It can also be seen that 9 seconds and 10 seconds mean zero up-crossing periods has a tension value above the minimum allowable tension.
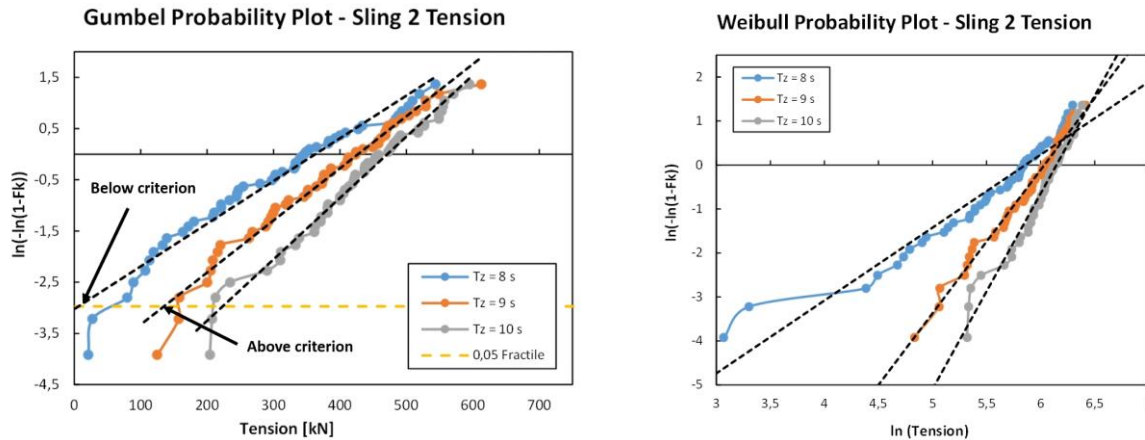
Figure 7-5: Probability plot for tension in Sling 2 (Hs = 4,25 m).

Based on the probability paper plots for the various time domain simulation results, the Gumbel probability model is chosen to model the extreme values for both maximum and minimum tension with regards to ITS deployment in this study.

7.3   Upright Dynamic Responses

A selection of results for allowable sea states are presented in Figure 7-9, with the responses exceeding its respective criterion marked with white. Like the ROV deployment results in Section 6 the allowable significant wave height for the ITS deployment increases when the mean zero up-crossing period increases. This relation is expected to be a result of lower wave kinematics with increasing wave period and that the vessel will "follow the waves" more for longer waves. Equation (119) in section 6.3 shows the relationship between wave period and maximum vertical fluid particle velocity, where an increasing wave period results in a decreasing maximum vertical fluid particle velocity. Looking at the heave RAO graph in Figure 4-22 it can be seen that for longer wave periods the heave response amplitude of the vessel tends to equal the wave amplitude. One meter wave amplitude equals one meter response amplitude.

A clear relation between the slamming force, acting on the suction anchors, and the dynamic hook load can be seen in Figure 7-6 and Figure 7-7. The maximum peak load occurs 2 seconds after the slamming force acts on suction anchor number 2. The timing of the slamming load acting on suction anchor number 2 is not necessarily the same as the other 3 suction anchors, as their roofs most likely do not hit the free surface at the exact same instant of time. The magnitude of the total slamming force is slightly higher since this graph only shows the slamming force due to the trapped water inside the suction anchor. The sphere underneath the suction anchor (further explained in section 5.3.3) is not included in the graph, but it occurs at the same instant of time. Depending on the timing of the crane tip motion and the motion of the template after slamming, the maximum dynamic hook load will happen at a certain time after the slamming load.
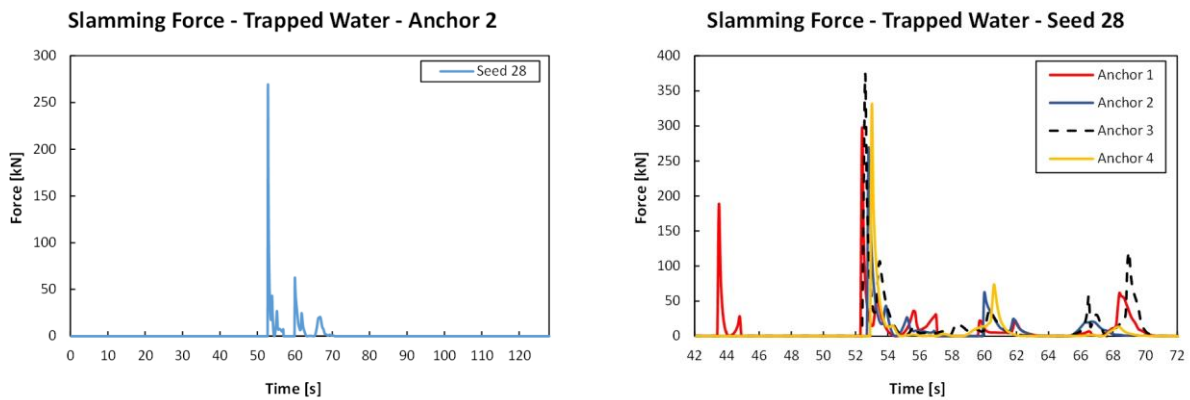
Figure 7-6: Slamming force for seed 28 (Hs = 3,5 m and Tz = 7 s).
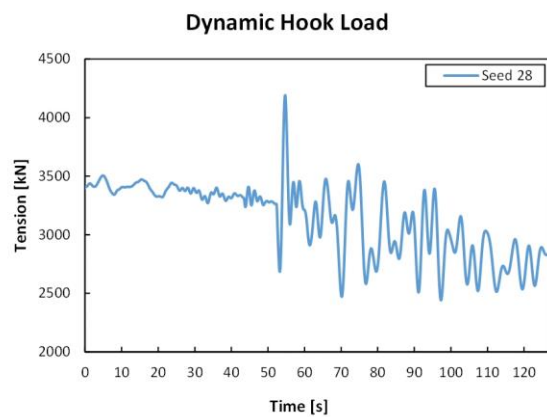
Figure 7-7: Dynamic hook load for seed 28 (Hs = 3,5 m and Tz = 7 s).

The effect of shielding can also be spotted in Figure 7-9. Sling leg number 2 is more prone to becoming slack than the other three slings. The suction anchor connected to the same corner as sling number 2 is the suction anchor which experiences the highest wave kinematics. This can be seen by comparing Figure 7-2 and the shielding results, which are presented as contour plots in Figure 4-27. Low sea state RAOs means lower vertical fluid particle velocity at that given point. This will again result in lower slamming loads and therefore bigger margin against slack.

Allowable Sea State
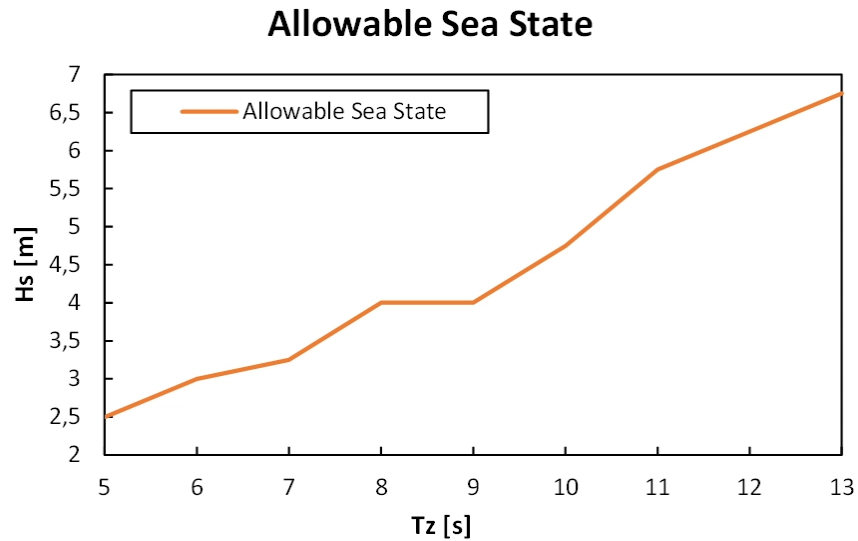
Figure 7-8: Allowable sea states for ITS deployment – Upright RAO.

The allowable sea states in Figure 7-8 is presented as a graph where the area underneath the line represents the combinations of significant wave heights and mean zero up-crossing periods where the template is allowed to be lowered through the splash zone. The allowable sea state results must not be mistaken to be the limit for the entire installation operation. This study only focuses on lowering the ITS through the splash zone. Normally a marine operation can be divided into multiple phases with separate allowable sea states for each part of the operation [5], but for a short operation like overboarding and lowering the template through the splash zone it is unrealistic to have multiple allowable sea states. Judging by the results from Amer's study on overboarding of a subsea template [14] it is not unlikely that the allowable sea states will be somewhat lower if the overboarding phase of the operation is also covered in the analysis. The supplier of this ITS has also set an upper installation limit of 2,5 meter significant wave height. This is the upper limit where the supplier is confident that their design is sufficiently strong to handle the loads occurring during the installation phase. This is overlooked in this study, but it gives an indication of which environmental conditions that are normally accepted for such operations. The experience of the offshore personnel conducting the operation is the final barrier prior to starting the operation. If they are not comfortable to execute the operation in the present conditions, the operation will not commence.

Tz / Hs	7	8	9	10	11	12	13	Criteria
5,25	4830,9	4567,5	4240,6	4041,6	3916,5	3835,6	3718,9	Max DHL
	1575,6	1819,3	1966,8	1992,8	2226,2	2181,3	2273,0	Min DHL
	77,4	54,7	227,1	238,3	368,5	408,2	415,6	Min Tension - Leg 1
	0	0	32,6	126,3	223,7	317,0	324,2	Min Tension - Leg 2
	7,1	19,6	168,2	199,5	311,6	397,0	371,1	Min Tension - Leg 3
	0	0	91,1	144,8	285,1	371,6	358,1	Min Tension - Leg 4
5,5	4771,0	4539,0	4711,3	4288,6	3928,8	3859,0	3827,1	Max DHL
	1471,8	1769,1	1973,4	2053,2	2134,0	2218,2	2222,2	Min DHL
	75,5	57,0	166,8	196,1	273,9	310,1	389,4	Min Tension - Leg 1
	0	0	55,1	97,3	107,0	300,0	302,9	Min Tension - Leg 2
	0	3,8	130,5	156,5	228,1	294,6	355,4	Min Tension - Leg 3
	0	0	123,4	139,3	130,0	351,4	391,1	Min Tension - Leg 4
5,75	5095,3	4826,1	4456,2	4376,2	4108,9	3967,9	3769,5	Max DHL
	1393,7	1648,5	1839,4	1995,9	2004,9	2161,6	2212,1	Min DHL
	0	0	87,5	234,7	238,9	308,0	376,0	Min Tension - Leg 1
	0	0	0	69,3	146,9	283,2	255,0	Min Tension - Leg 2
	0	0	52,1	200,8	182,4	342,4	364,7	Min Tension - Leg 3
	0	0	13,4	88,8	214,6	308,3	325,1	Min Tension - Leg 4
6	5537,8	4992,5	4764,9	4282,7	4246,2	3965,7	3994,9	Max DHL
	1120,9	1573,1	1733,2	1960,3	1983,4	2144,7	2143,9	Min DHL
	0	0	100,5	228,6	202,2	286,7	302,0	Min Tension - Leg 1
	0	0	0	54,0	115,9	205,1	260,7	Min Tension - Leg 2
	0	0	21,6	179,1	185,6	271,0	305,3	Min Tension - Leg 3
	0	0	60,9	90,5	177,9	295,4	304,8	Min Tension - Leg 4
6,25		4969,6	4641,0	4401,6	4202,7	4080,2	3986,6	Max DHL
		1440,2	1755,1	1892,1	1975,4	2088,6	2083,2	Min DHL
		0	91,6	170,1	204,4	210,5	313,4	Min Tension - Leg 1
		0	0	0	105,0	182,7	234,7	Min Tension - Leg 2
		0	72,5	104,2	191,7	192,7	277,9	Min Tension - Leg 3
		0	20,5	17,3	145,4	235,1	329,7	Min Tension - Leg 4
6,5		4987,5	4793,1	4534,9	4278,3	4113,8	3988,5	Max DHL
		1545,5	1777,4	1826,2	1979,6	2047,9	2152,6	Min DHL
		0	15,8	119,6	112,1	243,2	285,8	Min Tension - Leg 1
		0	0	26,7	112,2	131,6	291,3	Min Tension - Leg 2
		0	0	120,1	130,4	227,0	330,1	Min Tension - Leg 3
		0	0	50,1	161,2	187,8	360,0	Min Tension - Leg 4
6,75		5102,7	4779,4	4591,4	4314,3	4132,3	4100,0	Max DHL
		1513,6	1595,4	1729,5	1963,9	2011,2	2108,8	Min DHL
		0	0	35,7	91,2	283,8	188,0	Min Tension - Leg 1
		0	0	0	71,8	194,4	162,7	Min Tension - Leg 2
		0	0	0	116,1	265,2	207,0	Min Tension - Leg 3
		0	0	0	123,8	221,4	231,7	Min Tension - Leg 4
7		5919,8	5022,7	4641,9	4583,0	4146,1	4122,4	Max DHL
		1234,7	1697,0	1819,0	1767,3	1982,9	2029,6	Min DHL
		0	0	43,5	112,0	121,3	248,7	Min Tension - Leg 1
		0	0	0	48,9	182,6	133,6	Min Tension - Leg 2
		0	0	32,1	71,6	106,8	233,7	Min Tension - Leg 3
		0	0	0	134,4	239,7	139,2	Min Tension - Leg 4

Figure 7-9: Selection of allowable sea states for upright RAO with 0,05 exceedance probability.

7.4 Heeling Dynamic Responses

Running the simulations with RAO data obtained at a 3 degrees heeling angle gives results in the same area of magnitude as the results from the model with RAO data obtained from upright position. The allowable sea state comparison is presented as a graph in Figure 7-10. The two graphs follow each other up until 9 meters significant wave height, where the simulation setup using RAO data from 3 degrees heeling angle gives lower allowable sea states. The small deviations in the lower region of zero up-crossing periods are partly because of a slightly different vessel response, but mainly discrepancies due to the statistical approach. The allowable sea states at 5 seconds mean zero up-crossing period, with regards to the operational criteria in this thesis, will for both set of RAO data be the same as the ITS supplier's limit of 2,5 meters significant wave height.
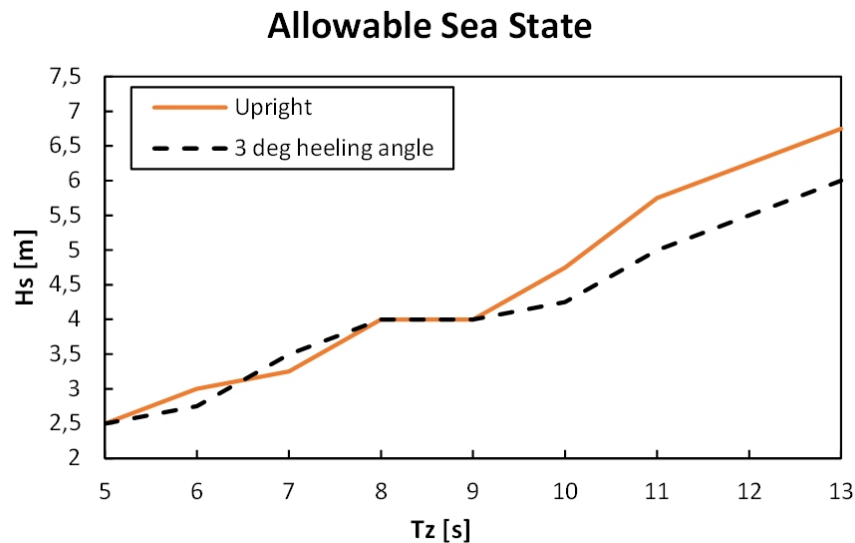
Figure 7-10: Comparison of allowable sea states for ITS deployment with different set of RAO data.

The same relation between the shielding effect and the slack lifting sling criterion can be seen for these simulations as for the simulations using RAO data for upright position. This is highlighted in Figure 7-11 for a significant wave height of 2,5 meters. The values have been found using the minimum Gumbel distribution with a non-exceedance probability of 0,95. The results corresponds well with the shielding results from the hydrodynamic analysis, as sling number two is attached to the suction anchor which experiences the highest wave kinematics.
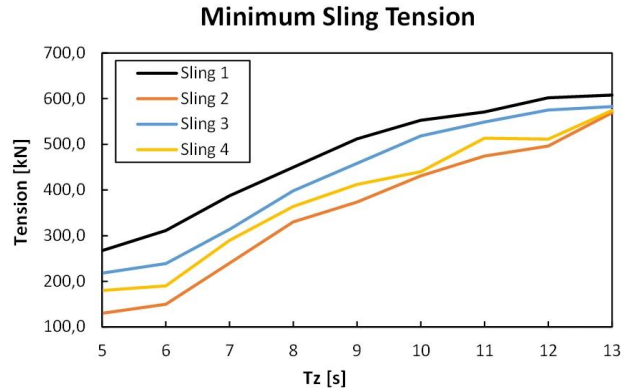
Figure 7-11: ITS deployment - Minimum sling tension for Hs = 2,5 m.

Looking at the Heave RAO of the crane tip motion in Figure 7-12 it can be seen that the RAO data for the heeling vessel condition induces larger heave motions at the crane tip from 9 to 13 seconds. This is due to the increased roll response seen in Figure 4-22. The same effect can be seen if the Heave RAO for the crane tip in head waves were plotted and compared. Figure 7-12 corresponds well with the results from the assessment of the allowable sea states seen in Figure 7-10. The heave RAO at the crane tip for both vessel conditions follow each other up to the point of 9 seconds, and the same can be seen for the allowable sea states. The crane tip of the vessel described with RAO data obtained at 3 degrees heeling angle will after this point have larger responses in heave direction than the crane tip of the vessel described with RAO data obtained in upright position. This results in lower allowable sea states for the vessel described with RAO data obtained at 3 degrees heeling angle. There is a direct relation between the relative displacement between the lifted object and the crane tip. This and the effect of relative displacement between the crane tip and the sea surface is further explained in Section 7.5.
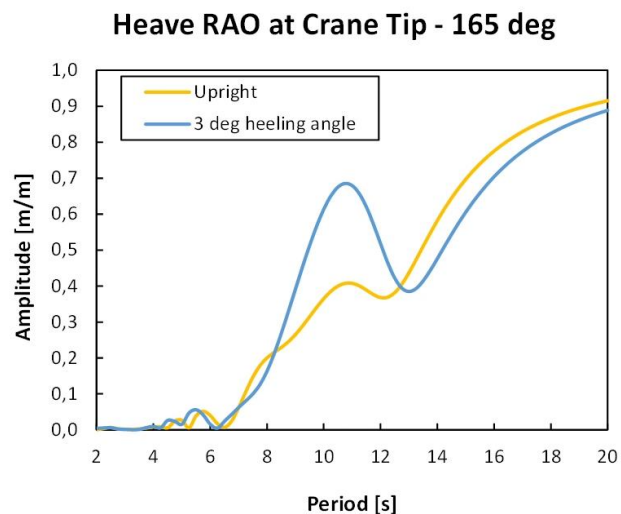
Figure 7-12: Comparison of heave RAO at crane tip for uprigth and heeling vessel - 165 degrees.

The heave RAO for 165 degrees wave direction is presented because this is the direction that the majority of the short-crested waves, in the simulations, arrives from.

7.5   Dynamic Responses for Uncoupled Model

Lowering through the splash zone has also been simulated as an uncoupled model. This means that the tension in the lifting wire, caused by the template, does not influence the vessel responses. Defining vessel motion as prescribed and not calculated simplifies the model and will therefore also decrease the simulation time. This can be beneficial for large models. Some software, like Orcaflex, might also struggle with running the coupled model if horizontal restraints are not set up properly. According to DNV's recommended practice for modelling and analysis of marine operations [1] applying uncoupled vessel RAOs will most likely give conservative results since the object will reduce the vertical crane tip motion for most cases. The vessel responses are predefined motions determined by the wave amplitude and wave period. This is a similar vessel setup as the ROV deployment in Section 5.2.1 and the links helping the vessel maintain its horizontal position is no longer needed. The results from the simulations yields a significantly lower allowable sea state than the results from the simulations with a coupled model.

The results, using displacement RAO obtained when the vessel is in upright state, are presented in Figure 7-13. Both graphs have the same shape, since the vessel responses per wave period are similar, and waves are the primary source for creating vessel motions also for the coupled model. The magnitude of the allowable sea state at each wave period is, however, significantly lower for the uncoupled model. This is because the lifting wire between the load and the crane tip will act as a spring in the coupled model, which will try to compensate the relative motion between the load and the vessel. Increasing the crane radius will further increase this effect, as the moment around the longitudinal axis caused by the ITS will increase when the radius increases. Less dynamic loads are expected for a bigger crane radius, but the capacity of the crane will typically decrease when the radius increases. The movement of the vessel in the uncoupled model is unaffected by the movement of the ITS.

Allowable Sea State - Upright
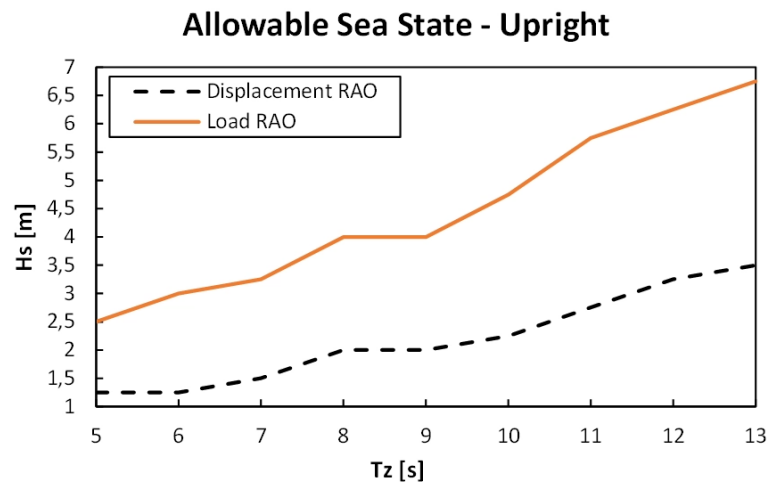
Figure 7-13: Allowable sea state for lowering ITS through splash zone using displacement RAO.

The same pattern for minimum tension in the four legs of the lifting arrangement can be seen in the results for the uncoupled model. Figure 7-14 shows that lifting sling number 2 will statistically experience the lowest tension of the four lifting sling for all simulated mean zero up-crossing periods. This is because the shielding effect is the same for both the coupled and the uncoupled model. The same pattern is evident for all significant wave heights.

Minimum Sling Tension
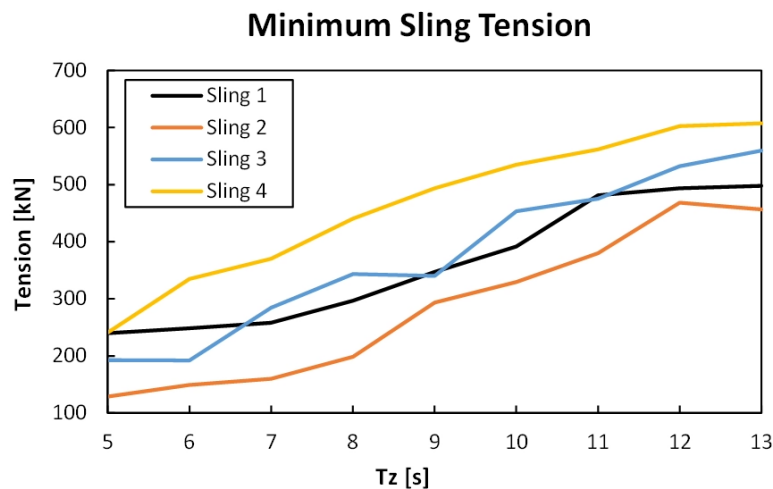
Figure 7-14: ITS deployment - Minimum sling tension for Hs = 2,5 m (uncoupled model).

Three different cases with the same wave condition and the same wave seeds have been simulated in order to take a closer look at the difference between coupled and uncoupled models. The first model is a model where the crane tip

is connected to a rigid point, and the winch payout is the only thing inducing vertical motion to the ITS prior to start of submergence. The second model is the same model used to obtain the results in Section 7.3 (coupled model). The third model is the uncoupled model used to obtain the results in this section.
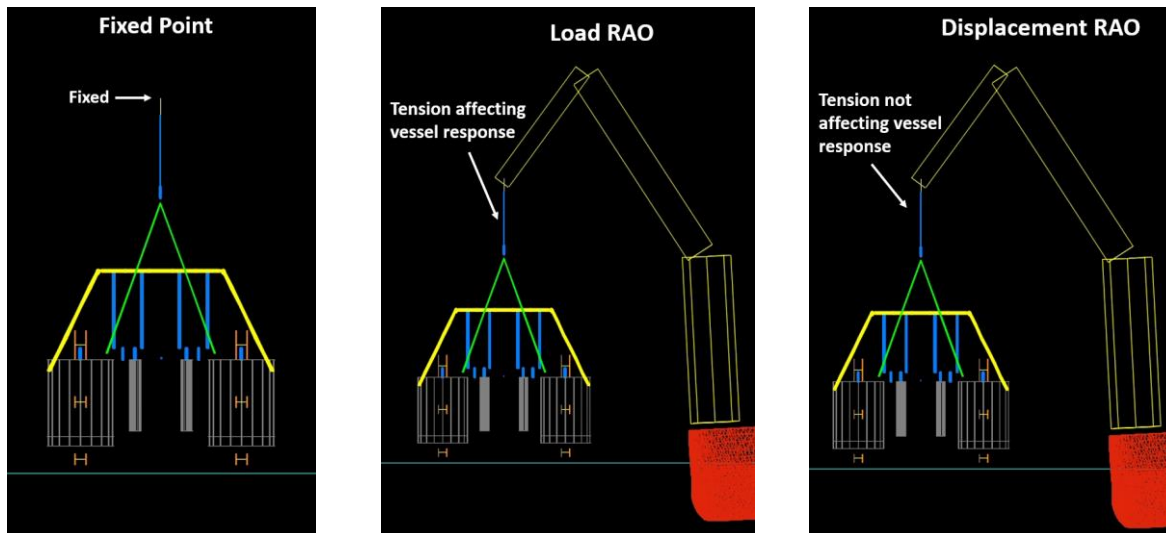
Figure 7-15: ITS Deployment - Illustration of different crane tip/vessel input.

The tension in the lifting wire is directly related to the relative displacement between the crane tip and the lifted object. The force in the lifting wire is according to Hooke's law, a product of displacement and the spring constant. Comparing the time history of lifting wire tension, sea surface clearance and crane tip heave motion suggests that the lifting wire tension is related to the vessel's ability to adjust its motion to the lifted object. This reduces the relative displacement between them. Hence, the maximum wire tension is also reduced. According to Figure 7-16 the maximum peak loads for the fixed crane tip and the vessel described with Displacement RAOs are clearly higher than the peak loads for the vessel described with Load RAO. By comparing the two seeds it can be seen that the maximum dynamic load does not necessarily happen directly after the roof of the suction anchors hits the free surface. The magnitude and location of the maximum peak load for the uncoupled model depends on the timing of the crane tip motion relative to the occurrence of the slamming force. There is more variation in the magnitude of the fixed and uncoupled model than there is for the coupled model. The standard deviation for a sample size of 50 simulations, presented in Table 7-1, reflects the variation of maximum values per sample. The standard deviation for the sample of coupled model simulations is clearly the lowest.
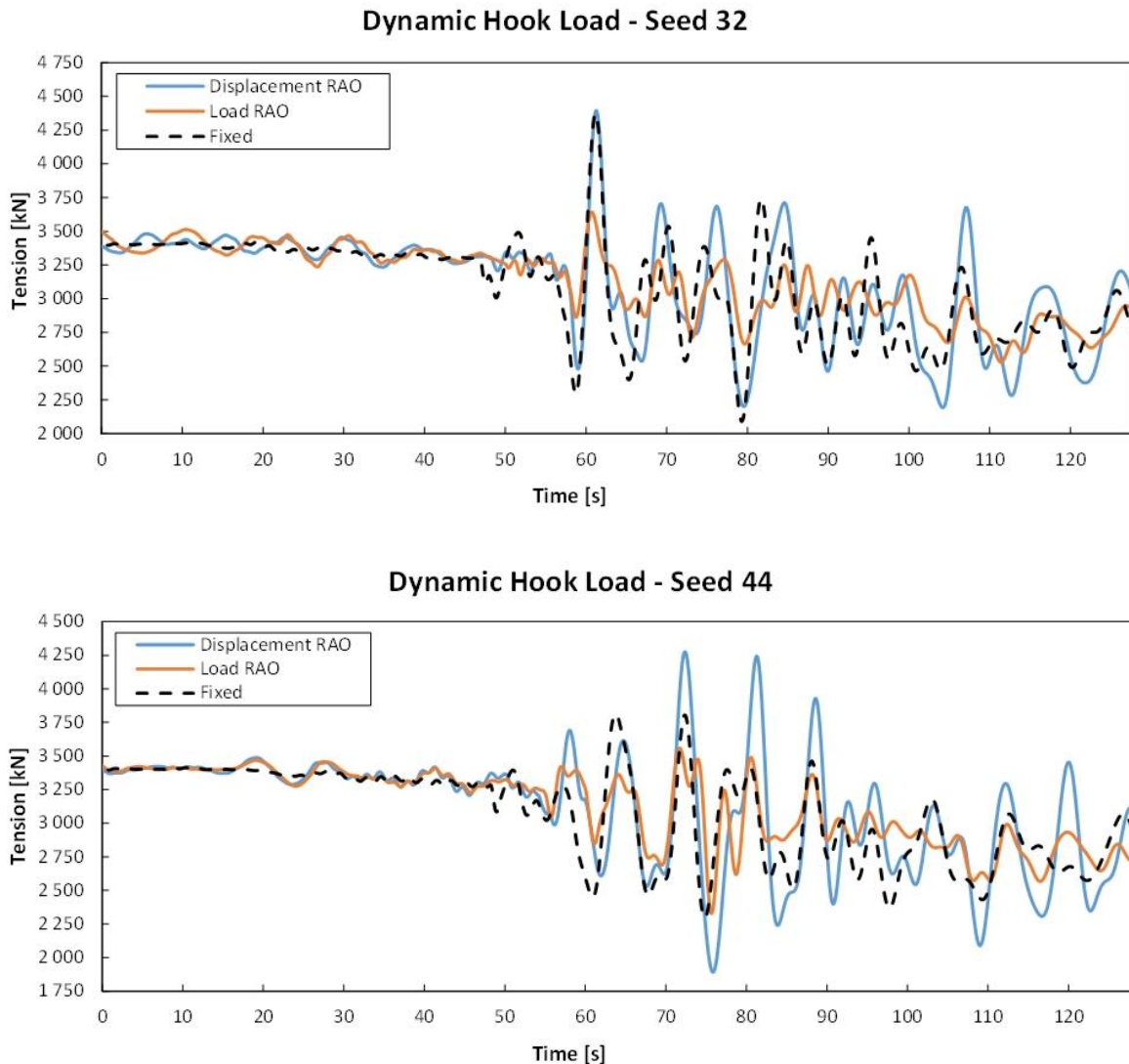
Figure 7-16: Dynamic hook load for the three cases in (Hs = 2,5 m and Tz = 8 s).

Table 7-1: Standard deviation of DHL for Hs = 2,5 m, Tz = 8 s (50 Seeds).

	Displacement RAO	Load RAO	Fixed crane tip
Standard deviation, [kN]	283,5	66	263,7

The standard deviation for the Load RAO is lower because the crane tip adjusts to the motion of the ITS and will therefore create incidents with higher level of resemblance to each other. This means that the maximum values obtained from simulations with a coupled model will deviate less from each other as opposed to uncoupled models and fixed crane tip models, where timing is crucial.

The time history graphs in Figure 7-17 indicates that the heave motion of the crane tip for the coupled model has higher amplitudes than the heave motion of the crane tip for the uncoupled model. The sea surface clearance graphs show a time history of the distance between the crane tip and the sea surface, where both models have similar amplitudes prior to the point where the template crosses the splash zone. The simulation with the coupled model is the only one with reduced amplitude after this point. An amplitude of 0 m would mean that the crane tip follows the sea surface perfectly. It is evident for both seeds that the amplitude of the sea surface clearance in the coupled model simulations reduces at around 60 to 80 seconds. This is the same area where the peak loads in Figure 7-16 occurs. At this stage, the motion of the template is affected by the motions of the waves due to its hydrodynamic properties. This happens regardless if the model is coupled, uncoupled or just a fixed crane tip, but the vessel described with load RAO is the only one that adjusts to the motion of the template. The mean value of all the load RAO z-motion and sea surface clearance time histories increases because the mean value of the lifting wire tension decreases. This will again affect the mean value of the vessel's roll motion.
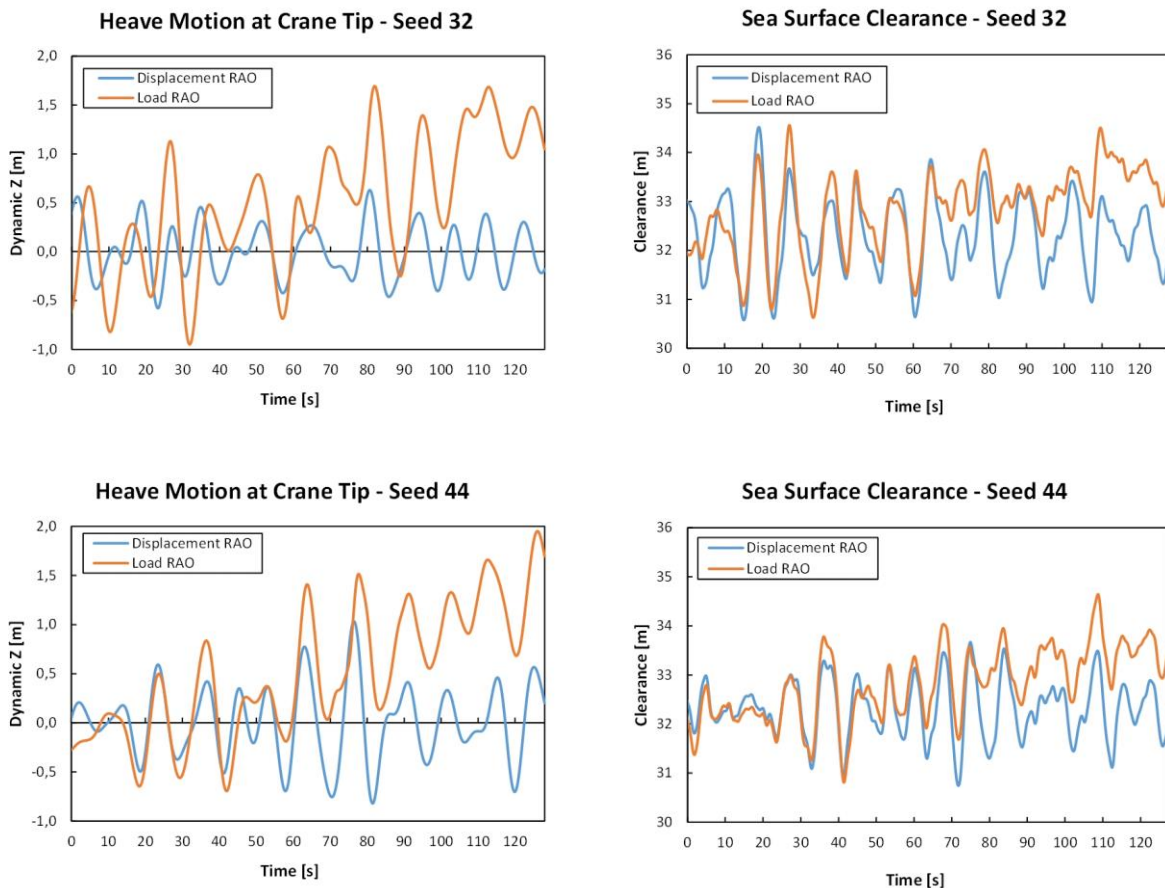
Figure 7-17: Heave motion and sea surface clearance at the crane tip (Hs = 2,5 m and Tz = 8 s).

7.6   Dynamic Responses with Increased Roll Motion

A sensitivity study on the roll response's influence on the dynamic hook load is presented in this chapter. The roll response of the vessel has been increased by changing the additional viscous roll damping during the diffraction analysis. It is interesting to investigate the roll motion's influence on the lifting wire tension since installation vessels can have different loading conditions based on which type of job it will do. This can for example be roll reduction tanks, amount of liquid in other tanks or other equipment on deck. Reducing the additional viscous roll damping in the diffraction analysis is a simplified way to investigate increasing roll motion. Roll reduction tanks or liquid in other tanks, for example, will introduce the free surface effect and therefore also alter the natural period. This is beyond the scope of this thesis and not included in detail. Figure 7-18 shows the roll RAO in beam waves for changing viscous roll damping. The RAO data from the vessels in the three previous sub chapters is also included. The previously studied vessel conditions, "Upright" and "3 deg heeling angle", have a viscous roll damping of 400 000 kNm/(rad/s). All the vessel conditions have been simulated as coupled models with the same setup as the simulations in Section 7.3 and 7.4. The RAO data for the three new vessel conditions are obtained with the vessel in upright position.
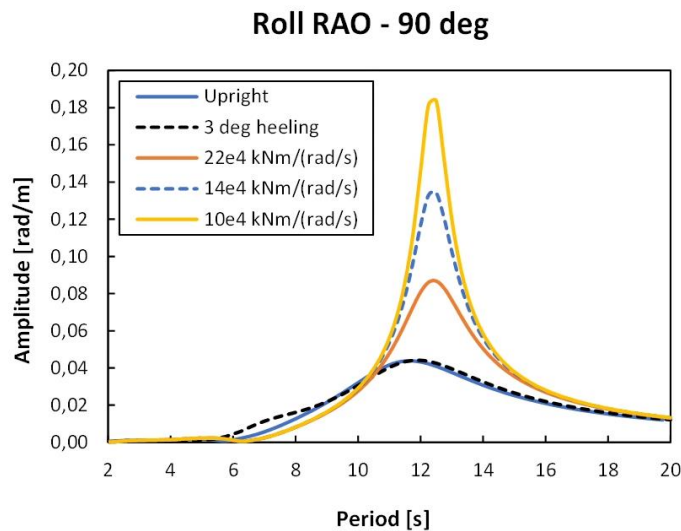
Figure 7-18: Roll RAO in beam waves with changing additional roll damping.

The heave responses for the crane tip will change when the roll responses change. This is reflected in Figure 7-19. The figure shows the RAOs for waves arriving from 165 degrees because this is the direction that the majority of the waves will arrive from in the simulations. A clear relation can be seen between the changing roll motion and the heave responses for the crane tip. The RAOs for the 3 cases increases towards a peak at 12 second wave periods before a significant dip can be seen at around 13 seconds. This is because the heave motion at the crane tip is the sum of the vessels heave, pitch and roll motion (this is briefly discussed in Section 6.3). For larger wave periods all of the vessel conditions approach 1 meter response amplitude per meter wave amplitude.
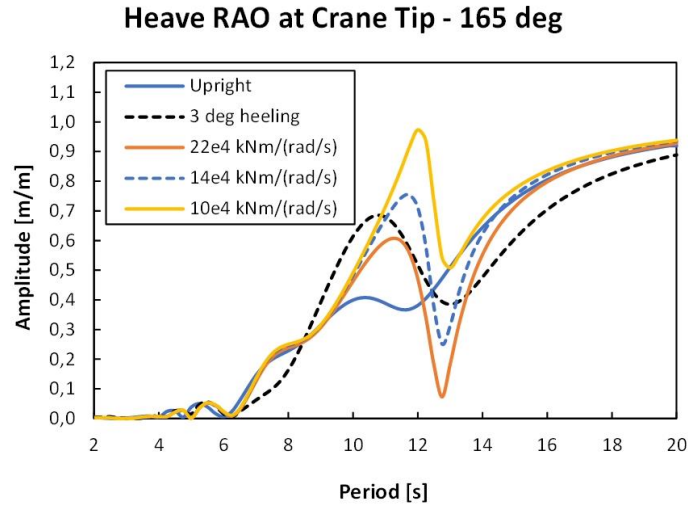
Figure 7-19: Crane tip heave RAO for 165 degrees waves with changing additional roll damping.

The simulations are conducted for a significant wave height of 2,5 meters simply because this is the operational limit that the suppliers of the ITS have set. The results from the simulations shows that the dynamic hook load increases when the roll response of the vessel increases. This will further lead to lower allowable sea states. Even though the heave RAO at the crane tip for the vessel described with RAO data obtained at 3 degrees heeling angle is of similar magnitude as for the vessels analyzed with a roll damping of 22e4 kN/(rad/s) and 14e4 kN/(rad/s), the tension is a lot lower. This is because the roll responses for the vessel at 3 degrees heeling angle is only increasing noticeably when the wave direction is towards the bow, or close to 180 degrees. This is further explained in Section 4.2.1, and can be seen in Figure 7-18 where the roll RAO for the obtained at 3 degrees heeling angle and upright position is the same (both with same viscous roll damping). The roll response for the cases with reduced viscous roll damping, on the other hand, will increase for all directions (except for 180 degrees where the roll response is negligible). The dip in heave RAO at the crane tip for wave periods of approximately 13 seconds is also present in the results. This is the reason for the steep negative slope seen for the three cases with reduced roll damping in Figure 7-20. The dynamic hook load is expected to be lower for large wave periods than for short wave periods, as previously mentioned, but since the slope is a lot steeper for the three cases with reduced roll damping than for the initial cases this is concluded to be because of the dip seen in Figure 7-19. The difference in dynamic hook load is larger for the mid-range of wave periods. The same trend can be seen in the heave RAO graph for the crane tip motions where the graphs follow each other for both short and long wave periods.
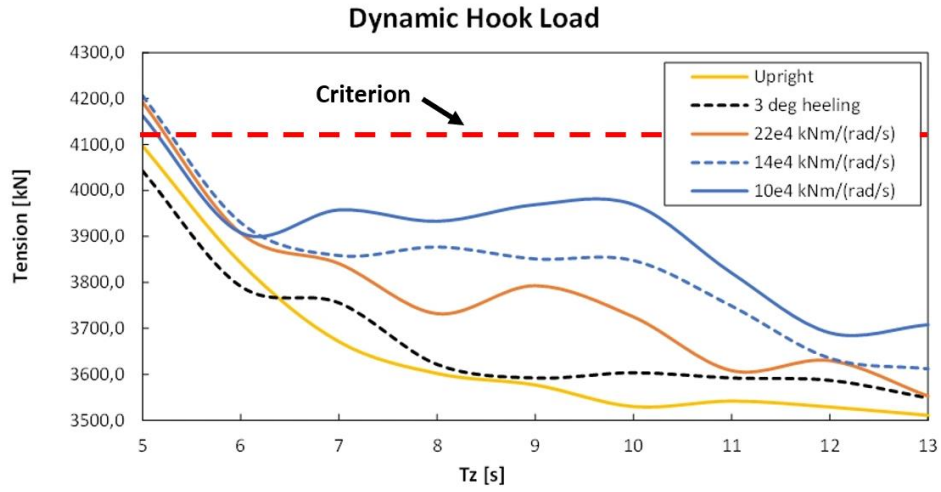
Figure 7-20: Dynamic hook load results for Hs = 2,5 m with changing additional roll damping.

Chapter 8

Discussion and Comparison

This chapter discusses the similarities and differences between the ROV deployment operation and the ITS deployment operation. They are comparable since both vessels are lowering an object through the splash zone and a set of RAOs are calculated for both vessels at the new state of equilibrium to compare with the RAOs for the upright/even keel condition. The ROV deployment takes place at the stern of the vessel, giving the ROV deployment vessel a trimming angle of 3,66 degrees. The ITS deployment, on the other hand, happens on the port side of the ITS deployment vessel. This, along with the counteraction from the ballasting system, induces a heeling angle of 3 degrees.

The vessel motion increases for both vessels when waves arrive along the axis which the vessel is rotated around compared to the motion calculated at the upright/even keel condition. Especially for the ROV deployment, where both head waves and beam waves are simulated, a distinct difference in impact of the inclined RAO data can be seen for beam waves. The allowable sea states barely change for head waves. This is because of the variation in draught across the wave direction axis when the waves arrive from 90 degrees, which is only present when the vessel is trimmed. This is further explained using Figure 4-24. Increased pitch responses for the trimmed case causes lower allowable sea states for the ROV deployment since the increased "crane tip" motion creates a larger pendulum motion. The governing criterion for the ROV deployment is the horizontal clashing between the ROV and the vessel hull, which has a direct relation to the amplitude of the pendulum motion.

The ITS deployment focuses on waves arriving from 165 degrees, which is close to head waves. An increased roll response, and thus increased heave motion at the crane tip, can be seen for the RAOs generated at 3 degrees heeling angle. Like the ROV deployment, the allowable sea states increased when the vessel responses increased. The pendulum motion of the lifted object is not checked against any criterion, like the ROV deployment is, but the RAOs for the vessel at 3 degrees heeling angle will induce larger dynamic hook loads. The larger dynamic hook loads occur because of the increased heave motion of the crane tip.

Table 8-1 summarizes the main changes to the results when the RAO data for upright/even keel condition is replaced with the RAO data for the inclined vessel. Both results from the hydrodynamic analysis and from the time domain simulations are addressed.

Table 8-1: Comparison between changes in results due to different set of RAOs for ROV – and ITS deployment.

ROV Deployment	**ITS Deployment**
• Increased pitch response in beam waves.	• Increased roll response in head waves.
• Small changes in allowable sea states due to tension criterion.	• Decreased allowable sea states due to tension criterion.
• Decreased allowable sea sates due to pendulum motion.	• No pendulum motion criterion.
• Small changes to vessel response in head waves.	• Small changes to vessel response in beam waves.

The overall allowable sea states for the two cases is presented in Figure 8-1 as a summary. As mentioned in Table 8-1, it can be seen that the allowable sea for both cases decreases. This is due to different criterions. Small changes can be seen if the horizontal motion criterion is removed from the ROV deployment case. This is illustrated in Figure 6-24.

a) ROV deployment	b) ITS deployment
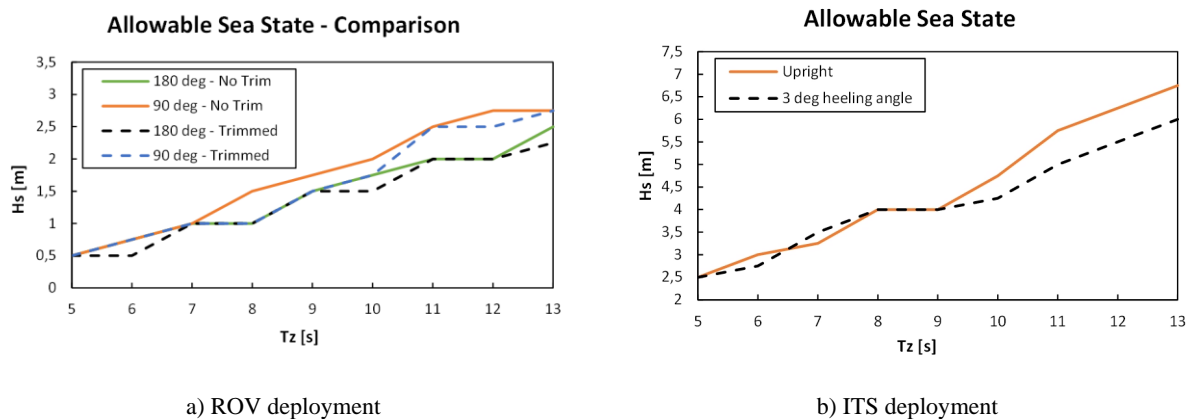
Figure 8-1: Allowable sea state results for the two cases.

The time domain simulations for the ROV deployment has been performed using displacement RAO, and the time domain simulations for the ITS deployment has been performed using load RAO. Load RAO and displacement RAO has been compared by running the ITS deployment time domain simulations in upright position with both types of RAO. The results show that the allowable sea states increase significantly when using load RAO. This is because the tension in the lifting wire makes the vessel adjust to the motion of the template when simulating as a coupled model, while the vessel moves regardless of the lifting wire tension in the uncoupled model.

The sensitivity study on the ITS deployment where the dynamic hook load for changing roll response is investigated shows that the dynamic hook load increases when the roll responses increases. This is because the roll motion contributes to the vertical motion of the crane tip, which has a direct relation to the tension in the lifting wire. The same relation between increasing heave motion of the crane tip and increasing dynamic hook load can be seen for the case with the RAO obtained at 3 degrees heeling angle compared to the simulations with RAO obtained in upright condition.

Chapter 9

Conclusion and Future Work

Two different cases involving offshore lifting operations have been studied in this thesis. Both cases have been compared with regards to changing the response amplitude operators from the ones derived for the vessel in upright/even keel position to the response amplitude operators for an initially trimmed/heeled vessel. The difference between coupled and uncoupled numerical models have been investigated with regards to deployment of a subsea template. This chapter summarizes the findings from both the hydrodynamic analyses and the time domain simulations of both cases and provides a brief discussion and conclusion on the results. The last subchapter discusses suggestions for improvement and recommendation for future work.

9.1   Conclusion

9.1.1   Hydrodynamic Analysis

The results from the frequency domain analysis, which is the basis for the time domain simulations, coincides with the calculated natural periods. Special attention is paid to the waves arriving parallel to the axis that the vessels have been initially rotated around. Waves from this direction will induce larger responses around the axis of which the vessel is rotated when the vessel is analyzed with an initial rotation rather than in upright/even keel condition. This is due to the different wave kinematics at the different draughts. In essence, vessels with an initial heeling angle will have larger roll motion in head waves and vessels with an initial trimming angle will have larger pitch motions in beam waves. This will be applicable for most heavy lifting operations as the weight of the lifted object is the reason for the trimming/heeling. In the interest of reducing the crane tip motions during a lifting operation, the vessels will in many cases have the waves arriving along the axis which it is initially rotated around.

9.1.2   Time Domain Simulations

The results from the hydrodynamic analysis show that the vessels with an initial heeling or trimming angle experience larger responses and decreased allowable sea states compared to vessels analyzed at even keel/upright position. In general, the time domain simulation results indicate that the tension in the lifting wire depends on the magnitude of the crane tip motion and the crane tip's ability to follow the motion of the lifted object. An insignificant change in lifting wire tension is reported for the ROV deployment case when changing the RAOs from the even keel condition to the trimmed condition. The lifting wire tension in the ITS deployment, on the other hand, increases noticeably in the area where the roll responses of the vessel increases when changing the RAOs from the upright condition to the heeling condition. This is because the amplitude of the crane tip motion is larger for the heeling case than for the upright case. The sensitivity study on the roll response's influence on the dynamic hook load adds to the observation that larger crane tip motions induces larger dynamic hook loads.

Larger crane tip motion will not only induce larger lifting wire tension, it also induces larger horizontal motion since the lifting wire and the object at the end will serve as a pendulum. The overall allowable sea state for the ROV deployment reduces when changing the RAOs from the even keel condition the trimmed condition because one of the criterions are directly affected by the pendulum motion. The horizontal clearance reduces and the potential for clashing between the ROV and the vessel increases when the crane tip motion increases. The conclusion for the observations mentioned above is that the motions for the vessels at an inclined condition is larger than the motions for a vessel in upright or even keel condition. This influences the magnitude of the crane tip motion, which subsequently will have an effect on the measured responses to be compared with the operational criteria. The impact of the inclination will vary from case to case, not only from vessel to vessel, but also in terms of the applicable operational criteria.

This thesis also substantiates DNV's statement that applying uncoupled vessel RAOs will typically give conservative results as the crane tip motion will be reduced by the lifted object in most cases. This is true for the ITS deployment simulated in this thesis as a significant decrease in allowable sea states can be seen when changing from a coupled model to an uncoupled model. This is because of the coupled model vessel's ability to adjust to the motion of the lifted object when large hydrodynamic forces are applied to the object.

9.2   Recommendations for Future Work

The diffraction analysis in this study is based on several assumptions and simplifications. A recommendation for future work is to further investigate these assumptions and simplifications. The non-viscous fluid assumption used in the hydrodynamical analysis introduces the need to specify viscous roll damping and viscous fluid damping. Further investigation of the size and damping parameter of the fluid damping lid should be conducted to get representative environmental conditions. Orcina recommend that the damping parameter should be informed by experimental or measured data [29]. The viscous roll damping in this study is based on Froude scaling, in absence of something better. A closer study on this value will increase the validity of the model.

With regards to the time domain simulations, it would be interesting to run a sensitivity study by changing the weight of the lifted object to investigate how it affects the gap between the maximum tension results for the coupled model and the uncoupled model. Heavy objects should influence the motion of the vessel more than light objects. Sensitivity studies are always interesting, since it offers an insight into the significance of the selected parameter. Another parameter can be the spreading coefficient for short-crested waves. This would be interesting for lifting operations in general, as the spreading can vary from one marine location to another.

Like the hydrodynamic analysis, the accuracy of the numerical model for time domain simulations could be improved by conducting model experiments and logging from actual lifting operations to obtain more accurate values for input such as water filling and hydrodynamic coefficients. Water filling is not included in this study, and the results are therefore most likely conservative as this numerical model assumes sudden filling of any hollow elements. The rate of change for added mass is also modeled according to DNV-RP-H103 [1], where a horizontal cylinder is being submerged in water. Conducting model test on the slamming load acting on the suction anchor can potentially have a large impact on the maximum lift wire tension.

A thorough investigation of the change in mass moment of inertia would be a great extension of this study. When the heavy object is overboarded the ballast system will move water to the other side of the vessel to compensate for the large amount of mass extended to one side of the vessel. Both the object itself and the vessel have a significant weight. When the water is pumped to the opposite side of the crane, the case will be a vessel with a large amount of mass on each side. This affects the mass moment of inertia of the vessel and therefore also the rotational motion of the vessel. The heave motion of the crane tip changes when the rotational motion changes and this may lead to other results in terms of allowable sea states.

References

[1] DNV, *DNV-RP-H103: Modelling and Analysis of Marine Operations,* Høvik: DNV, 2009.

[2] Y. Bai and Q. Bai, Subsea Engineering Handbook, Amsterdam; Boston; Paris: Elsevier, 2010.

[3] International Standards Organization, *Petroleum and Natural Gas Industries-Design and Operation of the Subsea Production Systems,* 13628-1: ISO, 2000.

[4] A. M. Nårstad, "Suction Anchor Penetration - Estimating Penetration Resistance Based on CPT Sleeve Friction," Master thesis - NTNU, Trondheim, 2017.

[5] DNVGL, *DNVGL-ST-N001: Marine Operations and Marine Warranty,* Høvik: DNVGL, 2016.

[6] L. Li, Z. Gao and T. Moan, "Response analysis of a nonstationary lowering operation for an offshore wind turbine monopile substructure," *Journal of Offshore Mechanics and Arctic Engineering,* vol. 137, no. 5, 2015.

[7] DNVGL, *DNVGL-RP-N201: Lifting appliances used in subsea operations,* Høvik: DNV, 2019.

[8] L. Li, C. Parra, X. Zhu and M. C. Ong, "Splash zone lowering analysis of a large subsea spool piece," *Marine Structures,* vol. 70, no. 102664, pp. 1-17, 2020.

[9] R. Gordon, G. Grytøyr and M. Dhaigude, "Modeling Suction Pile Lowering Through the Splash Zone," in *ASME 2013 32nd International Conference on Ocean, Offshore and Arctic Engineering*, Nantes, 2013.

[10] R. Bjerkholt, "Analysis of ROV Lift Operation," Master thesis - NTNU, Trondheim, 2014.

[11] A. Aasen, "Analysis of an offshore lifting operation accorind to DNV -How to find the characteristic load by repeated dynamic simulations in the time domain," Master thesis - UiS, Stavanger, 2016.

[12] M. Wu, "Dynamic Analysis of a Subsea Module During Splash-zone Transit," Master thesis - NTNU, Trondheim, 2013.

[13] L. Li, Z. Gao, T. Moan and H. Omberg, "Analysis of lifting operation of a monopile for an offshore wind turbine considering vessel shielding effects," *Marine Structures,* vol. 39, pp. 287-314, 2014.

[14] A. Amer, "Numerical study on the deployment of a subsea template," Master thesis - UiS, Stavanger, 2020.

[15] W. Guachamin-Acero, L. Li, Z. Gao and T. Moan, "Methodology for assessment of the operational limits and operability," *Ocean Engineering,* vol. 125, pp. 308-327, 2016.

[16] L. Li, S. Haver and N. Berlin, "Asssessment of operational limits: Effects of uncertainties in sea state description," *Marine Structures,* vol. 77, 2021.

[17] W. Guachamin-Acero and L. Li, "Methodology for assessment of operational limits including uncertainties in," *Ocean Engineering,* vol. 165, pp. 184-193, 2018.

[18] X. Wu and T. Moan, "Dynamic behaviour of anchor handling vessels during anchor deployment," *Journal of marine science and technology,* vol. 22, no. 4, pp. 655-672, 2017.

[19] O. T. Gudmestad, Marine Technology and Operations: Theory & Practice, Southampton: WIT Press, 2015.

[20] J. Journée and W. Massie, Offshore Hydromechanics, Delft: TU Delft, 2001.

[21] S. Haver, *Metocean Modelling and Prediction of Etxremes,* Stavanger: UiS, NTNU, 2018.

[22] Orcina, "Orcaflex documentation," [Online]. Available: https://www.orcina.com/webhelp/OrcaFlex/Default.htm. [Accessed 12 November 2020].

[23] S. s. Rao, Mechanical Vibrations, Harlow: Pearson Education, 2018.

[24] L. Li, "Dynamic Analysis of the Installation of Monopiles for Offshore Wind Turbines," Doctoral thesis - NTNU, Trondheim, 2016.

[25] DNV, *DNV-RP-C205: Environmental Conditions and Environmental Loads,* Høvik: DNV, 2007.

[26] C. Zhou, "On Extreme Value Statistics," Rozenberg Publishers, Rotterdam, 2008.

[27] E. Pinheiro and S. Ferrari, "A comperative review of generalizations of the Gumbel extreme value distribution with an application to wind speed data," *Journal of Statistical Computation and Simulation,* vol. 86, no. 11, pp. 2241-2261, 2016.

[28] E. J. Gumbel, "Statistical Theory of Extreme Values and Some Practical Applications," National Technical Reports Library, Washington D.C., 1954.

[29] Orcina, "Orcawave documentation," [Online]. Available: https://www.orcina.com/webhelp/OrcaWave/Default.htm. [Accessed 12 November 2020].

[30] C. Geuzaine and J.-F. Remacle, "Gmsh: a three-dimensional finite element mesh generator with built-in pre- and post-processing facilities.," *International Journal for Numerical Methods in Engineering,* vol. 79, no. 11, pp. 1309-1331, 2009.

[31] Autodesk, "Autodesk: Products: Inventor," Autodesk, [Online]. Available: https://www.autodesk.com/products/inventor/overview?plc=INVPROSA&term=1-YEAR&support=ADVANCED&quantity=1. [Accessed 12 November 2020].

[32] C. Geuzaine and J.-F. Remacle, "Gmsh Reference Manual for Gmsh 4.7.0," 6 November 2020. [Online]. Available: http://gmsh.info/doc/texinfo/gmsh.html#Choosing-the-right-unstructured-algorithm. [Accessed 12 November 2020].

[33] Deepocean, "Deepoceangroup.com," [Online]. Available: https://deepoceangroup.com/wp-content/uploads/2018/02/PANTHER-Plus-SEAROV-Specifications-21-02-2018.pdf. [Accessed 3 March 2021].

[34] J. N. Newman, Marine Hydrodynamics, Massachusetts: The MIT Press, 2017.

[35] DNV, "DNV 2.22: Lifting Appliances," DNV, Høvik, 2013.

Appendix A

Froude Scaling

This appendix presents the calculations for the Froude scaling of the viscous roll damping.

Froude Scaling

Beam - Example vessel:

$$B := 16 \; m$$

Roll damping - Example vessel:

$$b_1 := 36000 \; \frac{kN \cdot m}{\frac{rad}{s}}$$

ROV Deployment Vessel

Beam - ROV deployment vessel:

$$B_1 := 3.8 \; m$$

Scaling factor:

$$R := \frac{B}{B_1} = 4.211$$

Roll damping - ROV deployment vessel:

$$b := \frac{b_1}{R^{4.5}} = 56 \; \frac{kN \cdot m}{\frac{rad}{s}}$$

ITS Deployment Vessel

ITS deployment vessel beam:

$$B_2 := 27 \; m$$

Scaling factor:

$$R := \frac{B}{B_2} = 0.593$$

Roll damping for the ITS deployment vessel:

$$b := \frac{b_1}{R^{4.5}} = \left(4 \cdot 10^5\right) \frac{kN \cdot m}{\frac{rad}{s}}$$

<div style="text-align: right;">

Appendix B

</div>

Calculation of Added mass and Natural Periods

This appendix presents the calculations for the added mass and the natural periods. The added mass at infinite frequency is obtained from the lowest analyzed wave period (2 seconds).

Calculation of Natural Period and Added mass

ROV Deployment Vessel

Added Mass - Heave:

Vessel beam: $B := 3.8 \ m$

Length: $L := 14 \ m$

Added mass coefficient: $C_A := 1$

DNV-RP-H103: Table A-1
(Hull shape considered to be circular)

Water density: $\rho := 1025 \ \dfrac{kg}{m^3}$

Reference area: $A_R := \dfrac{\pi \cdot B^2}{8} = 5.671 \ m^2$

Added mass: $A := 2 \cdot \rho \cdot A_R \cdot C_A \cdot L = 163 \ tonne$

Natural Period - Heave:

Mass of vessel: $m := 41 \ tonne$

Hydrostatic stiffness - heave: $k := 358 \ \dfrac{tonne}{s^2}$

Natural period for heave motion: $T_0 := \dfrac{2 \ \pi}{\sqrt{\dfrac{k}{m+A}}} = 4.74 \ s$

Natural Period - Analysis 1

Natural Period - Heave:

Mass of vessel: $m := 41 \ tonne$

Added mass from orcawave: $A := 41 \ tonne$ (Added mass at infinite frequency)

Hydrostatic stiffness - heave: $k := 358 \ \dfrac{tonne}{s^2}$

Natural period for heave motion: $T_0 := \dfrac{2 \ \pi}{\sqrt{\dfrac{k}{m+A}}} = 3.007 \ s$

Natural Period - Roll

Mass moment of inertia: $I_{roll} := 55.3 \ tonne \cdot m^2$

Added mass from orcawave: $A := 20 \ tonne \cdot m^2$ (Added mass at infinite frequency)

Hydrostatic stiffnes - roll:	$k := 67.6 \; kN \cdot m$
Natural period for roll:	$T_0 := \dfrac{2 \, \pi}{\sqrt{\dfrac{k}{I_{roll} + A}}} = 6.631 \; s$

Natural Period - Pitch

Mass moment of inertia:	$I_{pitch} := 455 \; tonne \cdot m^2$
Added mass from orcawave:	$A := 360 \; tonne \cdot m^2$ *(Added mass at infinite frequency)*
Hydrostatic stiffnes - pitch:	$k := 3573 \; kN \cdot m$
Natural period for pitch:	$T_0 := \dfrac{2 \, \pi}{\sqrt{\dfrac{k}{I_{pitch} + A}}} = 3.001 \; s$

Natural Period - Analysis 2

Natural Period - Heave:

Mass of vessel:	$m := 41 \; tonne$
Added mass from orcawave:	$A := 46 \; tonne$ *(Added mass at infinite frequency)*
Hydrostatic stiffness - heave:	$k := 358 \; \dfrac{tonne}{s^2}$
Natural period for heave motion:	$T_0 := \dfrac{2 \, \pi}{\sqrt{\dfrac{k}{m + A}}} = 3.097 \; s$

Natural Period - Roll

Mass moment of inertia:	$I_{roll} := 55.3 \; tonne \cdot m^2$
Added mass from orcawave:	$A := 10 \; tonne \cdot m^2$ *(Added mass at infinite frequency)*
Hydrostatic stiffnes - roll:	$k := 67.6 \; kN \cdot m$
Natural period for roll:	$T_0 := \dfrac{2 \, \pi}{\sqrt{\dfrac{k}{I_{roll} + A}}} = 6.175 \; s$

Natural Period - Pitch

Mass moment of inertia:	$I_{pitch} := 455 \; tonne \cdot m^2$
Added mass from orcawave:	$A := 399 \; tonne \cdot m^2$ *(Added mass at infinite frequency)*

Hydrostatic stiffnes - pitch:	$k := 3573 \ kN \cdot m$
Natural period for pitch:	$T_0 := \dfrac{2 \ \pi}{\sqrt{\dfrac{k}{I_{pitch} + A}}} = 3.072 \ s$

Natural Period - Analysis 3

<u>Natural Period - Heave:</u>

Mass of vessel:	$m := 41 \ tonne$
Added mass from orcawave:	$A := 46 \ tonne$ *(Added mass at infinite frequency)*
Hydrostatic stiffness - heave:	$k := 358 \ \dfrac{tonne}{s^2}$
Natural period for heave motion:	$T_0 := \dfrac{2 \ \pi}{\sqrt{\dfrac{k}{m + A}}} = 3.097 \ s$

<u>Natural Period - Roll</u>

Mass moment of inertia:	$I_{roll} := 55.3 \ tonne \cdot m^2$
Added mass from orcawave:	$A := 10 \ tonne \cdot m^2$ *(Added mass at infinite frequency)*
Hydrostatic stiffnes - roll:	$k := 67.6 \ kN \cdot m$
Natural period for roll:	$T_0 := \dfrac{2 \ \pi}{\sqrt{\dfrac{k}{I_{roll} + A}}} = 6.175 \ s$

<u>Natural Period - Pitch</u>

Mass moment of inertia:	$I_{pitch} := 455 \ tonne \cdot m^2$
Added mass from orcawave:	$A := 399 \ tonne \cdot m^2$ *(Added mass at infinite frequency)*
Hydrostatic stiffnes - pitch:	$k := 3573 \ kN \cdot m$
Natural period for pitch:	$T_0 := \dfrac{2 \ \pi}{\sqrt{\dfrac{k}{I_{pitch} + A}}} = 3.072 \ s$

Natural Period - Analysis 4

<u>Natural Period - Heave:</u>

Mass of vessel:	$m := 41 \ tonne$
Added mass from orcawave:	$A := 47 \ tonne$ *(Added mass at infinite frequency)*
Hydrostatic stiffness - heave:	$k := 351 \ \dfrac{tonne}{s^2}$

Natural period for heave motion:

$$T_0 := \frac{2\pi}{\sqrt{\dfrac{k}{m+A}}} = 3.146 \; s$$

Natural Period - Roll

Mass moment of inertia:

$$I_{roll} := 55.3 \; tonne \cdot m^2$$

Added mass from orcawave:

$$A := 13 \; tonne \cdot m^2 \quad \text{(Added mass at infinite frequency)}$$

Hydrostatic stiffnes - roll:

$$k := 58.9 \; kN \cdot m$$

Natural period for roll:

$$T_0 := \frac{2\pi}{\sqrt{\dfrac{k}{I_{roll}+A}}} = 6.766 \; s$$

Natural Period - Pitch

Mass moment of inertia:

$$I_{pitch} := 455 \; tonne \cdot m^2$$

Added mass from orcawave:

$$A := 432 \; tonne \cdot m^2 \quad \text{(Added mass at infinite frequency)}$$

Hydrostatic stiffnes - pitch:

$$k := 3356 \; kN \cdot m$$

Natural period for pitch:

$$T_0 := \frac{2\pi}{\sqrt{\dfrac{k}{I_{pitch}+A}}} = 3.23 \; s$$

ITS Deployment Vessel
Natural Period - Upright

Natural Period - Heave:

Mass of vessel:

$$m := 18.54 \cdot 10^3 \; tonne$$

Added mass from orcawave:

$$A := 33 \cdot 10^3 \; tonne \quad \text{(Added mass at infinite frequency)}$$

Hydrostatic stiffness - heave:

$$k := 34.08 \cdot 10^3 \; \frac{tonne}{s^2}$$

Natural period for heave motion:

$$T_0 := \frac{2\pi}{\sqrt{\dfrac{k}{m+A}}} = 7.727 \; s$$

Natural Period - Roll

Mass moment of inertia:

$$I_{roll} := 2.056 \cdot 10^6 \; tonne \cdot m^2$$

Added mass from orcawave:

$$A := 645.4 \cdot 10^3 \; tonne \cdot m^2 \quad \text{(Added mass at infinite frequency)}$$

Hydrostatic stiffnes - roll:

$$k := 706.2 \cdot 10^3 \; kN \cdot m$$

Natural period for roll:

$$T_0 := \frac{2\pi}{\sqrt{\dfrac{k}{I_{roll}+A}}} = 12.289 \; s$$

Natural Period - Pitch

Mass moment of inertia:

$$I_{pitch} := 30.88 \cdot 10^6 \; tonne \cdot m^2$$
(Added mass at infinite frequency)

Added mass from orcawave:

$$A := 36 \cdot 10^6 \; tonne \cdot m^2$$

Hydrostatic stiffnes - pitch:

$$k := 48.1 \cdot 10^6 \; kN \cdot m$$

Natural period for pitch:

$$T_0 := \frac{2\pi}{\sqrt{\dfrac{k}{I_{pitch}+A}}} = 7.409 \; s$$

Natural Period - 3 degrees heeling angle

Natural Period - Heave:

Mass of vessel:

$$m := 18.54 \cdot 10^3 \; tonne$$

Added mass from orcawave:

$$A := 34 \cdot 10^3 \; tonne \quad \text{(Added mass at infinite frequency)}$$

Hydrostatic stiffness - heave:

$$k := 34.03 \cdot 10^3 \; \frac{tonne}{s^2}$$

Natural period for heave motion:

$$T_0 := \frac{2\pi}{\sqrt{\dfrac{k}{m+A}}} = 7.807 \; s$$

Natural Period - Roll

Mass moment of inertia:

$$I_{roll} := 2.056 \cdot 10^6 \; tonne \cdot m^2$$
(Added mass at infinite frequency)

Added mass from orcawave:

$$A := 642.4 \cdot 10^3 \; tonne \cdot m^2$$

Hydrostatic stiffnes - roll:

$$k := 703.4 \cdot 10^3 \; kN \cdot m$$

Natural period for roll:

$$T_0 := \frac{2\pi}{\sqrt{\dfrac{k}{I_{roll}+A}}} = 12.306 \; s$$

Natural Period - Pitch

Mass moment of inertia:

$$I_{pitch} := 30.88 \cdot 10^6 \; tonne \cdot m^2$$
(Added mass at infinite frequency)

Added mass from orcawave:

$$A := 35 \cdot 10^6 \; tonne \cdot m^2$$

Hydrostatic stiffnes - pitch:

$$k := 47.8 \cdot 10^6 \; kN \cdot m$$

Natural period for pitch:

$$T_0 := \frac{2\pi}{\sqrt{\dfrac{k}{I_{pitch}+A}}} = 7.376 \; s$$

<div align="right">

Appendix C

</div>

<div align="right">

Calculation of Hydrodynamic Forces for ROV Deployment

</div>

This appendix presents the calculations for the hydrodynamic forces for the ROV deployment.

Calculation of ROV Properties

The below calculations are in accordance with DNV-RP-H103 and the Orcaflex 6d buoy documentation. The TMS is threated as a rectangular box, with the ROV parked inside.

Input:

Gravity constant:

$$g = 9.807 \ \frac{m}{s^2}$$

Seawater density:

$$\rho_w := 1025 \ \frac{kg}{m^3}$$

Width:

$$x := 1491 \ mm$$

Length:

$$y := 1792 \ mm$$

Height:

$$z := 2100 \ mm$$

Mass:

$$M := 1900 \ kg$$

Submerged weight:

$$W_{sub} := 1000 \ kg$$

Displacement:

$$V := \frac{M - W_{sub}}{\rho_w} = 0.878 \ m^3$$

Mass moment of inertia - x:

$$I_x := \frac{1}{12} \cdot M \cdot \left(y^2 + z^2 \right) = 1.207 \ tonne \cdot m^2$$

Mass moment of inertia - y:

$$I_y := \frac{1}{12} \cdot M \cdot \left(x^2 + z^2 \right) = 1.05 \ tonne \cdot m^2$$

Mass moment of inertia - z:

$$I_z := \frac{1}{12} \cdot M \cdot \left(x^2 + y^2 \right) = 0.86 \ tonne \cdot m^2$$

Drag area - x:

$$A_{drag.x} := y \cdot z = 3.763 \ m^2$$

Drag area - y:

$$A_{drag.y} := x \cdot z = 3.131 \ m^2$$

Drag area - z:

$$A_{drag.z} := x \cdot y = 2.672 \ m^2$$

Drag coefficient - x:

$$C_{dx} := 1.16 \qquad \textit{DNV-RP-H103: Appendix B}$$

Drag coefficient - y:

$$C_{dy} := 1.16 \qquad \textit{DNV-RP-H103: Appendix B}$$

Drag coefficient - z:

$$C_{dz} := 2.5 \qquad \textit{DNV-RP-H103: 4.6.2.4}$$

Rotational drag - x:

$$R_{drag.x} := \frac{x}{32} \cdot \left(z^4 \cdot C_{dy} + y^4 \cdot C_{dz} \right) = 2.252 \ m^5$$

Rotational drag - y:	$R_{drag.y} := \dfrac{y}{32} \left(x^4 \cdot C_{dz} + z^4 \cdot C_{dx} \right) = 1.955 \; m^5$
Rotational drag - z:	$R_{drag.z} := \dfrac{z}{32} \left(x^4 \cdot C_{dy} + y^4 \cdot C_{dx} \right) = 1.161 \; m^5$
b/a - Ratio - x:	$ba_x := \dfrac{z}{y} = 1.172$
b/a - Ratio - y:	$ba_y := \dfrac{z}{x} = 1.408$
b/a - Ratio - z:	$ba_z := \dfrac{y}{x} = 1.202$

DNV-RP-H103: Table A-2 Interpolation

Added mass coefficient - x:	$C_{ax} := 0.579 + \dfrac{(0.642 - 0.579) \cdot (ba_x - 1)}{1.25 - 1} = 0.622$

DNV-RP-H103: Table A-2 Interpolation

Added mass coefficient - y:	$C_{ay} := 0.642 + \dfrac{(0.690 - 0.642) \cdot (ba_y - 1.25)}{1.5 - 1.25} = 0.672$

DNV-RP-H103: Table A-2 Interpolation

Added mass coefficient - y:	$C_{az} := 0.579 + \dfrac{(0.642 - 0.579) \cdot (ba_z - 1)}{1.25 - 1} = 0.63$
Reference volume - x:	$V_x := \dfrac{\pi}{4} \cdot y^2 \cdot z = 5.296 \; m^3$
Reference volume - y:	$V_y := \dfrac{\pi}{4} \cdot x^2 \cdot z = 3.667 \; m^3$
Reference volume - z:	$V_z := \dfrac{\pi}{4} \cdot x^2 \cdot y = 3.129 \; m^3$
Added mass 2d - x:	$A_{22x} := \rho_w \cdot C_{ax} \cdot V_x = 3.378 \; tonne$
Added mass 2d - y:	$A_{22y} := \rho_w \cdot C_{ay} \cdot V_y = 2.527 \; tonne$
Added mass 2d - z:	$A_{22z} := \rho_w \cdot C_{az} \cdot V_z = 2.02 \; tonne$
Lambda - x:	$\lambda_x := \dfrac{\sqrt{A_{drag.x}}}{x + \sqrt{A_{drag.x}}} = 0.565$ *DNV-RP-H103: 4.6.3.3*
Lambda - y:	$\lambda_y := \dfrac{\sqrt{A_{drag.y}}}{y + \sqrt{A_{drag.y}}} = 0.497$ *DNV-RP-H103: 4.6.3.3*

Lambda - z:

$$\lambda_z := \frac{\sqrt{A_{drag.z}}}{z + \sqrt{A_{drag.z}}} = 0.438 \qquad \textit{DNV-RP-H103: 4.6.3.3}$$

Added mass 3d - x:

$$A_{33x.0} := A_{22x} \cdot \left(1 + \sqrt{\frac{1 - \lambda_x^2}{2 \cdot \left(1 + \lambda_x^2\right)}}\right) = 5.094 \ \textit{tonne}$$

Added mass 3d - y:

$$A_{33y.0} := A_{22y} \cdot \left(1 + \sqrt{\frac{1 - \lambda_y^2}{2 \cdot \left(1 + \lambda_y^2\right)}}\right) = 3.916 \ \textit{tonne}$$

Added mass 3d - z:

$$A_{33z.0} := A_{22z} \cdot \left(1 + \sqrt{\frac{1 - \lambda_z^2}{2 \cdot \left(1 + \lambda_z^2\right)}}\right) = 3.197 \ \textit{tonne}$$

Perforation Ratio - x:

$$p_x := 0.1 \qquad\qquad\qquad \text{Guesstimated.}$$

Perforation Ratio - y:

$$p_y := 0.1 \qquad\qquad\qquad \text{Guesstimated.}$$

Perforation Ratio - z:

$$p_z := 0.1 \qquad\qquad\qquad \text{Guesstimated.}$$

Reduction Factor - x:

$$R_x := 0.97 \qquad\qquad \text{DNV-RP-H103: figure 4.7}$$

Reduction Factor - y:

$$R_y := 0.97 \qquad\qquad \text{DNV-RP-H103: figure 4.7}$$

Reduction Factor - z:

$$R_z := 0.97 \qquad\qquad \text{DNV-RP-H103: figure 4.7}$$

Added mass 3d reduced - x:

$$A_{33x} := A_{33x.0} \cdot R_x = 4.941 \ \textit{tonne}$$

Added mass 3d reduced - y:

$$A_{33y} := A_{33y.0} \cdot R_y = 3.798 \ \textit{tonne}$$

Added mass 3d reduced - z:

$$A_{33z} := A_{33z.0} \cdot R_z = 3.101 \ \textit{tonne}$$
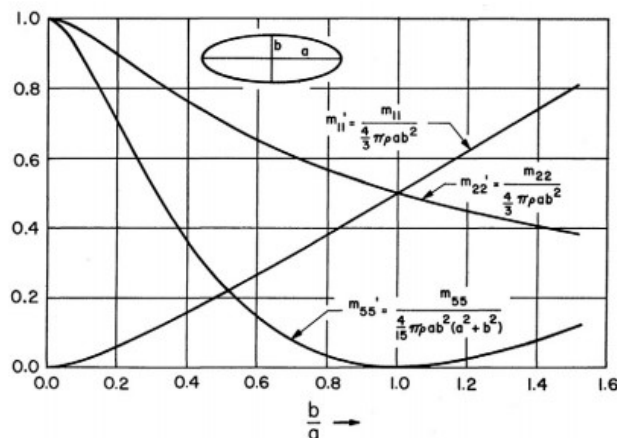
b/a - Ratio - x:	$ba_x := \dfrac{2 \cdot \sqrt{\dfrac{y \cdot z}{\pi}}}{x} = 1.468$
b/a - Ratio - y:	$ba_y := \dfrac{2 \cdot \sqrt{\dfrac{x \cdot z}{\pi}}}{y} = 1.114$
b/a - Ratio - z:	$ba_y := \dfrac{2 \cdot \sqrt{\dfrac{x \cdot y}{\pi}}}{z} = 0.878$
Rotational addd mass coefficients from figure:	$C_{arx} := 0.1$
	$C_{ary} := 0.01$
	$C_{az} := 0.02$

Input for Orcaflex:

Hydrodynamic mass:	$HM := V \cdot \rho_w = 900 \; \boldsymbol{kg}$
Hydrodynamic inertia - x:	$HI_x := \dfrac{HM}{M} \cdot I_x = 0.572 \; \boldsymbol{tonne \cdot m}^2$
Hydrodynamic inertia - y:	$HI_y := \dfrac{HM}{M} \cdot I_y = 0.497 \; \boldsymbol{tonne \cdot m}^2$
Hydrodynamic inertia - z:	$HI_z := \dfrac{HM}{M} \cdot I_z = 0.408 \; \boldsymbol{tonne \cdot m}^2$
Translational added mass coefficients:	$C_{ax} := \dfrac{A_{33x}}{HM} = 5.49$
	$C_{ay} := \dfrac{A_{33y}}{HM} = 4.22$
	$C_{az} := \dfrac{A_{33z}}{HM} = 3.45$
Height of slam buoy (lumped):	$h := 0.1 \; \boldsymbol{m}$
Added mass rate of change - Vertical direction:	$AM_R := \dfrac{A_{33z}}{h} = 31.007 \; \dfrac{\boldsymbol{tonne}}{\boldsymbol{m}}$
Slamming Area:	$A_P := x \cdot y = 2.672 \; \boldsymbol{m}^2$
Slamming coefficient - entry	$C_{s.entry} := \dfrac{2 \cdot AM_R}{\rho_w \cdot A_P} = 22.644$ *DNV-RP-H103: 3.2.9.2*

Appendix D

Calculation of Hydrodynamic Forces for ITS Deployment

This appendix presents the calculations for the hydrodynamic forces for the ITS deployment.

Calculation of ITS Properties

Suction Anchor

Outer diameter:

$$OD := 6 \; \boldsymbol{m}$$

Wall thickness:

$$wt := 20 \; \boldsymbol{mm}$$

Inner diameter:

$$ID := OD - 2 \cdot wt = 5.96 \; \boldsymbol{m}$$

Height:

$$h := 7.9 \; \boldsymbol{m}$$

Top plate thickness:

$$t := 30 \; \boldsymbol{mm}$$

Ventilation hole diamter:

$$D_{vent} := 1 \; \boldsymbol{m}$$

Number of ventilation holes:

$$n_{vent} := 2$$

Steel density:

$$\rho_s := 7850 \; \frac{\boldsymbol{kg}}{\boldsymbol{m}^3}$$

Water density:

$$\rho_w := 1025 \; \frac{\boldsymbol{kg}}{\boldsymbol{m}^3}$$

Weight of skirt:

$$m_{skirt} := \frac{\rho_s \cdot h \cdot \pi \cdot \left(OD^2 - ID^2\right)}{4} = 23.301 \; \boldsymbol{tonne}$$

Weight of top plate:

$$m_{plate} := \frac{\rho_s \cdot t \cdot \pi \cdot OD^2}{4} = 6.659 \; \boldsymbol{tonne}$$

Total weight of suction anchor:

$$m_{anchor} := m_{skirt} + m_{plate} = 29.96 \; \boldsymbol{tonne}$$

Mass moment of inertia for suction anchors:

$$I_x := \frac{1}{12} \cdot m_{anchor} \cdot \left(\frac{3}{4} \cdot \left(OD^2 + ID^2\right) + h^2\right)$$

$$I_y := I_x = 289.739 \; \boldsymbol{tonne} \cdot \boldsymbol{m}^2$$

$$I_z := \frac{m_{anchor} \cdot \left(OD^2 + ID^2\right)}{8} = 267.846 \; \boldsymbol{tonne} \cdot \boldsymbol{m}^2$$

Projected area:

$$A_{pA} := \frac{\pi}{4} \cdot OD^2 = 28.274 \; \boldsymbol{m}^2$$

Perforation percentage:

$$p := \frac{n_{vent} \cdot \frac{\pi}{4} \cdot D_{vent}^2}{A_{pA}} \cdot 100 = 5.556$$

Length-diameter ratio:

$$b2a := \frac{h}{OD} = 1.317$$

2d Steady flow drag coefficient - rough cylinder:

$$C_{DS.2D} := 1.05$$

Reduction factor:	$\kappa := 0.8$	*DNV-RP-H103: Table B-2*

KC-number: $\qquad KC := \dfrac{\pi \cdot h}{OD} = 4.136$

Wake amplification factor: $\qquad \psi := 0.8 \qquad\qquad$ *DNV-RP-C205 Figure 6-5*

3d Steady flow drag coefficient: $\qquad C_{DS.3D} := C_{DS.2D} \cdot \kappa = 0.84$

Drag coefficient for oscillating flow: $\qquad C_{DS} := C_{DS.3D} \cdot \psi = 0.672$

$\qquad\qquad\qquad\qquad\qquad\qquad\qquad\qquad$ *DNV-RP-H103: Table A-2 Interpolation*

Added mass coefficient - normal to cylinder: $\qquad C_a := 0.62 + \dfrac{(0.78 - 0.62) \cdot (b2a - 1.2)}{2.5 - 1.2} = 0.634$

Vertical Added Mass - Upper and Lower Sphere:

Added mass coefficient for circular disc: $\qquad C_a := \dfrac{2}{\pi} = 0.637 \qquad$ *DNV-RP-H103: Table A-2*

Reference volume for circular disc: $\qquad V_r := \dfrac{4}{3} \pi \cdot \left(\dfrac{OD}{2}\right)^3 = 113.097 \ m^3$

Added mass for circular disc: $\qquad A_{330} := \dfrac{\rho_w \cdot C_a \cdot V_r}{2} = 36.9 \ tonne$

Lambda: $\qquad \lambda := \dfrac{\sqrt{A_{pA}}}{h + \sqrt{A_{pA}}} = 0.402$

Added mass for solid object: $\qquad A_{33s} := A_{330} \cdot \left(1 + \sqrt{\dfrac{1 - \lambda^2}{2\ (1 + \lambda^2)}}\right) = 59.061 \ tonne$

Reduced added mass due to perforation: $\qquad A_{33} := A_{33s} \cdot \left(0.7 + 0.3 \cdot \cos\left(\dfrac{\pi \cdot (p - 5)}{34}\right)\right) = 59.038 \ tonne$

Input from DNV-RP-H103
Figure 3-5:
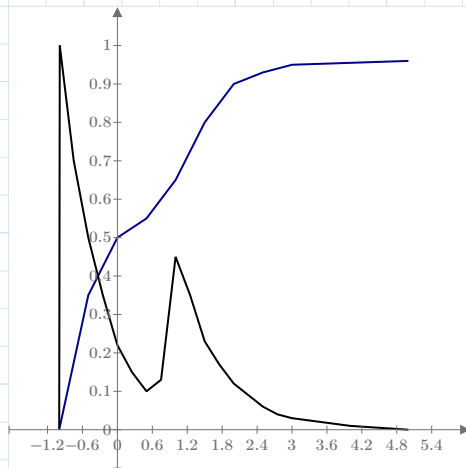
h_r	C_{ar}		h_{rc}	dC_a
-1	0		-1	0
-0.5	0.35		-0.99	1
0	0.5		-0.75	0.7
0.5	0.55		-0.5	0.5
1	0.65		-0.25	0.35
1.5	0.8		0	0.22
2	0.9		0.25	0.15
2.5	0.93		0.5	0.1
3	0.95		0.75	0.13
5	0.96		1	0.45
			1.25	0.35
			1.5	0.23
			1.75	0.17
			2	0.12
			2.25	0.09
			2.5	0.06
			2.75	0.04
			3	0.03
			4	0.01
			5	0

C_{ar}

dC_a

h_r

h_{rc}

Distance from centroid of upper
sphere to suction anchor roof:

$$h_{sU} := \frac{4\ OD}{6\ \pi} = 1.273\ \boldsymbol{m}$$

Distance from centroid of lower sphere
to waterline when fully submerged

$$h_{sL} := h + \frac{4\ OD}{6\ \pi} = 9.173\ \boldsymbol{m}$$

Diameter of AM line element:

$$D_{line} := 1\ \boldsymbol{m}$$

Diameter of AM line element - Upper sphere:

$$D_{line.u} := 2 \cdot h_{sU} = 2.546\ \boldsymbol{m}$$

Length of AM line element:

$$L_{line} := 1\ \boldsymbol{m}$$

AM line element buoyancy:

$$B_{line} := \frac{\pi \cdot D_{line}^2}{4} \cdot L_{line} \cdot \rho_w = 0.805\ \boldsymbol{tonne}$$

AM line element buoyancy -
upper sphere:

$$B_{line.u} := \frac{\pi \cdot D_{line.u}^2}{4} \cdot L_{line} \cdot \rho_w = 5.22\ \boldsymbol{tonne}$$

Input for added mass - lower
sphere:

$$C_{ai} := \frac{A_{33}}{B_{line}} \cdot C_{ar} = \begin{bmatrix} 0 \\ 25.668 \\ 36.668 \\ 40.335 \\ 47.669 \\ 58.669 \\ 66.003 \\ 68.203 \\ 69.669 \\ 70.403 \end{bmatrix}$$

Input for added mass - upper
sphere:

$$C_{ai} := \frac{A_{33}}{B_{line.u}} \cdot C_{ar} = \begin{bmatrix} 0 \\ 3.958 \\ 5.655 \\ 6.22 \\ 7.351 \\ 9.048 \\ 10.178 \\ 10.518 \\ 10.744 \\ 10.857 \end{bmatrix}$$

Input for normalized submergence -
variable added mass for upper sphere:

$$h_{iU} := h_r$$

Input for normalized submergence -
variable added mass for lower sphere:

$$h_{iL} := h_r + \frac{2\,h_{sL}}{D_{line}} = \begin{bmatrix} 17.346 \\ 17.846 \\ 18.346 \\ 18.846 \\ 19.346 \\ 19.846 \\ 20.346 \\ 20.846 \\ 21.346 \\ 23.346 \end{bmatrix}$$

Input for added mass rate of
change - lower sphere:

$$dC_{ai} := \frac{A_{33}}{B_{line}} \cdot dC_a = \begin{bmatrix} 0 \\ 73.336 \\ 51.335 \\ 36.668 \\ 25.668 \\ 16.134 \\ 11 \\ 7.334 \\ 9.534 \\ 33.001 \\ 25.668 \\ 16.867 \\ 12.467 \\ 8.8 \\ 6.6 \\ 4.4 \\ 2.933 \\ 2.2 \\ 0.733 \\ 0 \end{bmatrix}$$

Input for added mass rate of change - upper sphere:

$$dC_{ai} := \frac{A_{33}}{B_{line.u}} \cdot dC_a = \begin{bmatrix} 0 \\ 11.309 \\ 7.917 \\ 5.655 \\ 3.958 \\ 2.488 \\ 1.696 \\ 1.131 \\ 1.47 \\ 5.089 \\ 3.958 \\ 2.601 \\ 1.923 \\ 1.357 \\ 1.018 \\ 0.679 \\ 0.452 \\ 0.339 \\ 0.113 \\ 0 \end{bmatrix}$$

Input for normalized submergence - added mass rate of change for upper sphere:

$$h_{iiU} := h_{rc}$$

Input for normalized submergence - added mass rate of change for lower sphere:

$$h_{iiL} := h_{rc} + \frac{2 \, h_{sL}}{D_{line}} = \begin{bmatrix} 17.346 \\ 17.356 \\ 17.596 \\ 17.846 \\ 18.096 \\ 18.346 \\ 18.596 \\ 18.846 \\ 19.096 \\ 19.346 \\ 19.596 \\ 19.846 \\ 20.096 \\ 20.346 \\ 20.596 \\ 20.846 \\ 21.096 \\ 21.346 \\ 22.346 \\ 23.346 \end{bmatrix}$$

<u>Vertical Added Mass - Trapped Water</u>

Added mass (trapped water):

$$A_{33} := \rho_w \cdot \frac{\pi}{4} \left(ID^2 - 2 \cdot D_{vent}^2 \right) \cdot h = 213.189 \; \textit{tonne}$$

Distance from centroid of trapped water to waterline when fully submerged:

$$h_{sT} := 4 \; \textit{m}$$

Input for added mass:

$$C_{ai} := \frac{A_{33}}{B_{line}} \cdot C_{ar} = \begin{bmatrix} 0 \\ 92.687 \\ 132.41 \\ 145.651 \\ 172.133 \\ 211.857 \\ 238.339 \\ 246.283 \\ 251.58 \\ 254.228 \end{bmatrix}$$

Input for normalized submergence - variable added mass for trapped water:

$$h_{iT} := h_r + \frac{2\,h_{sT}}{D_{line}} = \begin{bmatrix} 7 \\ 7.5 \\ 8 \\ 8.5 \\ 9 \\ 9.5 \\ 10 \\ 10.5 \\ 11 \\ 13 \end{bmatrix}$$

Input for added mass rate of change:

$$dC_{ai} := \frac{A_{33}}{B_{line}} \cdot dC_a = \begin{bmatrix} 0 \\ 264.821 \\ 185.374 \\ 132.41 \\ 92.687 \\ 58.261 \\ 39.723 \\ 26.482 \\ 34.427 \\ 119.169 \\ 92.687 \\ 60.909 \\ 45.02 \\ 31.778 \\ 23.834 \\ 15.889 \\ 10.593 \\ 7.945 \\ 2.648 \\ 0 \end{bmatrix}$$

Input for normalized submergence - added mass rate of change for trapped water:

$$h_{iiU} := h_{rc} + \frac{2\,h_{sT}}{D_{line}} = \begin{bmatrix} 7 \\ 7.01 \\ 7.25 \\ 7.5 \\ 7.75 \\ 8 \\ 8.25 \\ 8.5 \\ 8.75 \\ 9 \\ 9.25 \\ 9.5 \\ 9.75 \\ 10 \\ 10.25 \\ 10.5 \\ 10.75 \\ 11 \\ 12 \\ 13 \end{bmatrix}$$

Tail Pipe

Outer diameter:

$$OD := 1 \; m$$

Wall Thickness:

$$wt := 20 \; mm$$

Inner diameter:

$$ID := OD - 2 \; wt = 0.96 \; m$$

Height:

$$h := 6.5 \; m$$

Weight of skirt:

$$m_{tail} := \frac{\rho_s \cdot h \cdot \pi \cdot \left(OD^2 - ID^2\right)}{4} = 3.142 \; tonne$$

Mass moment of inertia for tail pipe:

$$I_x := \frac{1}{12} \cdot m_{tail} \cdot \left(\frac{3}{4} \cdot \left(OD^2 + ID^2\right) + h^2\right)$$

$$I_y := I_x = 11.439 \; tonne \cdot m^2$$

$$I_z := \frac{m_{tail} \cdot \left(OD^2 + ID^2\right)}{8} = 0.755 \; tonne \cdot m^2$$

Length-diameter ratio:

$$b2a := \frac{h}{OD} = 6.5$$

2d Steady flow drag coefficient - rough cylinder

$$C_{DS.2D} := 1.05$$

Reduction factor:

$$\kappa := 0.8 \qquad \text{DNV-RP-H103: Table B-2}$$

KC-number:

$$KC := \frac{\pi \cdot h}{OD} = 20.42$$

Wake amplification factor:

$$\psi := 1.25 \qquad \text{DNV-RP-C205: Figure 6-5}$$

3D Steady flow drag coefficient:

$$C_{DS.3D} := C_{DS.2D} \cdot \kappa = 0.84$$

Drag coefficient for oscillating flow:

$$C_{DS} := C_{DS.3D} \cdot \psi = 1.05$$

DNV-RP-H103: Table A-2 Interpolation

Added mas coefficient - normal to cylinder:

$$C_a := 0.9 + \frac{(0.96 - 0.9) \cdot (b2a - 5)}{9 - 5} = 0.923$$

Top Structure

Pipe 1

Outer diameter:

$$OD_{p1} := 0.7 \; m$$

Wall thickness:

$$wt := 27 \; mm$$

Inner diameter:

$$ID_{p1} := OD_{p1} - 2 \; wt = 0.646 \; m$$

Length per section:

$$h := 11 \; m$$

Total length of pipe 1:	$l_{p1} := 62 \; m$
Weight of pipe:	$m_{p1} := \dfrac{\rho_s \cdot l_{p1} \cdot \pi \cdot \left(OD_{p1}{}^2 - ID_{p1}{}^2\right)}{4} = 27.784 \; tonne$
Length-diameter ratio:	$b2a := \dfrac{h}{OD_{p1}} = 15.714$
2D Steady flow drag coefficient - rough cylinder	$C_{DS.2D} := 1.05$ *DNV-RP-H103: Table A-2*
	DNV-RP-H103: Table B-2
Reduction factor:	$\kappa := 0.82 + \dfrac{(0.90 - 0.82) \cdot (20 - b2a)}{20 - 10} = 0.854$
KC-number:	$KC := \dfrac{\pi \cdot h}{OD} = 34.558$
Wake amplification factor:	$\psi := 1.15$ *DNV-RP-C205: Figure 6-5*
3D Steady flow drag coefficient:	$C_{DS.3D} := C_{DS.2D} \cdot \kappa = 0.897$
Drag coefficient for oscillating flow:	$C_D := C_{DS.3D} \cdot \psi = 1.032$
Added mas coefficient - normal to cylinder:	$C_a := 1$ *DNV-RP-H103: Table A-2*

Pipe 2

Outer diameter:	$OD_{p2} := 0.5 \; m$
Wall thickness:	$wt := 15 \; mm$
Inner diameter:	$ID_{p2} := OD_{p2} - 2 \; wt = 0.47 \; m$
Length per section:	$h := 11 \; m$
Total length of pipe 2:	$l_{p2} := 44 \; m$
Weight of pipe:	$m_{p2} := \dfrac{\rho_s \cdot l_{p2} \cdot \pi \cdot \left(OD_{p2}{}^2 - ID_{p2}{}^2\right)}{4} = 7.894 \; tonne$
Length-diameter ratio:	$b2a := \dfrac{h}{OD_{p2}} = 22$
2d Steady flow drag coefficient - rough cylinder	$C_{DS.2D} := 1.05$ *DNV-RP-H103: Table A-2*
	DNV-RP-H103: Table B-2
Reduction factor:	$\kappa := 0.82 + \dfrac{(0.90 - 0.82) \cdot (20 - b2a)}{20 - 10} = 0.804$
KC-number:	$KC := \dfrac{\pi \cdot h}{OD} = 34.558$

Wake amplification factor:	$\psi := 1.15$	*DNV-RP-C205: Figure 6-5*
3d Steady flow drag coefficient:	$C_{DS.3D} := C_{DS.2D} \cdot \kappa = 0.844$	
Drag coefficient for oscillating flow:	$C_D := C_{DS.3D} \cdot \psi = 0.971$	
Added mas coefficient - normal to cylinder:	$C_a := 1$	*DNV-RP-H103: Table A-2*

Guideposts

Number of guideposts:	$n_{gp} := 16$	
Weight:	$m_{gp} := 1.39 \; \textbf{tonne}$	
Buoyancy:	$B := 0.18125 \; \textbf{tonne}$	
Height:	$h := 7 \; \textbf{m}$	
Outer diameter:	$OD := 0.2 \; \textbf{m}$	
Displacement:	$V := \dfrac{B}{\rho_w} = 0.177 \; \textbf{m}^3$	
Total weight of GPs:	$m_{gp.tot} := n_{gp} \cdot m_{gp} = 22.24 \; \textbf{tonne}$	
Length-diameter ratio:	$b2a := \dfrac{h}{OD} = 35$	
2d Steady flow drag coefficient - rough cylinder	$C_{DS.2D} := 1.05$	*DNV-RP-H103: Table A-2*
		DNV-RP-H103: Table B-2
Reduction factor:	$\kappa := 0.9 + \dfrac{(0.98 - 0.9) \cdot (40 - b2a)}{40 - 20} = 0.92$	
KC-number:	$KC := \dfrac{\pi \cdot h}{OD} = 109.956$	
Wake amplification factor:	$\psi := 1$	*DNV-RP-C205: Figure 6-5*
3d Steady flow drag coefficient:	$C_{DS.3D} := C_{DS.2D} \cdot \kappa = 0.966$	
Drag coefficient for oscillating flow:	$C_D := C_{DS.3D} \cdot \psi = 0.966$	
Added mass coefficient - normal to cylinder:	$C_a := 1$	
Added mass:	$A_{33o} := \dfrac{C_a \cdot \rho_w \cdot h \cdot \pi \cdot OD^2}{4} = 0.225 \; \textbf{tonne}$	
Added mass coefficient for orcaflex:	$C_a := \dfrac{A_{33o}}{B} = 1.244$	
Drag area - Normal to cylinder:	$A_{drag} := OD \cdot h = 1.4 \; \textbf{m}^2$	

Bottom Structure
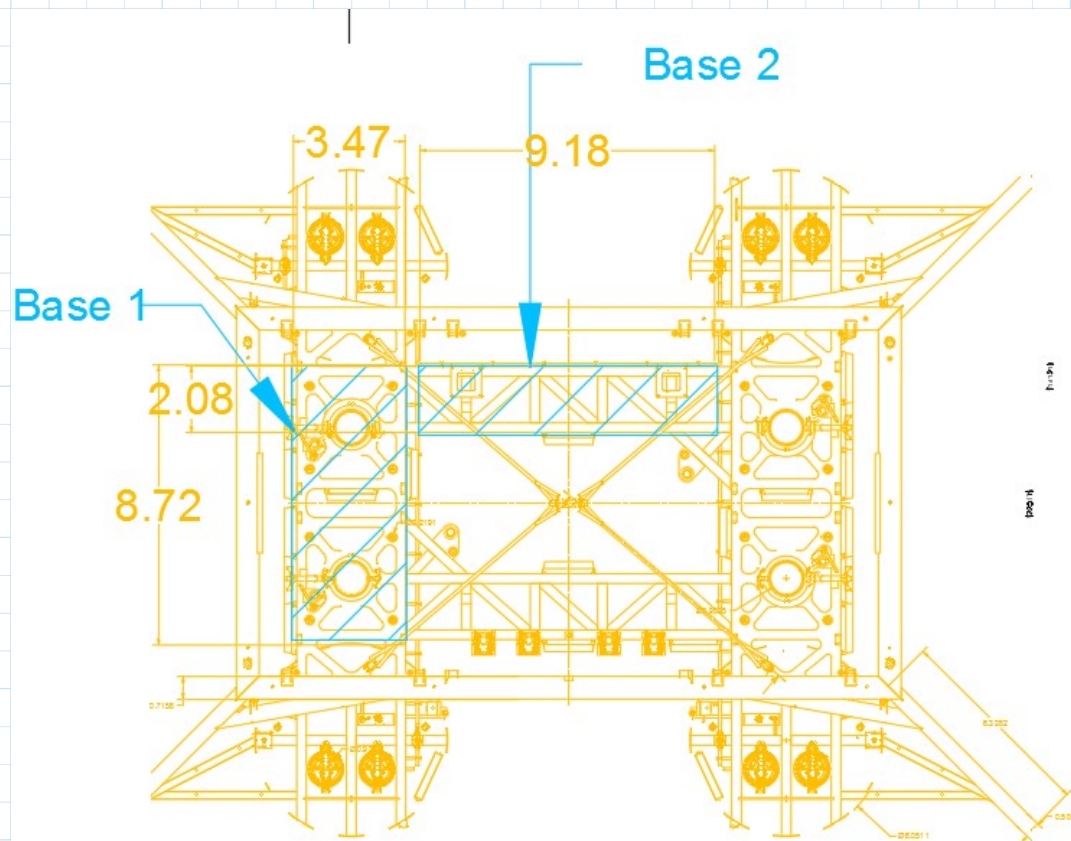
Base 1 - Vertical (z)

The added mass calculation is based on a rectangular flat plate from DNV-RP-H103: Table A-2

Length:

$$b := 8.7 \ m$$

Width:

$$a := 3.5 \ m$$

Height:

$$h := 1 \ m$$

Length - width ratio:

$$ba_z := \frac{b}{a} = 2.486$$

Area:

$$A := a \cdot b = 30.45 \ m^2$$

Open area:

$$A_o := 13.5 \ m^2$$

Reference volume:

$$V_R := \frac{\pi \cdot a^2 \cdot b}{4} = 83.704 \ m^3$$

Perforation rate:

$$p := \frac{A_o}{A} \cdot 100 = 44.3$$

Reduction factor due to perforation:

$$r := e^{\frac{10 - p}{28}} = 0.293$$

Projected Area:
$$A_{PV1} := A \cdot \left(1 - \frac{p}{100}\right) = 16.95 \ m^2$$

Added mass coefficient:
$$C_{az} := 0.757 + \frac{(0.801 - 0.757) \cdot (ba_z - 2.0)}{2.5 - 2} = 0.8$$

Lambda:
$$\lambda := \frac{\sqrt{A_{PV1}}}{h + \sqrt{A_{PV1}}} = 0.805$$

Added mass for solid plate:
$$A_{33o} := \rho_w \cdot V_R \cdot C_{az} = 68.615 \ tonne$$

Added mass for 3d non-perforated structure:
$$A_{33s} := \left(1 + \sqrt{\frac{1 - \lambda^2}{2 \cdot (1 + \lambda^2)}}\right) \cdot A_{33o} = 91.064 \ tonne$$

Added mass including perforation:
$$A_{33.V1} := A_{33s} \cdot r = 26.717 \ tonne$$

Base 1 - Horizontal (x)

The added mass calculation is based on a rectangular flat plate from RP-H103 Table A-2. The drag calculation is based on a rectangular flat plate from RP-H103 Table B-2.

Length:
$$b := 12 \ m$$

Width:
$$a := 1 \ m$$

Height:
$$h := 3.5 \ m$$

Length - width ratio:
$$ba_z := \frac{b}{a} = 12$$

Area:
$$A := a \cdot b = 12 \ m^2$$

Reference volume:
$$V_R := \frac{\pi \cdot a^2 \cdot b}{4} = 9.425 \ m^3$$

Projected area:
$$A_P := A = 12 \ m^2$$

Added mass coefficient:
$$C_{az} := 1$$

Lambda:
$$\lambda := \frac{\sqrt{A_P}}{h + \sqrt{A_P}} = 0.497$$

Added mass for solid plate:
$$A_{33o} := \rho_w \cdot V_R \cdot C_{az} = 9.66 \ tonne$$

Added mass for 3d non-perforated structure:
$$A_{33.H1} := \left(1 + \sqrt{\frac{1 - \lambda^2}{2 \cdot (1 + \lambda^2)}}\right) \cdot A_{33o} = 14.966 \ tonne$$

Drag coefficient
$$C_d := 1.5 \qquad\qquad \textit{DNV-RP-H103: Appendix B}$$

Base 2 - Vertical (z)

The added mass calculation is based on a rectangular flat plate from DNV-RP-H103 Table A-2

Length: $\qquad b := 9.2 \ m$

Width: $\qquad a := 2.1 \ m$

Height: $\qquad h := 1 \ m$

Length - width ratio: $\qquad ba_z := \dfrac{b}{a} = 4.381$

Area: $\qquad A := a \cdot b = 19.32 \ m^2$

Open area: $\qquad A_o := 9 \ m^2$

Reference volume: $\qquad V_R := \dfrac{\pi \cdot a^2 \cdot b}{4} = 31.865 \ m^3$

Perforation rate: $\qquad p := \dfrac{A_o}{A} \cdot 100 = 46.6$

Reduction factor due to perforation: $\qquad r := e^{\frac{10-p}{28}} = 0.271$

DNV-RP-H103 4.6.4.1

Projected area: $\qquad A_{PV2} := A \cdot \left(1 - \dfrac{p}{100}\right) = 10.32 \ m^2$

Added mass coefficient: $\qquad C_{az} := 0.757 + \dfrac{(0.801 - 0.757) \cdot (ba_z - 2.0)}{2.5 - 2} = 0.967$

Lambda: $\qquad \lambda := \dfrac{\sqrt{A_{PV2}}}{h + \sqrt{A_{PV2}}} = 0.763$

Added mass for solid plate: $\qquad A_{33o} := \rho_w \cdot V_R \cdot C_{az} = 31.568 \ tonne$

Added mass for 3d non-perforated structure: $\qquad A_{33s} := \left(1 + \sqrt{\dfrac{1 - \lambda^2}{2 \cdot (1 + \lambda^2)}}\right) \cdot A_{33o} = 43.05 \ tonne$

Added mass including perforation: $\qquad A_{33.V2} := A_{33s} \cdot r = 11.656 \ tonne$

Base 2 - Horizontal (y)

The added mass calculation is based on a rectangular flat plate from DNV-RP-H103: Table A-2

Length: $\qquad b := 12 \ m$

Width: $\qquad a := 1 \ m$

Height: $\qquad h := 2.1 \ m$

Length - width ratio: $\qquad ba_z := \dfrac{b}{a} = 12$

Area: $\qquad A := a \cdot b = 12 \ m^2$

Reference volume: $\qquad V_R := \dfrac{\pi \cdot a^2 \cdot b}{4} = 9.425 \ m^3$

Projected area: $\qquad A_P := A = 12 \ m^2$

Added mass coefficient: $\qquad C_{az} := 1$

Lambda: $\qquad \lambda := \dfrac{\sqrt{A_P}}{h + \sqrt{A_P}} = 0.623$

Added mass for solid plate: $\qquad A_{33o} := \rho_w \cdot V_R \cdot C_{az} = 9.66 \ tonne$

Added mass for 3d non-perforated structure: $\qquad A_{33.H2} := \left(1 + \sqrt{\dfrac{1 - \lambda^2}{2 \cdot \left(1 + \lambda^2\right)}}\right) \cdot A_{33o} = 14.198 \ tonne$

Drag coefficient $\qquad C_d := 1.5 \qquad\qquad$ *DNV-RP-H103: Appendix B*

Summary - bottom structure:

The bottom structure properties are evenly distributed on 12 Orcaflex 3d buoys.

Number buoys in Orcaflex: $\qquad n := 12$

Total mass: $\qquad m_{tot} := 144.61 \ tonne$

Mass per buoy: $\qquad m_{buoy} := \dfrac{m_{tot}}{n} = 12.051 \ tonne$

Volume per buoy: $\qquad V_{buoy} := \dfrac{m_{buoy}}{\rho_s} = 1.535 \ m^3$

Vertical drag area per buoy: $\qquad A_{drag.z} := \dfrac{2 \cdot A_{PV1} + 2 \cdot A_{PV2} + 4 \cdot A_{pA}}{n} = 13.97 \ m^2$

Horizontal drag area per buoy:

$$A_{drag.xy} := \frac{12 \; m \cdot 1 \; m}{n} = 1 \; m^2$$

Vertical added mass coefficient

$$C_{az} := \frac{2 \cdot A_{33.V1} + 2 \cdot A_{33.V2}}{\rho_w \cdot V_{buoy} \cdot n} = 4.064$$

Added mass x-direction:

$$C_{ax} := \frac{2 \cdot A_{33.H1}}{\rho_w \cdot V_{buoy} \cdot n} = 1.585$$

Added mass y-direction:

$$C_{ay} := \frac{2 \cdot A_{33.H2}}{\rho_w \cdot V_{buoy} \cdot n} = 1.504$$